SIGNAL PROCESSING TECHNIQUES FOR IMPROVING IMAGE RECONSTRUCTION OF PARALLEL MAGNETIC RESONANCE IMAGING AND DYNAMIC MAGNETIC RESONANCE IMAGING

by

Huajun She

A dissertation submitted to the faculty of
The University of Utah
in partial fulfillment of the requirements for the degree of

Doctor of Philosophy

Department of Electrical and Computer Engineering

The University of Utah

May 2015

The University of Utah Graduate School

STATEMENT OF DISSERTATION APPROVAL

The dissertation of **Huajun She**
has been approved by the following supervisory committee members:

Rong-Rong Chen, Chair	12/16/2014	Date Approved
Edward V.R. DiBella, Member	12/16/2014	Date Approved
Cynthia Furse, Member	12/16/2014	Date Approved
Behrouz Farhang-Boroujeny, Member	12/16/2014	Date Approved
Glen Morrell, Member	12/16/2014	Date Approved

and by **Gianluca Lazzi**, Chair of

the Department of **Electrical and Computer Engineering**

and by David B. Kieda, Dean of The Graduate School.

ABSTRACT

Magnetic Resonance Imaging (MRI) is one of the most important medical imaging technologies in use today. Unlike other imaging tools, such as X-ray imaging or computed tomography (CT), MRI is noninvasive and without ionizing radiation. A major limitation of MRI, however, is its relatively low imaging speed and low spatial-temporal resolution, as in the case of dynamic contrast enhanced magnetic resonance imaging (DCE-MRI). These hinder the clinical use of MRI. In this thesis, we aim to develop novel signal processing techniques to improve the imaging quality and reduce the imaging time of MRI.

This thesis consists of two parts, corresponding to our work on parallel MRI and dynamic MRI, respectively. In the first part, we address an important problem in parallel MRI that the coil sensitivities functions are not known exactly and the estimation error often leads to artifacts in the reconstructed image. First, we develop a new framework based on multichannel blind deconvolution (MBD) to jointly estimate the image and the sensitivity functions. For fully sampled MRI, the proposed approach yields more uniform image reconstructions than that of the sum-of-squares (SOS) and other existing methods. Second, we extend this framework to undersampled parallel MRI and develop a new algorithm, termed Sparse BLIP, for blind iterative parallel image reconstruction using compressed sensing (CS). Sparse BLIP reconstructs both the sensitivity functions and the image simultaneously from the undersampled data, while enforcing the sparseness constraint in the image and sensitivities. Superior image constructions can be obtained by

Sparse BLIP when compared to other state-of-the-art methods. In the second part of the thesis, we study highly accelerated DCE-MRI and provide a comparative study of the temporal constraint reconstruction (TCR) versus model-based reconstruction. We find that, at high reduction factors, the choice of baseline image greatly affects the convergence of TCR and the improved TCR algorithm with the proposed baseline initialization can achieve good performance without much loss of temporal or spatial resolution for a high reduction factor of 30. The model-based approach, on the other hand, performs inferior to TCR with even the best phase initialization.

CONTENTS

LIST OF FIGURES

LIST OF TABLES

ACKNOWLEDGEMENTS

First and foremost, I would like to express my sincerest gratitude to my advisor, Professor Rong-Rong Chen, for giving me the chance to work with her, and sharing with me her keen insights and deep knowledge in many research areas. Without her invaluable guidance and kind support, I would never have been able to finish this dissertation.

I am truly grateful to Professor Leslie Ying from the State University of New York at Buffalo for her constant guidance during my research. In particular, my visits to her research laboratory were most valuable and I learned so much from close interactions with her. I would like to thank Professor Edward DiBella for the many discussions that we had in his office and for his constructive advice in many aspects of my research. I would like to thank Professor Cynthia Furse, Professor Behrouz Farhang-Boroujeny, and Professor Glen Morrell for serving in my PhD thesis committee and providing valuable suggestions during my qualifying exam, thesis proposal, and final defense.

I am indebted to all the colleagues I have worked with at the University of Utah. Thanks to Hong Wan, Dong Liang, and many others who supported my research in one way or another. Thanks to the friends who made my life at Utah memorable, especially Dong Liu, Shuchang Liu, Ran Meng, Yang Zhao, Ronghui Peng, Xuehong Mao, Yuchou Chang, Haifeng Wang, Yihang Zhou, Shreyas Payal, Nick Nielson, and the friends I met in Utah.

Finally I would like to thank my mother, my uncle, my aunt, and my whole family for their love and support throughout my life.

CHAPTER 1

INTRODUCTION

Magnetic resonance imaging (MRI) is widely used in radiology due to its ability to detect cancer and accurately diagnose several other diseases noninvasively. Compared to other medical imaging tools, such as X-rays and computed tomography (CT), the advantage of MRI is that it uses nonionizing radiation and does not have the risk of radioactive harm to people (1). In addition, MRI provides more flexibility in image contrast by using various imaging sequences and scanning protocols. MRI is broadly used in many applications, such as imaging brain, blood vessels, abdomen, and bones, etc. MRI can also be used to measure brain oxygen saturation, blood flow velocities, diffusion of water molecules, and concentration of metabolites.

The most challenging problem of MRI is its relatively slow acquisition speed and low spatial-temporal resolution. Although imaging speeds have increased dramatically over the last four decades, many clinical and research applications, ranging from dynamic contrast enhanced imaging of breast tumors to cardiac imaging, require faster imaging methods. Unfortunately, current MRI scanners already operate at the limits of potential imaging speed because of the technical and physiological problems associated with rapidly switched magnetic field gradients.

Many methods have been developed to deal with this problem. Parallel MRI reconstruction is one type of method to accelerate acquisition speed by using several coil

to acquire undersampled data simultaneously (2-4). Another way to accelerate imaging speed is the new emerging compressed sensing technology, which exploits the sparse property of images (5-8). It states that if an image is sparse in some transform domain, it can be accurately reconstructed using a subset of the data under certain conditions. In this thesis, we investigate several key challenges in accelerating MRI reconstruction. The main contributions of this thesis are three methods for rapid imaging technologies which utilize signal processing techniques including blind signal estimation and compressed sensing.

First, we consider image reconstruction from fully sampled multichannel phased array MRI data without prior knowledge of the coil sensitivities. To overcome the nonuniformity of the conventional sum-of-squares reconstruction (9), we develop a new framework based on multichannel blind deconvolution (MBD) (10-12) to jointly estimate the image function and the sensitivity functions. We investigate the nonuniqueness of the MBD problem by exploiting the smoothness of both functions in the image domain through regularization. We successfully demonstrate that the reconstructions by the proposed algorithm are more uniform than those by the existing methods using simulation, phantom, and in vivo experiments.

Second, we investigate image reconstruction from undersampled multichannel parallel MRI data using compressed sensing. Image reconstruction for parallel MRI can be formulated as a multichannel sampling problem where solutions are sought analytically (13). However, the channel functions given by the coil sensitivities in parallel imaging are not known exactly and the estimation error usually leads to artifacts (14). In this study, we propose a new reconstruction algorithm, termed Sparse BLIP, for blind iterative parallel imaging reconstruction using compressed sensing. The proposed algorithm reconstructs

both the sensitivity functions and the image simultaneously from undersampled data. It enforces the sparseness constraint in the image as done in compressed sensing (CS), but is different from CS in that the sensing matrix is unknown and additional constraint is enforced on the sensitivities as well. Both phantom and in vivo imaging experiments are carried out with retrospective undersampling to evaluate the performance of the proposed method.

Third, we investigate the image series reconstruction of dynamic contrast enhanced MRI (DCE-MRI) for breast tumor imaging. We provide a comparative study of the temporal constraint reconstruction (TCR) (15) versus model-based reconstruction (16). We find that, at high reduction factors, the choice of the baseline image greatly affects the convergence of TCR. We design a jigsaw undersampling pattern and form a good baseline estimation. The improved TCR algorithm with the proposed baseline initialization achieves good performance for a high reduction factor of 30. Next, we study the model-based reconstruction method (16), and find that the model-based reconstruction method performs inferior to TCR with even the best phase initialization that we have tested.

1.1 Dissertation Structure

This dissertation is organized as follows.

Chapter 2 is a brief introduction to MRI, which provides the necessary basic background about MR imaging. It covers some basic MR physics, including spin, magnetization, signal generation, signal reception, spatial encoding, and image generation, and fundamentals in parallel MRI, compressed sensing, dynamic MRI, and DCE-MRI.

In Chapter 3, we consider image reconstruction from fully sampled multichannel phased array MRI data. First, we introduce the structure of the multichannel blind deconvolution

(MBD) problem. Then we introduce the subspace approach (17) and the proposed regularized MBD approach. The proposed method is compared to the traditional methods using simulated dataset, phantom, and in vivo brain dataset.

In Chapter 4, we develop a sensitivity-based parallel imaging reconstruction method to iteratively reconstruct both the coil sensitivities and MR image simultaneously based on their prior information. First we introduce the Sparse SENSE (7) method and JSENSE (14) method. Then we describe the proposed Sparse BLIP method and its implementation. At last we compare the proposed method with IRGN-TV (18), Sparse SENSE (7), JSENSE (14), and L1-SPIRiT (8) using phantom, in vivo brain, and in vivo cardiac dataset.

In Chapter 5, we study the dynamic contrast enhanced MRI (DCE-MRI) for highly accelerated breast tumor imaging. We first review the traditional TCR method (15) and then describe the improved TCR method with our proposed sampling and baseline initialization approach. Then we present the phase-enhanced model-based method (19,20). We present a comparative study of the improved TCR method with phase-enhanced model-based method, and find that while the improved TCR method achieves good image reconstruction without much loss of spatial and temporal resolution at a high reduction factor of 30, the model-based method performs inferior to TCR with even the best phase initialization.

In Chapter 6, we summarize the main contribution of this dissertation and discuss future research directions.

CHAPTER 2

BACKGROUND

Since the first successful nuclear magnetic resonance (NMR) experiments, MRI has improved dramatically in imaging quality and imaging speed. MRI is a tomographic imaging method that produces images of internal physical and chemical characteristics of an object from externally measured NMR signals. NMR signals are used to form the image by spatial encoding technology, which uniquely encodes spatial information into the activated MR signals detected outside the object. Unlike computed tomography (CT) and positron emission tomography (PET), MRI can provide images with high resolution without using ionizing radiation. Furthermore, MRI can provide more flexibility in image contrast by using different imaging sequences and scanning protocols. These advantages lead MRI to become one of the most preferred imaging modalities in clinical applications.

2.1 Principle of Magnetic Resonance Imaging

2.1.1 Spin and Magnetization

As depicted in quantum physics, nuclei that have odd atomic weights or odd atomic numbers have angular momentum J (called a spin), such as the nucleus of a hydrogen atom (21-23). As shown in Figure 2.1, the angular momentum J gives rise to a nuclear magnetic moment $\mu = \gamma J$, where γ is gyromagnetic ratio. The overall magnetization M of an object is defined as the sum of all the micro nuclear magnetic moment. Without the

external magnetic field, the nuclear magnetic moments are randomly aligned, so the macroscopic magnetization of an object is zero. To activate magnetism from an object, we need to expose the object to an external magnetic field B_0. When exposed to an external magnetic field, a large part of the magnetic moments aligns with the external magnetic field.

From the quantum theory, the magnetic moment vectors can assume one of a discrete set of orientations when exposed to a strong external magnetic field. For the hydrogen ^{1}H nuclei, the magnetic moment vector takes one of two possible orientations: pointing up (parallel) and pointing down (antiparallel) as shown in Figure 2.2.

Classical mechanics can be used to describe the motion of the magnetic moment μ in the presence of B_0, which is termed as precession, as shown in Figure 2.3. The precession frequency is also denoted as Larmor frequency: $\omega_0 = \gamma B_0$. The direction of the field B_0 and its perpendicular plane are often referred to as the longitudinal direction (z-axial) and the transverse plane (x-y plane).

Because most spins adopt the parallel rather than the antiparallel state, the macroscopic magnetization $M = \sum \mu$ is in the direction of the B_0 field. The transverse component of macroscopic magnetization is zero at equilibrium since the precessing magnetic moments have random phases.

2.1.2 Bloch Equation

The interaction of the magnetization M with an external magnetic field B can be conveniently described by the Bloch equation (1):

$$\frac{dM}{dt} = M \times \gamma B + \frac{M_0 - M_z}{T_1} + \frac{M_{xy}}{T_2} , \qquad [2.1]$$

where M_{xy}, M_z, and M_0 are the transverse, longitudinal, and equilibrium magnetization, T_1 and T_2 are relaxation constants and are specific to different tissues.

2.1.3 Resonance

The net magnetization M is the source of signals used to provide information about the object. However, the net magnetization is not an oscillating signal (like a DC voltage), which is not detectable. In order to detect a signal from the spins, another radio frequency (RF) excitation field B_1 must be applied. As shown in Figure 2.4, an external RF field B_1 is applied in the transverse plane and precesses at the Larmor frequency. The magnetization M will be "excited" or flipped away from the equilibrium state, which can be described by Bloch equation.

2.1.4 Relaxation

After the excitation, there are two components of the magnetization M, i.e., longitudinal magnetization M_z and transverse magnetization M_{xy}. As shown in Figure 2.5 (a), after B_1 is removed, the magnetization will gradually return to the original equilibrium position through the process termed as "relaxation", which can be described by the Bloch equation [2.1]. The relaxation parameters are key to image contrast because different tissues have different relaxation parameters.

2.1.5 Signal Generation

As presented in Figure 2.5 (a), magnetization that is excited to the transverse plane precesses at the Larmor frequency. According to Faraday's law, the precession will induce

a changing voltage in the receiver coil tuned to the Larmor frequency, as shown in Figure 2.5 (b). This voltage is the signal that is used for imaging. The received signal is the cumulative contribution from all the excited magnetization in the volume. With only the homogeneous B_0 field present, the system does not contain any spatial information. The received signal is a complex harmonic with a single frequency peak centered at the Larmor frequency.

2.1.6 Spatial Encoding and K-space

The signal generated with the coil is a sum of local signals from all parts of the object. For a spatially homogeneous object, this signal is enough for imaging. But for a heterogeneous object, it is necessary to differentiate local signals from different parts of the object. In order to image a slice of the body, a linear gradient field G_z along z direction is used. The magnetic field will vary as $B(z) = B_0 + G_z z$. This variation causes the precession frequency to vary linearly in z direction: $\omega(z) = \gamma(B_0 + G_z z)$. Therefore, when the band-limited RF field B_1 is applied, only the protons at a slice of the body will be excited with the corresponding resonant frequency (1). The bandwidth of the RF pulse determines the thickness of the excited slice.

Similarly, the gradient fields G_x and G_y are applied to localize the MR signal in the x-y plane. The magnetic field at a specific spatial location (x, y) and time point t is $B(t) = B_0 + G_x(t)x + G_y(t)y$, and the precession frequency at position (x, y) becomes $\omega = \gamma(B_0 + G_x(t)x + G_y(t)y)$. The phase of magnetization can be computed from the integral of precession frequency: $\varphi(x, y, t) = \int_0^t \gamma(B_0 + G_x(\tau)x + G_y(\tau)y)d\tau$.

So the magnetization at position (x, y) and time point t is:

$$M_{xy}(x, y, t) = m(x, y)\exp\left(-j\int_0^t \gamma\left(B_0 + G_x(\tau)x + G_y(\tau)y\right)d\tau\right), \quad [2.2]$$

where exp is the exponential function. The signal received from the entire object is:

$$S(t) = \iint_{x,y} m(x, y)\exp\left(-j\int_0^t \gamma\left(B_0 + G_x(\tau)x + G_y(\tau)y\right)d\tau\right)dxdy. \quad [2.3]$$

After demodulation, i.e., removal of the carrier signal $\exp\left(-j\int_0^t \gamma B_0 d\tau\right)$, the signal is:

$$S(t) = \int_x\int_y m(x, y)\exp\left(-j\int_0^t \gamma\left(G_x(\tau)x + G_y(\tau)y\right)d\tau\right)dxdy. \quad [2.4]$$

Let $k_x(t) = \frac{\gamma}{2\pi}\int_0^t G_x(\tau)d\tau$, and $k_y(t) = \frac{\gamma}{2\pi}\int_0^t G_y(\tau)d\tau$, the signal can be represented as:

$$D(k_x, \mathrm{k}_y) = \int_x\int_y m(x, y)\exp\left(-j2\pi k_x x - j2\pi k_y y\right)dxdy. \quad [2.5]$$

This equation indicates that there is a Fourier transform relation between the received MR signal $D(k_x, \mathrm{k}_y)$ and the magnetization distribution image $m(x, y)$. In MRI, $m(x, y)$ is the desired image, and $D(k_x, \mathrm{k}_y)$ are the experimental data measured in the Fourier space, which is called the k-space (1). The received signal is the Fourier transform of the object image sampled at the spatial frequency (k_x, k_y) in k-space. Such a gathering method is different from the traditional optical imaging where pixel samples are measured directly.

2.1.7 K-space and Image Reconstruction

The MR sampling data in k-space are usually complex values. Low-frequency signals locate near the center of k-space, while high-frequency signals locate near the periphery of

k-space. Image resolution is determined by the extent of the k-space that is covered. The focus of view (FOV) is determined by the sampling density.

Figure 2.6 shows an in vivo brain image and its corresponding k-space magnitude image. Traditionally, fully sampled k-space sampling pattern is designed to meet the Nyquist criterion and has a full FOV image after inverse Fourier transform. Violation of the Nyquist criterion causes the aliasing in the reconstruction image. The appearance of the artifact depends on the undersampling pattern. Coherent aliasing is produced by equispaced undersampling and incoherent aliasing is produced by random undersampling. Incoherent sampling is essential to compressed sensing reconstruction, which will be illustrated later in this chapter. The appearance of such artifacts is shown in Figure 2.6 (c). Equispaced undersampling acquisition with a reduction factor of R=2 results in a half reduced FOV (FOV/2) with fold over aliasing artifacts. Image resolution is determined by the sampled region of k-space: lower frequency of samples gives lower resolution, as shown in Figure 2.7 (d).

2.2 Parallel MRI

2.2.1 Parallel Imaging

Imaging speed is one of the most important considerations in clinical MRI. In practical acquisition, to cover the whole k-space line by line is time consuming and may take several minutes. Therefore, MRI is much more susceptible to patient motion which leads to motion artifact in the reconstructed image. Although imaging speeds have increased dramatically over the years, current MRI scanners already operate at the limits of potential imaging speed because of the technical and physiologic problems associated with rapidly switched magnetic field gradients.

Parallel MRI (pMRI) is a technique to increase the speed of MRI acquisition, which works by acquiring a reduced amount of k-space data with several phased array receiver coils (2-4). Parallel MRI differs from conventional MRI in two ways. First, an array of coils is used to collect k-space data simultaneously. Second, to improve imaging speeds, the k-space is undersampled with respect to Nyquist rate.

The imaging equation of parallel data acquisition using an array of L receiver coils with sensitivity $s_l(x,y)$ can be expressed as the followings (3):

$$D_l(k_x,\mathrm{k}_y) = \int_x \int_y m(x,y)\, s_l(x,y)\, e^{-j2\pi k_x x} e^{-j2\pi k_y y}\, dxdy, \qquad [2.6]$$

where $m(x,y)$ is the desired image and $D(k_x,\mathrm{k}_y)$ are the data measured at k-space location (k_x,k_y). The term parallel imaging comes from the fact that $D_l(k_x,\mathrm{k}_y)$ are acquired simultaneously, and sensitivity encoding refers to the spatial encoding effect of $s_l(x,y)$. The k-space data from each coil is the Fourier transform of the sensitivity weighted image $m(x,y)s_l(x,y)$.

Fully sampled 8-channel head coil data for axial brain images are shown in Figure 2.7. Data are acquired using eight independent receiver channels instead of using a large homogeneous volume receive coil. Each receiver coil is more sensitive to the specific volume of tissue nearest to the coil, which means that the coils provide an additional source of spatial information for image reconstruction. The sensitivity weighted images of the eight coils are shown in Figure 2.7 (a), and their corresponding sensitivities are shown in Figure 2.7 (b).

In the case of undersampling, direct Fourier transform leads to aliasing image and

reconstruction algorithms are used to combine the undersampled data from each of the coils into a unaliased reconstructed image with the full FOV. The reconstruction methods of parallel MRI can be categorized into two groups: image-based parallel imaging reconstruction and k-space-based parallel imaging reconstruction. Image-based methods reconstruct images from the aliasing image of each coil and merge the images using knowledge of individual coil sensitivities. The commonly used image-based reconstruction methods include SENSE (3) and PILS (24). K-space based methods reconstruct the missing k-space data. The commonly used image-based reconstruction methods include SMASH (2), GRAPPA (4), AUTO-SMASH (25), and VD-AUTO-SMASH (26), etc. Among the pMRI algorithms, SENSE is the representative algorithm of the image-based method and GRAPPA is the representative algorithm for the k-space-based method.

2.2.2 SENSE

SENSE (3) is the first reconstruction algorithm used for clinical applications. It is considered as an "unfolding" algorithm in image domain. To perform the SENSE reconstruction, the maps of the coil sensitivities must be known. SENSE generally uses a prescan to measure sensitivity maps. After the prescan, an undersampled acquisition results in a reduced FOV in every coil image.

An example of 8-coil data of axial brain images is shown in Figure 2.8. For simplicity, only two coils are shown. We used an equispaced undersampling pattern of acceleration factor R = 2; the aliased pixels come from two locations at a distance of exactly half of FOV apart. The pixels of each coil image are weighted by the sensitivity of the coil. Pixels close to the coil will have a higher weighting than pixels further away. By knowing the aliasing pattern and the spatial sensitivities, we can write a linear equation and solve it to

obtain the values of the two pixels. The linear equations are described below:

$$A_1(x,y) = S_1(x,y) f(x,y) + S_1(x+FOV/2,y) f(x+FOV/2,y), \quad [2.7]$$

$$A_2(x,y) = S_2(x,y) f(x,y) + S_2(x+FOV/2,y) f(x+FOV/2,y), \quad [2.8]$$

where $A_1(x,y)$ and $A_2(x,y)$ are the aliased image pixel of coil 1 and coil 2 at position (x,y), $f(x,y)$ and $f(x+FOV/2,y)$ are the unaliased image pixel of the desired object image, and S_1 and S_2 are the sensitivities of the two coils. In these two equations, $A_1(x,y)$ and $A_2(x,y)$ are known from the undersampled coil images, and S_1 and S_2 are known from the prescan. So only $f(x,y)$ and $f(x+FOV/2,y)$ are unknown. We can solve this equation for the two pixels easily. The reconstruction for all pixels can be written into a matrix form and solved with a least square algorithm or gradient search algorithm.

When there is no noise and the sensitivities estimation is accurate, the acceleration factor could reach the number of the coil. However, in reality the SNR is low in a MRI scan. In addition, the sensitivities estimation from the prescan is not accurate enough. So inaccuracy in sensitivity estimation will propagate to the reconstructed image (14). These practical issues will limit acceleration factor far below the theoretical maximum value in actual reconstruction methods. Both image-based reconstruction methods and k-space-based reconstruction methods in parallel MRI have this problem.

2.2.3 GRAPPA

GRAPPA (4) has been employed in clinical applications to avoid the estimation of coil sensitivities which is necessary for SENSE. In addition to the equispaced sampling, GRAPPA samples a few auto-calibration signal (ACS) lines at the center k-space for

calibration. The conventional GRAPPA method reconstructs the missing k-space data by a linear combination of the acquired data, where the linear combination coefficients are estimated using the ACS lines.

Figure 2.9 shows an example of 2-coil k-space data. Each coil has an 11 x 11 data matrix. The black dots are acquired data and gray dots are unacquired data. The center 3 columns are fully sampled ACS lines, and outer k-space are equisapced undersampling with a reduction factor R = 2. The key is to work out how to generate missing lines, and this is where the calibration data are needed.

In Figure 2.9, we need to determine what combination of columns 5 and 7 from all coils gives the best approximation to column 6 of coil 1. Similarly, we must determine what combination gives the best approximation to column 6 of coil 2. The combination equations are given by:

$$k_{16} = a_{15}k_{15} + a_{17}k_{17} + a_{25}k_{25} + a_{27}k_{27}\ , \qquad [2.9]$$

$$k_{26} = b_{15}k_{15} + b_{17}k_{17} + b_{25}k_{25} + b_{27}k_{27}, \qquad [2.10]$$

where a and b are the combination coefficients that need to be estimated. They can be computed using data fitting algorithms such as least square or gradient search, etc. After the combination coefficients are computed out, the missing columns can be interpolated using the neighbor columns with these coefficients. For example, the 2nd column can be generated with columns 1 and 3 with those coefficients.

$$k_{12} = a_{15}k_{11} + a_{17}k_{13} + a_{25}k_{21} + a_{27}k_{23}\ , \qquad [2.11]$$

$$k_{22} = b_{15}k_{11} + b_{17}k_{13} + b_{25}k_{21} + b_{27}k_{23}\ . \qquad [2.12]$$

Finally, full k-space data are reconstructed for each coil, which are then Fourier transformed and combined into a single image using the square root sum-of-squares (SOS).

More detailed descriptions about GRAPPA are given by (2) and (4). More information from adjacent data blocks can help GRAPPA to improve reconstruction quality (27-29).

GRAPPA is an approximate scheme to interpolate missing lines in k-space with a linear model. When the acceleration factor is high, GRAPPA reconstruction can suffer from aliasing artifacts and noise amplifications, while SENSE is theoretically an exact scheme which can give the best performance when sensitivities are known exactly. But GRAPPA need not explicitly compute the sensitivity maps as SENSE does. This is one benefit of GRAPPA compared to SENSE.

2.3 Compressed Sensing MRI

Conventional MRI using Fourier imaging is based on Shannon sampling theory. The large number of data that Shannon sampling theory requires and the slow data acquisition scheme greatly limits the MR imaging speed. Therefore, many researchers are seeking methods to reduce the amount of acquired data without degrading the image quality. Parallel MRI is one method which is based on the multichannel sampling theory (13,30), and is a generalization to Shannon sampling theory. As we discussed before, its maximum reduction factor of undersampling is limited by the number of channels, while the new emerging compressed sensing (CS) theory (5,31) allows exact recovery of a sparse signal from a set of samples which is far below the Shannon sampling theory requires.

The CS theory (5,31) requires that: (a) the desired image have a sparse representation in a known transform domain; (b) the aliasing due to undersampling should be incoherent or noise like in that transform domain; (c) a nonlinear reconstruction should be used to solve a constrained minimization problem which enforces the consistency with the acquired data and the sparsity of the image representation.

MRI is suitable for compressed sensing reconstruction due to the following reasons (6). Most of the MR images have the property of sparsity. Some MR images are sparse in the original image domain, such as MR angiography. Some MR images are sparse in some transform domain, such as wavelet transform or total variation transform. MRI scanners naturally acquire samples in k-space domain, which gives an easy way for incoherent aliasing by random undersampling in k-space. The MRI reconstruction problem can be formed into a constrained minimization problem to address the data consistency and the sparse prior information.

If we know the signal is sparse in some transform domain, then the CS method tries to find the solution that is sparsest in the transform domain and satisfies the data consistency requirement. This process can be written into a constrained optimization problem:

$$\text{minimize} \left\| \Psi m \right\|_0$$

$$s.t. \left\| Am - d \right\|_2 < \varepsilon , \qquad [2.13]$$

where m is the sparse signal in some transform domain, and Ψ is the sparsifying transform such as wavelet or finite difference. $\left\| \cdot \right\|_0$ is the l_0 norm, which counts the number of nonzero coefficients in the sparse signal. A is the linear operator, d is the observed data, and the threshold parameter ε is usually set below the noise level. In the context of MRI, A usually refers to the undersampled Fourier transform.

The constrained optimization problem can be reformulated with the Lagrange's multipliers as

$$\arg\min_m \left\| Am - d \right\|_2^2 + \lambda \left\| \Psi m \right\|_0 . \qquad [2.14]$$

This l_0 minimization problem is difficult to solve numerically. Fortunately, Candes et al.

have proved that l_1 minimization is equivalent to l_0 minimization if the sparse transform matrix satisfies the restricted isometric property (RIP) (32,33). It has been shown that random Gaussian and partial Fourier matrices satisfy the RIP with high probability. The optimization problem is thus turned into:

$$\arg\min_m \|Am - d\|_2^2 + \lambda \|\Psi m\|_1, \qquad [2.15]$$

where $\|\cdot\|_1$ is the l_1 norm. This optimization problem is convex and can be solved with the nonlinear conjugate gradient algorithm or other convex optimization methods.

2.4 Dynamic MRI

2.4.1 General Dynamic MRI Methods

Dynamic MRI captures an object in motion by acquiring a series of images at a high frame rate to show the structure and function of the object. The application of dynamic MRI includes cardiac, breast, perfusion imaging, etc. Dynamic MRI collects more information than static MRI, which is helpful in detection of certain types of diseases such as cardiovascular diseases and breast cancer. Conceptually, the straightforward approach is acquiring full data to reconstruct each time frame separately. However, obtaining dynamic MR images with high spatial and temporal resolution in a short period of time is challenging. Over the years, a number of methods have been proposed to increase the acquisition rate of dynamic MRI without compromising image quality significantly. In general, such methods can be divided into three categories: methods based on exploiting correlations in time, correlations in k-space, or correlations both in spatially and temporally.

The most popular methods using temporal correlations includes keyhole (34), sliding

window (35), and temporal constraint reconstruction (TCR) method (15). Keyhole starts with gathering a full k-space data as the reference data. During the dynamic data acquisition, the center of k-space is updated at each time frame and the outer edge of k-space remains the same as the reference data. The sliding window method uses several frames of the acquired undersampled k-space data in a time window. The full k-space data are recovered by combining the high-frequency part of those k-space data in the window and the most recent low-frequency k-space data. Then the time window moves forward and repeats the process again. TCR assumes that the images of adjacent time frames are similar and uses the prior information that the finite difference along the time domain is sparse. With this sparse property, compressed sensing technology is used to do the reconstruction.

The methods that exploit correlations in the spatial domain are actually applications of parallel MRI (2-4). They exploit the correlation of the data acquired from multiple coils. These methods accelerate acquisition by collecting undersampled data with multiple coils. The missing data are recovered using the measured k-space data from all coils. In these methods, the image at each time frame is reconstructed independently from the images at other time frames.

The third type of methods exploit both spatial and temporal correlations (36-38). These methods are motivated by the fact that the Fourier transform of the spatial-temporal signal, i.e., the spatial-temporal frequency (*x-f*) signal, is usually very sparse. This enables the use of compressed sensing technology, which utilizes the sparsity in the *x-f* space. Another type of method that exploits spatial and temporal correlations is the k-t PCA method (39). PCA is a commonly used method that reduces highly dimensional datasets to lower

dimensionality by exploiting correlations in the data. In k-t PCA, the ACS data are used as the training data to find the principal components. Since the spatial-temporal signal projected onto the principal components is sparse, the compressed sensing-based method can be used.

2.4.2 DCE-MRI

The dynamic MRI application considered in the thesis is the dynamic contrast enhanced magnetic resonance imaging (DCE-MRI) for breast tumor detection. DCE-MRI provides a promising method to detect and characterize lesions. A contrast agent is injected and the data are acquired in k-space for each time frame. The acquired image series are used to track changes over time in the region of interest. DCE breast tumor imaging uses those contrast uptake patterns to distinguish malignant and benign tumors.

In DCE-MRI, high spatial resolution is desirable to identify tumor location, and high temporal resolution can improve the accuracy of quantitative analysis of the uptake and washout curves (40). However, high spatial resolution typically comes at the expense of high temporal resolution, and vice versa. A number of techniques have been used to enable the acquisition of images with both high spatial and temporal resolutions.

Model-based reconstruction (MBR) methods (16,20) assume that contrast agent (CA) exchanges at constant rates between vascular space and extravascular-extracellular space (EES). It constrains the magnitude of the reconstructed time series to be consistent with a pharmacokinetic model (16,20). The model only has a few parameters and it may achieve a reduction factor of eight as reported in (20).

The methods for general dynamic MRI reconstruction can also be used, such as Keyhole (34), UNFOLD (41), RIGR (42), HYPR (43), k-t BLAST (44), k-t FOCUSS (38), k-t PCA

(36,39), and TCR (15), etc. TCR method is easy to implement and perform well at reduction factor around ten. Usually, the initialization images are using low-resolution images reconstructed from the fully sampled low-frequency samples or the aliasing measurements images. However, the convergence of traditional TCR is relatively slow at high reduction factors. We find PCA also suffers from performance loss when initial estimation is too bad when reduction factors are high. To improve the limitations of these previous methods, we propose a better initialization method together with the corresponding sampling pattern to improve the reconstruction for both TCR and PCA at higher reduction factors.

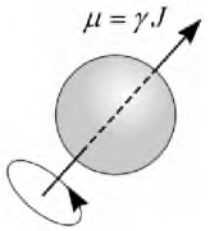

Figure 2.1 The nucleus angular momentum (spin) J gives rise to a nuclear magnetic moment $\mu = \gamma J$.

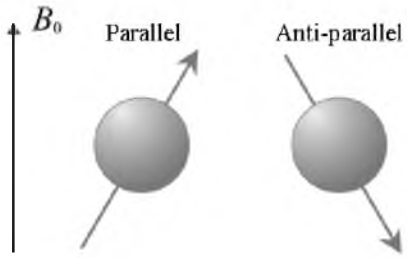

Figure 2.2 When exposed to an external magnetic field, the magnetic moment of the hydrogen nuclei can assume one of two orientations: parallel direction and antiparallel direction.

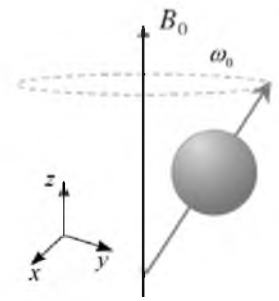

Figure 2.3 The magnetic moments precess in the presence of external magnetic field.

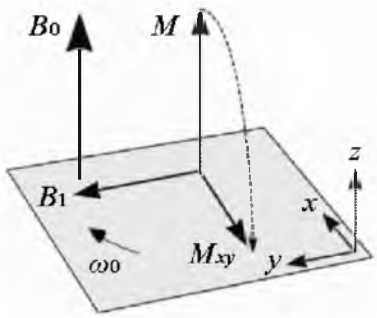

Figure 2.4 An external radio frequency excitation field B_1 is applied in the transverse plane and B_1 rotates at the same frequency as the spins precess. The magnetization M will be excited from the equilibrium state after B_1 is applied.

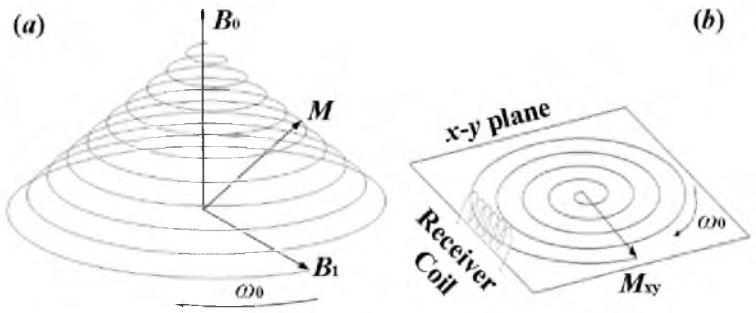

Figure 2.5 Describes how the receiver coil detects the signal from the magnetization. (a) After B_1 is removed, the magnetization will gradually return to the original equilibrium position through the relaxation process. (b) The transverse magnetization M_{xy} will induce a changing voltage in the receiver coil. This voltage is the signal that is used for imaging.

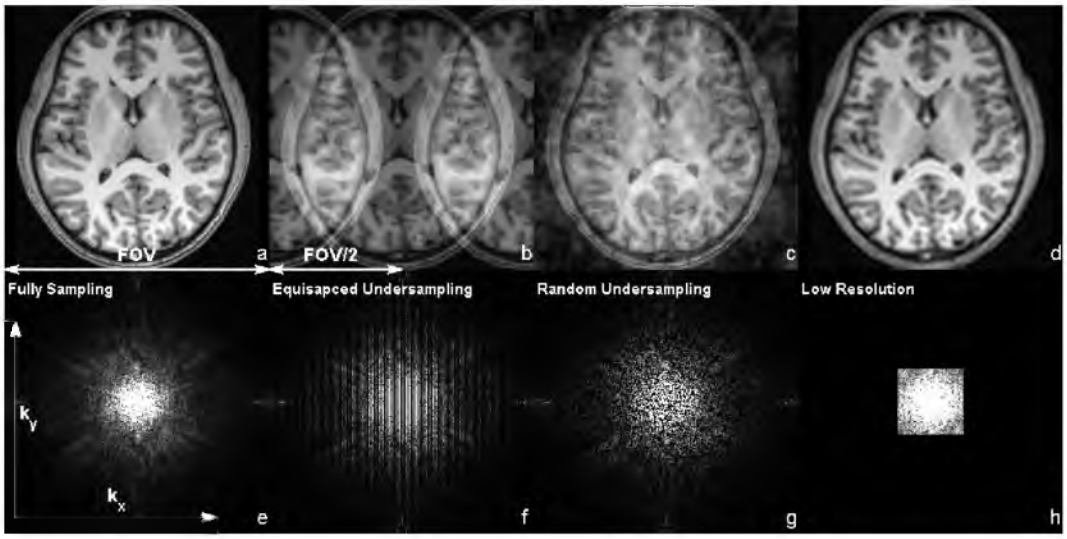

Figure 2.6 Describes different reconstruction images with different sampling patterns. (a) and (e) are the fully sampled brain image and its corresponding k-space magnitude image. (b) and (f) are the equispaced undersampling image and k-space image. The reduction factor of R=2 resulting in a half reduced FOV (FOV/2) with fold over aliasing artifacts. (c) and (g) show incoherent interference produced by random undersampling. Image resolution is determined by the sampled region of k-space, and lower frequency of samples gives lower resolution, as shown in (d) and (h).

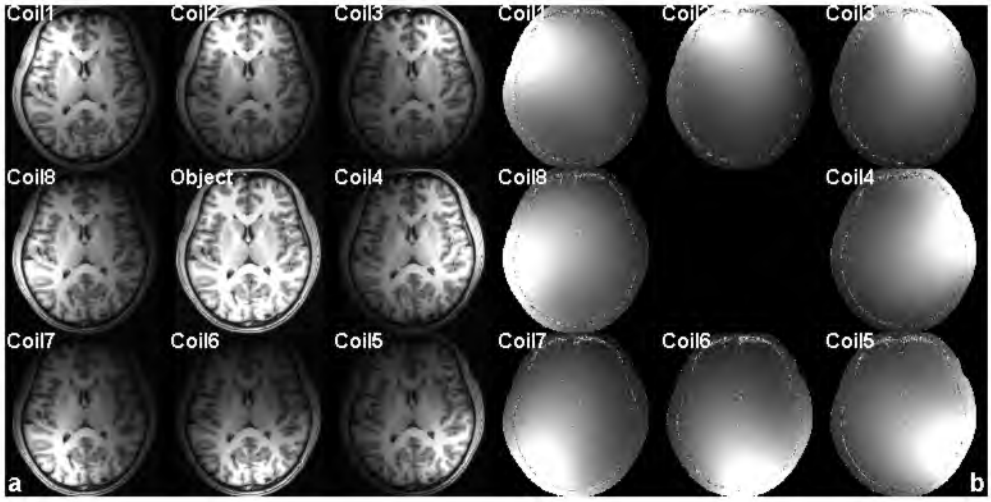

Figure 2.7 The sensitivity weighted images of the eight coils are shown in (a), and their corresponding sensitivities are shown in (b).

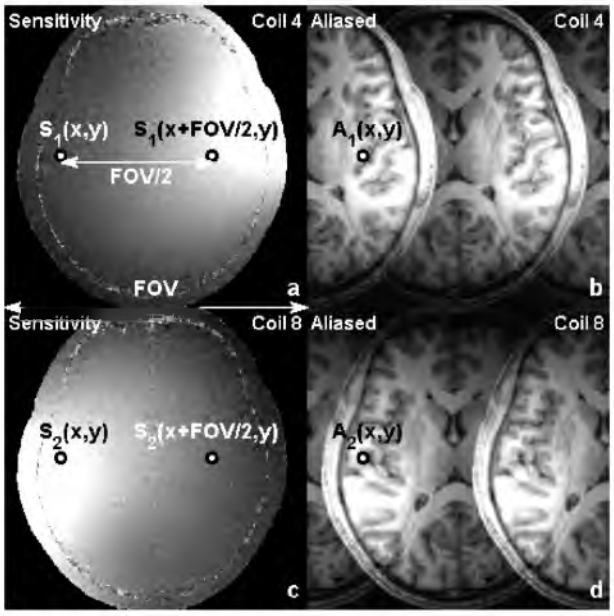

Figure 2.8 Describes the sensitivity encoding (SENSE) method. (a) and (c) are sensitivity maps of two coils. (b) and (d) are the aliased image from the two coils. An equispaced undersampling pattern of acceleration factor R = 2 is used. The sensitivity weighted aliased pixels in (b) and (d) come from two locations at a distance of exactly half of FOV apart.

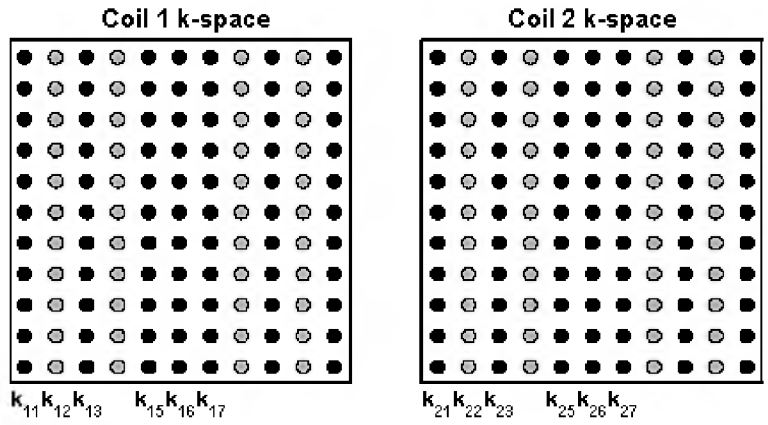

Figure 2.9 Two coils of undersampled k-space data are shown. The black dots are sampled data, and gray dots are the missing data. The fully sampled center calibration data consist of columns 5, 6, and 7.

CHAPTER 3

IMAGE RECONSTRUCTION FROM PHASED-ARRAY DATA BASED ON MULTICHANNEL BLIND DECONVOLUTION

MRI using phased array coils has emerged as a powerful technique to improve signal-to-noise ratio (SNR) of an image (9), reduce image acquisition time (2-4), or remove artifacts (45). With phased array coils, the acquired images usually have nonuniform intensity due to the coil sensitivity weighting. Removal of the sensitivity weighting for the original image requires prior knowledge of the sensitivities of the receiver coils (9,46,47). A typical method to reconstruct the original image without such prior information is the sum-of-squares (SOS) method (9). Other combination approaches (48-50) have also been proposed to improve SNR. For the SOS method, the reconstructed image is obtained by taking the square root of the sum of the absolute squares of the multiple images acquired with phased array coils. The SOS method effectively removes the spatially varying sensitivity weighting under the key assumption that the sum of the absolute squares of all sensitivity functions are spatially uniform. This assumption, however, is usually violated with surface coils, and the reconstructed image tends to be dark at locations further away from all coils (e.g., the center of the array). The nonuniformity of the image intensity greatly complicates further automatic analysis such as registration and tissue segmentation (51). Although nonuniform intensity of single-coil images has already been addressed by

numerous works (e.g., (51) and references therein), few works (17,52) have studied the issue in the context of multicoil images. In (52), an l_p norm was used in place of the l_2 norm in the SOS reconstruction to improve the uniformity, based on the assumption that the l_p norm of the sensitivity is uniform. The accuracy of such an assumption, however, depends on specific coil structures. Another method in (17) is based on a multichannel blind deconvolution (MBD) framework (10-12), treating both the original image and the sensitivity functions as unknowns to be reconstructed simultaneously. It adopts a subspace-based MBD method to perform deconvolution in the image domain and assumes a polynomial model for the sensitivity functions. A limitation of the method is that it is sensitive to noise, and typically high SNR acquisitions are needed for uniform reconstructions. Compared to (52), the MBD approach in (17) does not impose any uniformity constraint on the combined coil sensitivities.

In this paper, we propose a new approach to reconstruct the original uniform image using fully sampled multichannel data. Inspired by an approach developed previously for image super-resolution (53), the proposed method uses regularizations to address the non-uniqueness of the solutions, which utilizes the prior information that the image and sensitivity functions are smooth in the image domain.

3.1 Theory

3.1.1 Summary of the MBD Structure

In MRI with phased array coils, the k-space data are acquired simultaneously from L receiver coils with different sensitivities. The acquired data are the Fourier transform of the sensitivity-weighted images. The imaging equation is given by the Fourier imaging equation described in Chapter 2:

$$Y_i(k_x,k_y)=\iint f(x,y)h_i(x,y)e^{-j2\pi(k_x x+k_y y)}dxdy, \quad [3.1]$$

where (x,y) are image domain coordinates, $f(x,y)$ is the desired object image, $h_i(x,y)$ are the sensitivity functions for the *i*-th coil $(i=1,2,\cdots,L)$, (k_x,k_y) are k-space domain coordinates, and $Y_i(k_x,k_y)$ are the k-space sampling data collected from the *i*-th coil. The discretized sensitivity-weighted image can be represented by

$$y_i(m,n)=f(m,n)h_i(m,n). \quad [3.2]$$

When both the original image $f(m,n)$ and the sensitivity functions $h_i(m,n)$ are unknown, the problem of reconstructing the original image from the output $y_i(m,n)$ can be handled in the MBD framework.

3.1.2 Subspace Approach and Maximum-likelihood Approach

Two approaches are widely used for MBD image reconstruction. The first approach is the maximum-likelihood method (11), which utilizes the data consistency in measurements in Eq. [3.2]. The second approach for MBD is the subspace method (10,12), which utilizes the property, referred to as the cross-relation, that in the absence of noise, if the output of the *i*-th channel is put into the *j*-th channel, then the signal generated is the same as that generated by putting the output of the *j*-th channel into the *i*-th channel. Mathematically, we have

$$Y_i * H_j - Y_j * H_i = 0, \quad [3.3]$$

where H_i and H_j are the Fourier transform of h_i and h_j. Combining Eq. [3.3] for all (i,j) pairs, we obtain a set of equations which can be used to solve for the sensitivity functions

H_i given the acquired data. The subspace approach was adopted in (17) where the sensitivity functions are modeled as polynomials in the image domain. Since multiplication of polynomials becomes a linear convolution between the polynomial coefficients, the subspace-based MBD method was employed. However, the subspace approach is known to be sensitive to noise, which is also demonstrated in the Results section.

For our case of interest where circular convolution is involved, however, we observe that the solutions to both Eqs. [3.2] and [3.3] are not unique. To see this, we first show that the SOS reconstruction is always a solution to Eqs. [3.2] and [3.3]. Let us consider the SOS reconstruction

$$f_{sos}(m,n) = \sqrt{\sum_{i=1}^{L} |y_i(m,n)|^2}\,, \qquad [3.4]$$

and the corresponding sensitivity function given by

$$h_{sos,i}(m,n) = \frac{y_i(m,n)}{f_{sos}(m,n)}, \quad i = 1,\cdots,L\,. \qquad [3.5]$$

It follows that

$$y_i(m,n) = f_{sos}(m,n)\, h_{sos,i}(m,n)\,, \qquad [3.6]$$

and equivalently in k-space

$$Y_i(k_m,k_n) = F_{sos}(k_m,k_n) * H_{sos,i}(k_m,k_n)\,. \qquad [3.7]$$

This verifies that the SOS reconstruction is a solution to Eq. [3.2]. One can further verify that the following cross-relation holds:

$$Y_j(k_m,k_n) * H_{sos,i}(k_m,k_n) = Y_i(k_m,k_n) * H_{sos,j}(k_m,k_n)\,, \qquad [3.8]$$

which suggests that the SOS reconstruction is also a solution to the cross-relation Eq. [3.3]. It is easily seen that when we multiply a particular pixel of the SOS image $f_{sos}(m,n)$ by

γ, and multiply the corresponding pixel of sensitivity function $h_{sos,i}(m,n)$ by $1/\gamma$ to obtain a new pair of $f(m,n)$ and $h_i(m,n)$, the new pair is still a solution to Eqs. [3.2] and [3.3]. This confirms the nonuniqueness of both the maximum-likelihood and subspace methods for our case of interest, and the nonuniqueness leads to an ill-posed problem.

3.1.3 P-norm Approach

The p-norm approach is a generalization of the traditional SOS method. SOS is simple to implement and has nearly optimal SNR, but it may lead to signal inhomogeneity. The p-norm combination is given by

$$f_{pnorm}(m,n) = \left(\sum_{i=1}^{L} |y_i(m,n)|^p \right)^{1/p}. \qquad [3.9]$$

After the p-norm combination is computed, a constraint optimization problem is solved to estimate the optimal sensitivity *h*:

$$\arg\min_{h} \sum_{i} \left\| f_{pnorm} h_i - y_i \right\|^2 + \lambda R(h_i), \qquad [3.10]$$

where $h = \{h_1, h_2, \cdots, h_L\}$ are sensitivity functions, and $R(h_i)$ is the regularization term using total variation or finite difference. Then the estimated sensitivities are used to compute the weights:

$$w_i = \frac{h_i^*}{\sum_i |h_i|^2}, \qquad [3.11]$$

where $(\cdot)^*$ is the conjugate operator. These weights are used to compute the optimal linear combination (9) image

$$f_{opt} = \sum_i w_i y_i . \qquad [3.12]$$

The p-norm combination may increase image homogeneity in noise-free environments (52). However, the problem is generally ill-conditioned due to low SNR, and the SNR of f_{opt} is degraded when the p-norm combination is used for sensitivity estimation (52).

3.1.4 Regularized MBD Approach

Given the nonuniqueness of both approaches, we propose a new approach which employs regularization in the maximum-likelihood method to resolve the ambiguity in non-unique solutions. Two regularization terms are used with one for the image function and the other for the sensitivity functions, both incorporating smoothness constraint in the image domain. The proposed method can be equivalently regarded as a maximum a posteriori method with known prior (54). To estimate the image f and sensitivity functions $h = \{h_1, h_2 \cdots, h_L\}$, we minimize an objective function defined as

$$E(f,h) = \sum_{i=1}^{L} \left\| h_i \bullet f - y_i \right\|^2 + \alpha Q(f) + \beta R(h), \qquad [3.13]$$

where • denotes the pixel-wise product. The first term measures the fidelity to the data and comes from the acquisition model in Eq. [3.2]. The last two regularization terms utilize the smoothness of the image and the sensitivity functions in the image domain. The term $Q(f)$ is the l_2 norm of the finite difference of the image defined as

$$Q(f) = f^T \Lambda f \quad . \qquad [3.14]$$

Here, Λ is a positive semi-definite Laplacian matrix. Similarly, $R(h)$ is the summation of all coils' l_2 norm of the finite difference of the sensitivity functions, which is defined as

$$R(h) = \sum_{i=1}^{L} h_i^T \Lambda h_i \, . \qquad [3.15]$$

The parameters α and β are adjusted to control the convergence and smoothness of the solution to Eq. [3.13].

3.1.5 Alternative Minimization

It follows from Eq. [3.13] that the objective function can be written as

$$E(f,h)=\sum_{i=1}^{L}\left\|h_i \bullet f - y_i\right\|^2 + \alpha f^T \Lambda f + \beta \sum_{i=1}^{L} h_i^T \Lambda h_i \,. \qquad [3.16]$$

As a function of both f and h, the objective function E in Eq. [3.16] is not a convex function. However, E is convex with respect to f if h is fixed and is also convex with respect to h if f is fixed. Thus, the optimization problem can be solved by an alternative minimization (AM) method (14,53), which computes a minimization sequence $\left(f^m, h^m\right)$ alternatively. We propose the following two-step approach to find the values of f and h to minimize the objective function. Specifically we fix f or h and compute the derivatives with respect to h and f, respectively, and set them to be zero to find the minimum. After initialized with f^0 and h^0, the m-th iteration is performed as follows

$$\text{f-step: } f^m = \arg\min_f E\left(f, h^{m-1}\right) \Rightarrow \frac{\partial E}{\partial f} = 0 \Leftrightarrow \sum_{i=1}^{L} 2\left(h_i^{m-1}\right)^* \bullet \left(h_i^{m-1} \bullet f - y_i\right) + \alpha \Lambda f = 0 \,, \qquad [3.17]$$

$$\text{h-step: } h_i^m = \arg\min_{h_i} E\left(f^m, h_i\right) \Rightarrow \frac{\partial E}{\partial h_i} = 0 \Leftrightarrow 2\left(f^m\right)^* \bullet \left(h_i \bullet f^m - y_i\right) + \beta \Lambda h_i = 0 \,, \qquad [3.18]$$

where $(\cdot)^*$ is the conjugate operator.

3.2 Methods

The proposed MBD method was evaluated on four T1-weighted datasets: simulated data, phantom data, in vivo brain data, and in vivo cardiac data. All reconstruction methods were

implemented in MATLAB on a workstation. The SOS reconstruction, the subspace reconstruction, and the p-norm reconstruction are provided for comparison. All reconstructed images for the same dataset are normalized for visual evaluations.

3.2.1 Phantom Experiment

The objective of the phantom experiment is to demonstrate that the proposed method can generate uniform intensity in reconstructions. A phantom that is piecewise-constant was used for easy identification of nonuniformity. A T1-weighted scan was performed on the phantom using a two-dimensional spin echo sequence on a 3T commercial scanner (GE Healthcare, Waukesha, WI) with a four-channel torso coil (echo time/pulse repetition time = 11/300 ms, FOV = 18 × 18 cm, matrix = 256 × 256, slice thickness = 1.7mm). For comparison, SOS method, subspace method, and p-norm method were also used for reconstruction. The regularization parameters are: $\alpha = 1\times10^{-5}$, $\beta = 1\times10^{2}$ for the proposed method.

3.2.2 In vivo Human Brain Imaging Experiment

This experiment is to examine the performance of the proposed method when applied to in vivo data. One set of sagittal in vivo human brain data was acquired. The sagittal dataset was on a GE 3T scanner (GE Healthcare, Waukesha, WI) with a four-channel head coil and a 3-D T1-weighted spoiled gradient echo sequence (TE = minimum full, TR = 7.5ms, FOV = 24 × 24 cm, matrix = 256 × 256, slice thickness = 1.7mm). Informed consent was obtained from the volunteer in accordance with the Institutional Review Board policy. Similar to the phantom study, the SOS, subspace method, and p-norm method were used for performance comparison. The values for the regularization parameters are: $\alpha = 1\times10^{-5}$,

$\beta = 1\times10^4$ for the proposed method.

3.2.3 In vivo Cardiac Imaging Experiment

This experiment is to examine the performance of the proposed method when applied to one frame of in vivo cardiac data, where air-tissue boundaries induce sharp transitions in the estimated coil sensitivities. The dataset was acquired from a 3T scanner (Siemens Trio, Erlangen, Germany), with a 12 channel phased array coil (combined to 4 coils), using a 2-D true FISP sequence (TE = 1.87 ms, TR = 29.9 ms, BW = 930, flip = 50°, FOV = 34 × 28.6875 cm, matrix = 256 × 216, slice thickness = 6mm). The values for the regularization parameters are: $\alpha = 1\times10^{-4}$, $\beta = 1\times10^4$ for the proposed method.

3.2.4 Simulation

A 128 × 128 MR image is used as the original image. The simulated k-space data (noise-free) were generated by Fourier transforming the images weighted by a set of eight sensitivity functions. The sensitivity functions were simulated using the Biot-Savart law (17). The objective of this simulation is to study the effectiveness of the proposed method under noise-free measurements. The proposed method is compared with the SOS method, the subspace method, and the true image. The values for the regularization parameters are: $\alpha = 1\times10^{-5}$, $\beta = 1\times10^{-2}$ for the proposed method.

3.2.5 Parameters Selection

For the proposed method, different regularization parameters are needed for optimization. Regarding the choice of parameters, we find: (a) the parameters should be chosen such that the three terms in Eq. [3.16] are roughly in the same order. (b) Since the sensitivity function is in general smoother than the image, the parameter β should be

orders of magnitude larger than α to impose a stronger smoothness constraint.

3.3 Results

3.3.1 Phantom Experiment

For the phantom data, Figure 3.1 presents the reconstructed images using three different methods. We observe that the intensity of reconstruction using the proposed method is more uniform across the whole image, when compared with the SOS reconstruction, which is very dark in the center, and the subspace method, which is clearly nonuniform along the vertical direction, and p-norm method, which is also nonuniform around the center.

3.3.2 In vivo Human Brain Imaging Experiment

Reconstructions for the in vivo human brain sagittal data are shown in Figure 3.2. The intensity of the reconstruction by the proposed method is more uniform across the whole image, when compared with those by the SOS, subspace method, and p-norm method. In particular, the region toward the neck part makes the details more visible than that in the SOS reconstruction and subspace method. The subspace method is unable to provide a uniform reconstruction, possibly due to its lack of robustness to noise. The proposed method gives a less noisy reconstruction compared with the p-norm method toward the top-left region of the brain.

3.3.3 In vivo Cardiac Imaging Experiment

Reconstructions for the in vivo cardiac data are shown in Figure 3.3. The intensity of the reconstruction by the proposed method is more uniform across the whole image with a brighter vessels part, when compared with those by the SOS and subspace methods. In particular, the brighter region toward the heart and vessels makes the details more visible

than that in the SOS and subspace method. The proposed method gives a less noisy reconstruction compared with the p-norm method, especially at the vessels part and the top-right region of the image.

3.4 Discussion

3.4.1 Effectiveness Test Using Simulated Data

To study the effectiveness of the proposed method under noise-free measurements, we have compared the SOS, proposed method, and subspace method using the simulated data. Figure 3.4 presents the true image and the reconstructed images obtained from the SOS, proposed method, and subspace method. Figure 3.5 shows the root sum-of-squares of the corresponding sensitivity functions. It is observed in Figure 3.4 that the center part of the SOS reconstruction image is darker compared to that of the proposed method and the subspace method. This is because the SOS reconstruction is based on the assumption that the sum-of-squares of the sensitivity functions is a constant. However, as shown in Figure 3.5, this assumption is clearly violated for the sensitivity functions. In comparison, the root sum-of-squares for the estimated sensitivity functions obtained by the proposed method and the subspace method is nonuniform and resembles that of the true one. In this experiment, the proposed method is seen to perform better than the subspace method in reconstructing the original image and sensitivities.

3.4.2 Relation to Previous Works

We proposed a multichannel blind deconvolution reconstruction method in k-space for phased-array MRI data in (55), where the image function and sensitivity functions are all expressed and solved in k-space domain. The computation and store of the convolution

matrices in k-space take a lot of running time and memory, which leads to slow reconstruction speed. By handling the estimation problem in the image domain, we accelerate the running time and occupy less memory in this work. Previously in (55), we included a cross-relation term as a regularization term in the objective function to address the cross-relationship in the theory section. However, we found that the solutions of cross-relation are nonunique. Besides, the subspace method is sensitive to noise and may lead to the wrong solution. So in this paper we have not included the cross-relation term in the objective function. Based on these improvements, we notably improve the computation speed or reconstruction quality. For instance, in our reconstruction of the in vivo sagittal brain dataset, the computer running time of the proposed image domain method is around 120 seconds, while the k-space method needs more than 600 seconds. The reconstruction results of the image domain method and the k-space method are shown in Figure 3.6. We can see that, for this phantom dataset, the image domain method significantly improves the homogeneity of the reconstruction image comparing with the k-space method.

It is also worth noting that the first iteration of the proposed method is similar to the p-norm method. However, the p-norm method has not utilized the better estimated image and sensitivity to improve each other's reconstruction, while the proposed method improves the image and sensitivity through AM iterations. Such an AM optimization method can be proved to converge to a local minimum (56).

3.4.3 Initialization

The proposed method is robust to different initialization. We have tried totally random initialization with noise like image and sensitivities as well as initialization with p-norm combination. Figure 3.7 shows the comparison results of random initialization and p-norm

initialization. We can see that both initialization methods lead to similar reconstruction images.

3.4.4 Convergence and Computation Complexity

The prosed method converges fast and only needs 6 ~ 8 AM iterations. In the reconstruction of the sagittal brain dataset, the computer running time is around 120 seconds. The objective function decreases fast over the first few iterations. After that, the algorithm converges and further iterations do not improve the quality of the reconstruction.

This is demonstrated in Figure 3.8 for the in vivo brain data, where the 1st iteration reconstruction appears inhomogeneous and noisy, the 4th iteration reconstruction appears uniform, and the 6th iteration and 10th iteration show little difference from the 4th iteration. Figure 3.9 shows the objective function $E(f,h)$ versus the number of iterations for the optimization. $E(f,h)$ decreases until convergence after 6 iterations.

3.4.5 Signal-to-noise Ratio

In addition to the uniformity of intensity, the SNR of the final reconstruction is also improved over the SOS reconstruction and p-norm reconstruction due to the regularization terms for both image and sensitivities in the proposed method. We can observe the improvement of SNR for the proposed method over SOS reconstruction and p-norm reconstruction in Figure 3.2 and Figure 3.3, as discussed in the results section.

3.5 Conclusion

In this paper, we develop a regularized MBD method for image reconstruction using multichannel phased-array MRI data. The proposed method is compared with SOS, subspace method, and p-norm method using computer simulation, phantom, and in vivo

experiments. The results demonstrate that the proposed method reconstructs more uniform images than the SOS does. It is also more robust than the subspace approach in the presence of measurement noise. The proposed method gives more uniform or high SNR reconstructions than p-norm method.

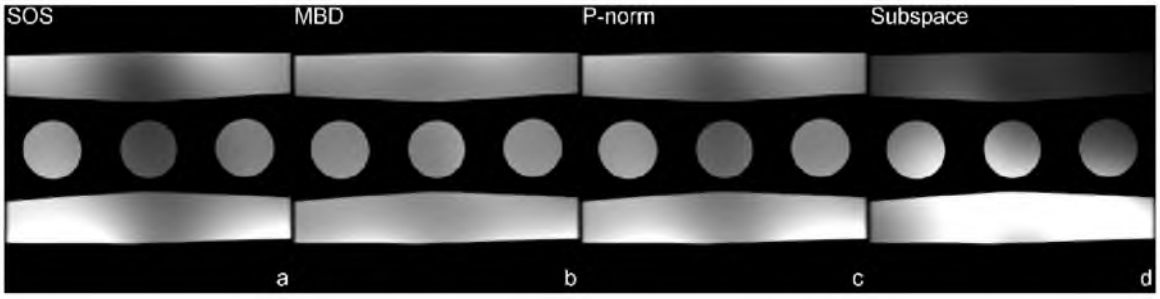

Figure 3.1 Experimental results from a set of phantom data for the SOS (a), the proposed method (b), p-norm method (c), and subspace method (d). We can see the image intensity of the proposed method is more uniform than that of the SOS, p-norm method, and subspace method.

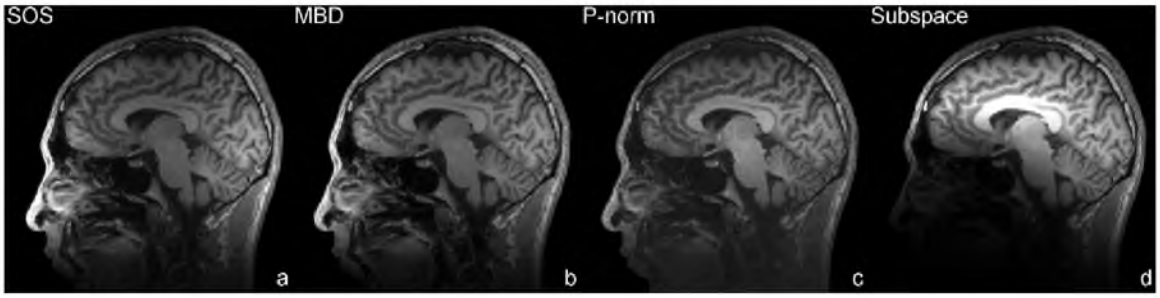

Figure 3.2 Experimental results from a set of in vivo sagittal brain data for the SOS (a), the proposed method (b), p-norm method (c), and subspace method (d). The higher level of uniformity in the proposed method makes some image details more visible in the region toward the neck compared with SOS and subspace method. The top-left part of the reconstruction image of p-norm method is noisier compared with the proposed method.

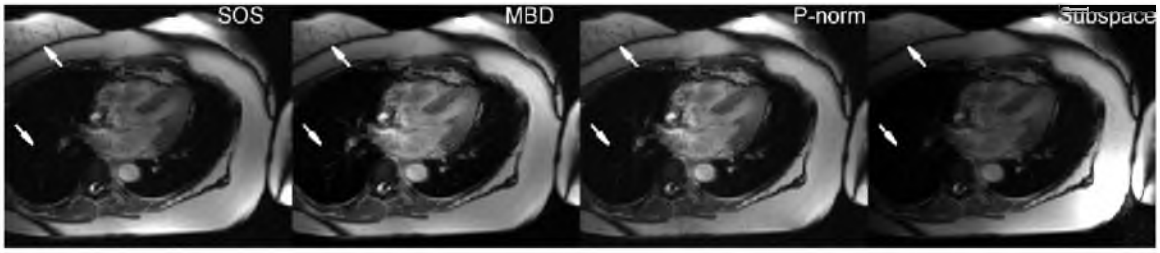

Figure 3.3 Experimental results from a set of in vivo cardiac data for the SOS (a), the proposed method (b), p-norm method (c), and subspace method (d). The higher level of uniformity in the proposed method makes some image details more visible in the region toward the vessels compared with subspace method. The vessels part of the reconstruction image of p-norm method is noisier compared with the proposed method.

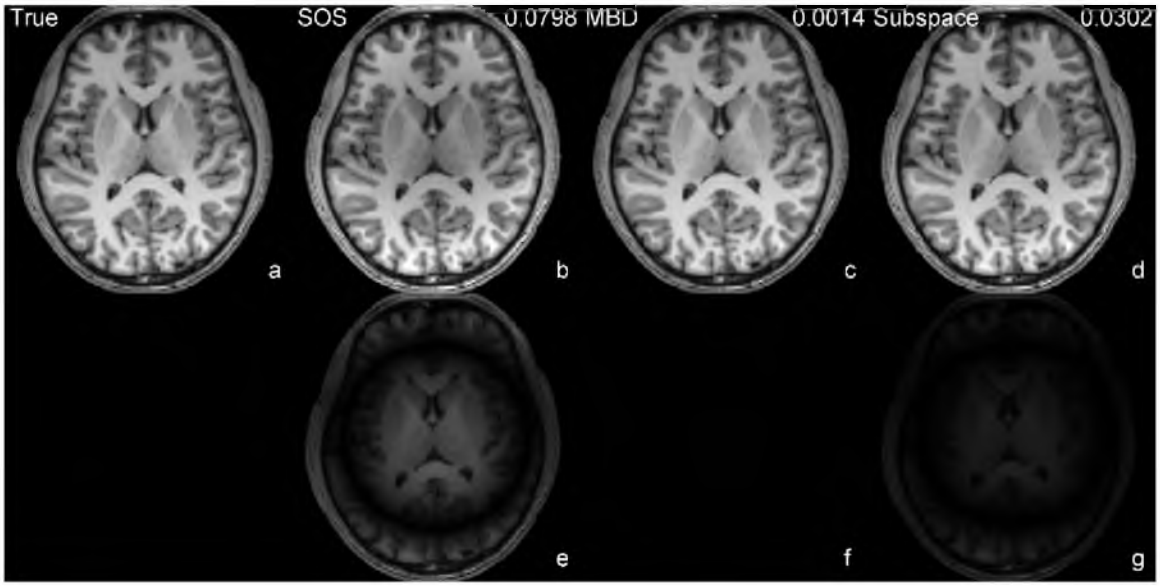

Figure 3.4 Simulation results for a 128 × 128 image reconstructed from a set of 8-channel data of the original image (a), SOS (b), the proposed method (c), and the subspace method (d) are shown in the first row. The difference image of SOS (e), the proposed method (f), and the subspace method (g) compared with the original image are shown in the second row. With the original image for reference, the reconstructions using the proposed method, subspace method, and p-norm method are brighter than the SOS reconstruction in the central region.

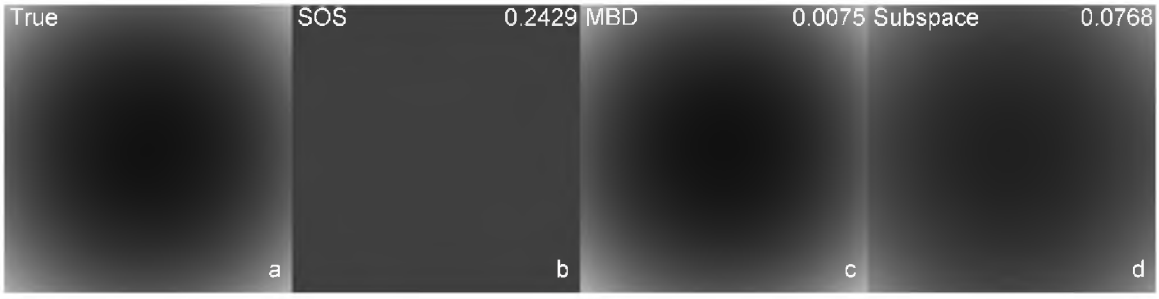

Figure 3.5 Composite images for the root sum-of-squares of the original (a) and estimated sensitivity functions for SOS (b), the proposed method (c), and the subspace method (d). The proposed method and subspace method show similar composition to the original one, while the composite sensitivity image from the SOS method is far away from the true one. Furthermore, the composition of the proposed method gives the smallest nRMSE compared with the true one.

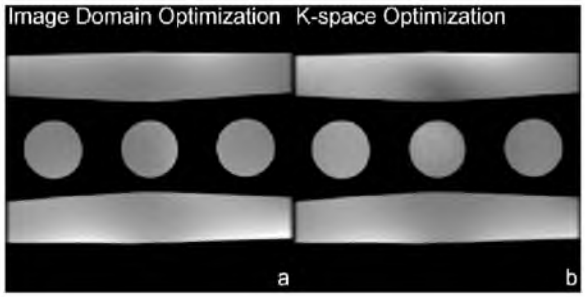

Figure 3.6 Comparison reconstruction results of image domain method (a) and k-space method (b). Image domain method gives more uniform reconstruction than k-space method.

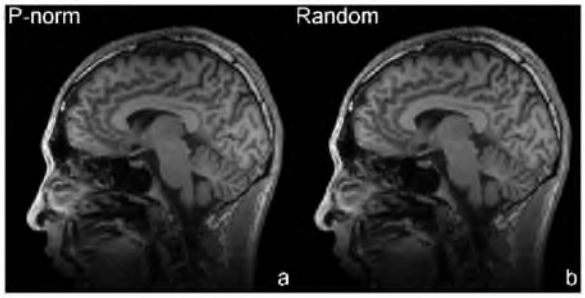

Figure 3.7 Comparison reconstruction results of random initialization (a) and p-norm initialization (b). Both initialization methods lead to similar reconstruction images.

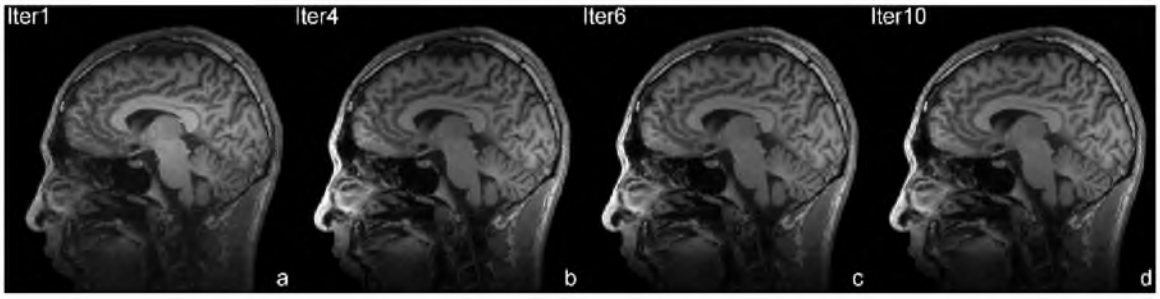

Figure 3.8 Reconstruction images of the proposed method for the 1st (a), 4th (b), 6th (c), and 10th (d) rounds of optimization for the in vivo brain dataset. We can see after the 1st round optimization, the reconstruction is close to the p-norm results, and after 4 iterations, the reconstruction image homogeneity is increased. Further iterations do not improve much of the reconstruction quality.

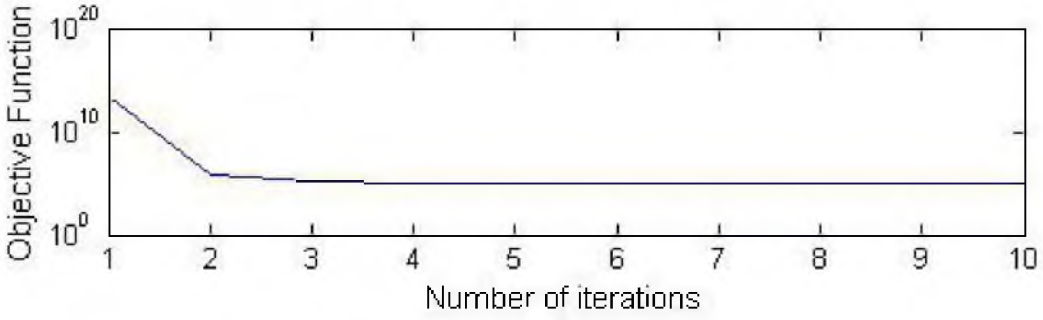

Figure 3.9 Convergence curves of the objective function value of the proposed method for the 1st, 4th, 6th, and 10th rounds of optimization for the in vivo data.

CHAPTER 4

SPARSE BLIP: BLIND ITERATIVE PARALLEL IMAGING RECONSTRUCTION USING COMPRESSED SENSING

Parallel imaging with phased array coils can be formulated as a multichannel sampling problem (13,30). Based on Papoulis generalized sampling theorem (57), SENSE (3) is an optimal reconstruction method among many existing methods (e.g., SMASH (2), AUTO-SMASH (25), PILS (24), SPACE-RIP (58), GRAPPA (4)) when exact knowledge of the coil sensitivities is provided. However, coil sensitivities are usually obtained from low-resolution images or through a separate scan, where accuracy cannot be guaranteed. Inaccuracy in estimation of coil sensitivities may lead to artifacts at high acceleration factors. JSENSE (14) provided a framework for image reconstruction without knowledge of coil sensitivities. It models both coil sensitivities and the desired image as unknowns to be reconstructed simultaneously. The underlying nonlinear problem can be solved by alternating minimization (14) or Gauss Newton method (59).

With the recent emergence of compressed sensing (CS) theory (5,31) and its successful application in MRI (6), several techniques (7,60-66) have been developed to apply CS to SENSE. Among these techniques, Sparse SENSE (7) is a direct application of CS reconstruction to SENSE with pseudo random trajectories. It minimizes the L_1 norm of the image in the sparsifying transform domain under the data consistency constraint from SENSE reconstruction equation. Similar to SENSE, these methods all suffer from artifacts

when coil sensitivities are inaccurate. Recently, there are a number of methods that explicitly take advantage of the smoothness prior in coil sensitivities (18,67,68). For example, (68) explores the sparseness of coil sensitivities using polynomial or Fourier transforms without regularization for the image, while (18), i.e., the iteratively regularized Gauss-Newton method with total variation (IRGN-TV), employs TV regularization for the image and a weighted L_2 norm in the frequency domain to incorporate the smoothness prior of sensitivities, and (67) also employs TV regularization for the image but a L_2 norm of high-order derivative for the sensitivities. On the other hand, L_1-SPIRiT (8) integrates CS with the k-space-based parallel imaging method and has the advantage of reconstruction without explicit representation of coil sensitivities in the image domain.

The sparseness model of CS provides a general prior for most images. Given the smoothness of coil sensitivities, the sparseness prior should also be able to represent the coil sensitivities with high fidelity and thus improve JSENSE. In this chapter, we propose a new approach of blind iterative parallel imaging reconstruction using compressed sensing, termed Sparse BLIP. Built on the formulation of JSENSE, the proposed Sparse BLIP method effectively incorporates the sparseness constraint to both the desired image and coil sensitivities. Subject to the data consistency constraint of the SENSE equation, the image and coil sensitivities are regarded both as unknowns and the total variation (TV) of both image and sensitivities are minimized simultaneously. We use an alternating minimization (AM) method (14) to find a suboptimal solution to the original nonconvex minimization problem. The convergence of the AM method to a local minimum is studied in (56). Starting with an initial estimation of coil sensitivities, the method alternately updates the reconstructed images and the coil sensitivity functions in each iteration, and

repeats until convergence. The performance of the proposed method is compared with that of Sparse SENSE, IRGN-TV, JSENSE, and L_1-SPIRiT.

4.1 Theory

4.1.1 Summary of Sparse SENSE

In SENSE with arbitrary trajectories, the imaging equation can be written as

$$\mathbf{Ef} = \mathbf{d}, \qquad [4.1]$$

where **d** is the vector formed from all k-space data acquired from all channels, and **f** is the unknown image vector formed from the desired full field of view (FOV) image. The encoding matrix **E** consists of the product of Fourier encoding and modulation by the coil sensitivity over the image, i.e.,

$$\mathbf{E}_{\{l,m\},n} = e^{-i2\pi \mathbf{k}_m \cdot \mathbf{r}_n} s_l(\mathbf{r}_n), \qquad [4.2]$$

where $\mathbf{k}_m$ and $\mathbf{r}_n$ denote the coordinates of the k-space data and image domain pixels respectively, and s_l denotes the sensitivity of the l-th coil. To reconstruct the desired image **f** given knowledge of acquired data **d** and sensitivities s_l, the least-squares method is usually used to solve Eq. [4.1]. Sparse SENSE (7) directly applies CS to SENSE by generalizing the formulation of Sparse MRI (6) to sensitivity encoding. In data acquisition, the k-space data are undersampled with fully sampling at the center and undersampled less near the k-space center and more in the periphery. In reconstruction, the problem is formulated as a constrained nonlinear convex program based on the SENSE equation [4.1]:

$$\text{minimize } \|\mathbf{\Psi f}\|_1 \text{ s.t. } \|\mathbf{Ef} - \mathbf{d}\|_2 \le \varepsilon, \qquad [4.3]$$

where $\mathbf{\Psi}$ is the sparse transformation matrix. We write Eq. [4.3] into a regularization form and add a TV of the image penalty term as

$$\arg\min_{\mathbf{f}} \left\{ \left\| \mathbf{d} - \mathbf{E}\mathbf{f} \right\|_2^2 + \lambda \left\| \Psi \mathbf{f} \right\|_1 + \alpha \mathrm{TV}(\mathbf{f}) \right\}, \quad [4.4]$$

where λ and α are regularization parameters which control the tradeoff between data consistency and sparseness prior, and the anisotropic TV operator on a complex image **f** is defined as:

$$\mathrm{TV}(\mathbf{f}) = \sum_{u=1}^{U} \sum_{v=1}^{V} \left| f_{u+1,v} - f_{u,v} \right| + \left| f_{u,v+1} - f_{u,v} \right|, \quad [4.5]$$

where u and v are pixel indices for the image with size U by V. Sparse SENSE uses the fully sampled central k-space lines to estimate the sensitivities, and based on which the image is reconstructed. Hence, the inaccuracy in sensitivities estimation can propagate to the reconstructed image.

4.1.2 Summary of JSENSE

JSENSE (10) is a method to reconstruct the image and coil sensitivities simultaneously such that the initial estimated coil sensitivities can be corrected through iterations and error propagation can be alleviated in the final reconstruction. In reconstruction, instead of assuming that the sensitivity functions are known and given, JSENSE assumes that sensitivities are unknown. With a parametric model for the coil sensitivities with unknown parameters **a**, the imaging equation in Eq. [4.1] becomes

$$\mathbf{E}(\mathbf{a})\mathbf{f} = \mathbf{d}. \quad [4.6]$$

Then the unknown parameters **a** for coil sensitivities and the desired image **f** can be solved by finding a solution to the following minimization problem:

$$\arg\min_{\{\mathbf{a},\mathbf{f}\}} \frac{1}{2} \left\| \mathbf{d} - \mathbf{E}(\mathbf{a})\mathbf{f} \right\|^2. \quad [4.7]$$

The nonlinear optimization problem in Eq. [4.7] does not guarantee convergence to a global

optimal solution. When the pixel-based model is used for the coil sensitivities, the problem becomes highly under-determined and regularization on the sensitivity functions is usually needed to ensure convergence to a solution close to the true one (59). In (59), a weighted L_2 norm form of regularization term $R(c) = \|Wc\|^2$ was used to penalize the high Fourier coefficients of the sensitivities, where c is the coil sensitivities and W is some weighting matrix. While JSENSE incorporates some prior information (e.g., smoothness) in coil sensitivities, no prior information on image is employed. In addition, the original work was based on uniform trajectories, although it can be extended to arbitrary trajectories.

4.1.3 Proposed Method: Sparse BLIP

Similar to JSENSE, the proposed method aims to reconstruct the desired image and coil sensitivities simultaneously. The data consistency term is thereby given by Eq. [4.6] where a pixel-based model is used for the coil sensitivities and the unknown parameter **a** represents all pixels of the sensitivities of all coils. The acquired data $\mathbf{d}_l$ from the l-th channel relates to the unknown image and pixel-based coil sensitivity function $\mathbf{s}_l$ of the l-th channel by

$$F_D(\mathbf{s}_l \bullet \mathbf{f}) = \mathbf{d}_l, \qquad [4.8]$$

where $\bullet$ denotes the pixel-wise product and F_D is the undersampled Fourier operator. The proposed method improves upon JSENSE by incorporating the concept of CS into the data consistency formulation. Specifically, the data are acquired with incoherent sampling and the reconstruction enforces sparseness constraints on both the image and sensitivity functions. Incoherent sampling is the fundamental requirement for a successful reconstruction using the CS theory. Incoherent sampling means that the aliasing artifacts caused by k-space undersampling should be incoherent (i.e., noise-like) in the sparsifying

transform domain (5,6,31). Based on the CS theory, to resolve the ambiguity of nonunique solutions to Eq. [4.8], the sparsest solution in a predetermined transform domain is needed. In this work, both the image and sensitivities are assumed to be sparse in TV of the spatial domain. The image is also assumed to be sparse in the wavelet domain similar to Sparse MRI (6). Incorporating the sparseness constraint using the CS framework, the image $\mathbf{f}$ and sensitivity functions $\mathbf{s}_l$ are jointly reconstructed by minimizing the energy function defined as

$$E(\mathbf{f}, \mathbf{s}_l) = \sum_{l=1}^{L} \left\| \mathrm{F}_D \left(\mathbf{s}_l \bullet \mathbf{f} \right) - \mathbf{d}_l \right\|^2 + \lambda \left\| \Psi \mathbf{f} \right\|_1 + \alpha \mathrm{TV}\left(\mathbf{f} \right) + \beta \sum_{l=1}^{L} \mathrm{TV}\left(\mathbf{s}_l \right). \qquad [4.9]$$

In [4.9], L is the total number of coils. The first data consistency term measures the fidelity to the measurement from multiple coils. The second regularization term exploits the sparseness of the image in the wavelet domain. The last two regularization terms utilize the sparseness of the image and sensitivity functions in the TV of the image domain, where TV is defined in Eq. [4.5]. The positive constants λ, α, and β are adjusted to balance the tradeoff between data consistency and sparseness prior.

As a function of both unknowns $\mathbf{f}$ and $\mathbf{s}_l$, the objective function E in Eq. [4.9] is non-convex and thus convergence to the global optimal solution is not guaranteed. However, E is convex with respect to $\mathbf{f}$ if $\mathbf{s}_l$ is fixed and is also convex with respect to $\mathbf{s}_l$ if $\mathbf{f}$ is fixed. To tackle the nonconvex optimization problem, we use an alternating minimization (AM) method (53,56) to find a suboptimal solution. Specifically, the coil sensitivities are initially estimated using the densely sampled data at the central k-space as done in SENSE. These initial coil sensitivities $\mathbf{s}_l^{(0)}$ are assumed to be known and plugged into Eq. [4.9]. The problem thereby reduces to Sparse SENSE. We then use the image reconstructed from Sparse SENSE as the initial image $\mathbf{f}^{(0)}$ and plug into Eq. [4.9] to update the coil sensitivities.

Subsequently, we alternate between updating the image and updating the coil sensitivities through iterations to obtain a sequence of minimizing ($\mathbf{f}^{(n)}$, $\mathbf{s}_l^{(n)}$) until the energy function stops decreasing. The alternating procedure at the n-th iteration is represented as:

f-step: Fix $\mathbf{s}_l = \mathbf{s}_l^{(n-1)}$, Eq. [4.9] reduces to

$$\begin{aligned}\mathbf{f}^{(n)} &= \arg\min_{\mathbf{f}} E(\mathbf{f}, \mathbf{s}_l^{(n-1)}) \\ &= \arg\min_{\mathbf{f}} \left[\sum_{l=1}^{L} \left\| \mathrm{F}_D \left(\mathbf{s}_l^{(n-1)} \bullet \mathbf{f} \right) - \mathbf{d}_l \right\|^2 + \lambda \left\| \Psi \mathbf{f} \right\|_1 + \alpha \mathrm{TV}(\mathbf{f}) \right],\end{aligned} \tag{4.10}$$

s-step: Fix $\mathbf{f} = \mathbf{f}^{(n)}$, Eq. [4.9] reduces to

$$\begin{aligned}\mathbf{s}_l^{(n)} &= \arg\min_{\mathbf{s}_l} E(\mathbf{f}^{(n)}, \mathbf{s}_l) \\ &= \arg\min_{\mathbf{s}_l} \left[\sum_{l=1}^{L} \left\| \mathrm{F}_D \left(\mathbf{s}_l \bullet \mathbf{f}^{(n)} \right) - \mathbf{d}_l \right\|^2 + \beta \sum_{l=1}^{L} \mathrm{TV}(\mathbf{s}_l) \right].\end{aligned} \tag{4.11}$$

It is seen that each subproblem in [4.10] and [4.11] is convex and thus an optimal solution can be found for each subproblem. We use the nonlinear conjugate gradient (NLCG) algorithm with line search to solve this alternating optimization problem. It is worth noting that the **f**-step of the first iteration of Sparse BLIP is the same as Sparse SENSE, and Sparse BLIP improves the sensitivities estimation of Sparse SENSE through alternating optimization of image and sensitivities. Such alternating minimization can be proved to converge to a local minimum (56) which gives a suboptimal solution to the original nonconvex problem.

4.1.4 Gradient Computation

In the NLCG algorithm, the most important steps are the computation of the gradients of [4.10] and [4.11], which are given by the following equations:

$$\frac{\partial E(\mathbf{f},\mathbf{s}_l^{(n-1)})}{\partial \mathbf{f}} = \sum_{l=1}^{L} 2\left(\mathbf{s}_l^{(n-1)}\right)^* \bullet \mathrm{F}_D^H\left(\mathrm{F}_D\left(\mathbf{s}_l^{(n-1)} \bullet \mathbf{f}\right) - \mathbf{d}_l\right) + \lambda\Psi^*\left((\Psi\mathbf{f})\bullet(\Psi\mathbf{f})^* + \varepsilon\right)^{-1/2} \bullet \Psi\mathbf{f} + \alpha\Delta\left(\left((\nabla\mathbf{f})\bullet(\nabla\mathbf{f})^* + \varepsilon\right)^{-1/2} \bullet \nabla\mathbf{f}\right), \quad [4.12]$$

$$\frac{\partial E(\mathbf{f}^{(n)},\mathbf{s}_l)}{\partial \mathbf{s}_l} = 2\left(\mathbf{f}^{(n)}\right)^* \bullet \mathrm{F}_D^H\left(\mathrm{F}_D\left(\mathbf{s}_l \bullet \mathbf{f}^{(n)}\right) - \mathbf{d}_l\right) + \beta\Delta\left(\left((\nabla\mathbf{s}_l)\bullet(\nabla\mathbf{s}_l)^* + \varepsilon\right)^{-1/2} \bullet \nabla\mathbf{s}_l\right), \quad [4.13]$$

where $(\cdot)^*$ is the conjugate operator, $\mathrm{F}_D^H(\cdot)$ is the conjugate transpose of F_D which is implemented by zero filling followed by the inverse Fourier transform, $\nabla(\cdot)$ is the finite difference operator, $\Delta(\cdot)$ is the self-adjoint of the finite difference operator (6), and the operator $\nabla(\cdot)$ and $\Delta(\cdot)$ are defined below. ε is a small positive smoothing parameter and usually takes a value in the range of $\varepsilon \in [10^{-15}, 10^{-6}]$ (6). In our implementation, we choose $\varepsilon = 10^{-7}$.

Consider a 2-D image f in the spatial domain, and (u, v) is its 2-D coordinate's index. The finite difference operation of f is defined as

$$\nabla(f)_{u,v} = \left[f_{u+1,v} - f_{u,v}, f_{u,v+1} - f_{u,v}\right]. \quad [4.14]$$

The result of the finite difference operation of a 2-D image f in the spatial domain thereby becomes two 2-D finite difference images. We refer to the two finite difference images as the "x-part" and "y-part" of the finite difference domain variable, i.e.,

$$\nabla(f) = \left[\nabla_x f, \nabla_y f\right]. \quad [4.15]$$

Consider a 2-D finite-difference domain variable Df,

$$Df_{u,v} = \left[\nabla_x f_{u,v}, \nabla_y f_{u,v}\right], \quad [4.16]$$

where (u, v) is its 2-D coordinate's index of its "x-part" and "y-part", respectively. The self-

adjoint operator of the finite difference operation of Df is defined as

$$\Delta(Df)_{u,v} = \left(\nabla_x f_{u-1,v} - \nabla_x f_{u,v}\right) + \left(\nabla_y f_{u,v-1} - \nabla_y f_{u,v}\right). \quad [4.17]$$

The result of the self-adjoint of the finite difference operation of a finite-difference domain variable will turn the two 2-D finite difference images back to one single image in spatial domain.

4.2 Methods

The proposed Sparse BLIP method was evaluated on five T_1-weighted datasets: phantom, in vivo brain data with coronal, sagittal, axial views, and in vivo cardiac data. For all in vivo studies, informed consent was obtained from the volunteer in accordance with the Institutional Review Board policy. All reconstruction methods were implemented in MATLAB (MathWorks, Natick, MA) on a workstation. The root sum-of-squares (SOS) reconstruction from fully sampled data was used as the gold standard for visual comparison. All phased array data were acquired in full and then manually undersampled retrospectively to simulate accelerated scans. The state-of-the-art parallel imaging techniques JSENSE (14), Sparse SENSE (7), L_1-SPIRiT (8), and IRGN-TV (18) were used to compare against the proposed Sparse BLIP method. Except for JSENSE where the data are acquired using variable-density uniform undersampling with the central k-space sampled with Nyquist rate as in (14), the same variable-density random sampling pattern was used for all reconstruction methods for fair comparison. Specifically, we choose samples randomly with sampling density scaling according to a power of distance from the k-space center. Usually, using density powers of 1–6 is good to reduce interference (6), and we use a power of 5. The coil sensitivity functions estimated from the central k-space data were used for Sparse SENSE and for the first iteration of the proposed Sparse BLIP.

For the coronal dataset, the initial and final coil sensitivities from Sparse BLIP were used for SENSE (3) reconstructions, which were compared with the conventional GRAPPA (4) reconstruction with a kernel size of 4 blocks and 5 columns. We scaled all undersampled k-space data from all channels by the same constant to have a maximum magnitude value of 1 prior to reconstruction. All reconstructed images for the same dataset were normalized and shown individually on the same scale for visual evaluations of image quality. Quantitative comparison was also provided in terms of the normalized root mean squared error (nRMSE) with the SOS as the reference, which is defined as:

$$\mathrm{nRMSE} = \frac{1}{\max\left(f_{\mathrm{SOS}}\right) - \min\left(f_{\mathrm{SOS}}\right)} \sqrt{\frac{\sum_{u=1}^{U}\sum_{v=1}^{V}\left|\hat{f}\left(u,v\right) - f_{\mathrm{SOS}}\left(u,v\right)\right|^2}{UV}}, \qquad [4.18]$$

where $\hat{f}$ is the reconstructed image and f_{SOS} is the SOS image.

4.2.1 Selection of Regularization Parameters

Although automatic optimization of regularization parameters remains an open problem in the context of compressed sensing, we use an approach named L-surface (69) similar to the L-curve method (70) to automate the parameter selection. At first we optimize only α and β using L-surface while keeping λ=0. The wavelet term parameter λ can be selected at the same order of α after α *and* β are selected. Specifically, we change the values of α and β in a reasonable range. For each pair of (α, β), we carry out the reconstruction and calculate the corresponding values for the three terms in the objective function: data consistency $\sum_{l=1}^{L}\left\|\mathrm{F}_D\left(\mathbf{s}_l \bullet \mathbf{f}\right) - \mathbf{d}_l\right\|^2$, TV of image $\mathrm{TV}\left(\mathbf{f}\right)$, and TV of sensitivities $\sum_{l=1}^{L}\mathrm{TV}\left(\mathbf{s}_l\right)$. We then plot an L-surface in 3-D over a wide range of regularization parameters where the vertical axis

represents the value of data consistency terms, and the two horizontal axes are the values of the TV of image term and the TV of sensitivities term. To construct the surface, we connect the line segments between points with constant α and varying β, and then connect line segments between points with constant β and varying α. Thereby each point on the surface corresponds to a particular (α, β) pair, and the corresponding values on the three axes represent the values of data consistency, TV of image, and TV of sensitivities for this (α, β) pair. The "optimal region" is located at the "corner" of the L-surface—the region analogous to the corner of the traditional L-curve for a single regularization constraint. The optimal parameters are the (α, β) pair at the "optimal region" (69). Usually, it takes 7×7 tests of (α, β) pairs to construct the L-surface and identify the "optimal region".

To give a fair comparison, the parameters for other competing methods were also chosen by the L-surface method. The parameters for Sparse SENSE include λ for the wavelet term and α for total variation. The parameters for L1-SPIRiT are λ_1 for autocalibration and λ_2 for the wavelet term. The parameters for IRGN-TV include α_k for the high Fourier coefficients of the sensitivities from the k-th iteration, β_k for the generalized total variation from the k-th iteration, the scaling factors q_α, q_β for α_k, β_k in each iteration, and the minimum α_{min} and β_{min}. JSENSE is only tested for the 2-D phantom and in vivo experiments. A uniform sampling pattern is used for JSENSE, which includes the central Nyquist samples fully sampled and outer samples uniform undersampled.

4.2.2 Initialization

The coil sensitivities are initially estimated with the standard approach where each channel image obtained from windowed, Nyquist-sampled central k-space data is divided by the SOS image of all channels. This is called the low resolution estimation method.

These estimated coil sensitivities were then used for JSENSE, IRGN-TV, Sparse SENSE, and Sparse BLIP.

4.2.3 Stopping Criterion

For Sparse BLIP, we find that even though the energy function $E(\mathbf{f}, \mathbf{s}_l)$ keeps decreasing over AM iterations, the data consistency term usually stops decreasing after several iterations. As a result, the quality of the reconstructed image hardly improves afterwards (a similar observation was made in (8) for L1-SPIRiT). This leads to an effective stopping criterion for Sparse BLIP. Specifically, we define the root mean squared error (RMSE) of the under-sampled data as

$$\text{RMSE} = \sqrt{\frac{\sum_{l=1}^{L} \left\| \mathrm{F}_D(\mathbf{s}_l \bullet \mathbf{f}) - \mathbf{d}_l \right\|^2}{\sum_{l=1}^{L} \#(\mathbf{d}_l)}}, \qquad [4.19]$$

where $\#(\mathbf{d}_l)$ denotes the number of elements in $\mathbf{d}_l$. The RMSE is computed after each **f**-step and **s**-step. If within an AM iteration, the RMSE of **s**-step is larger than that of **f**-step, then we stop the algorithm because it is unlikely that additional AM iterations will improve the RMSE further.

4.2.4 Phantom Experiment

The objective of the phantom experiment is to evaluate the performance of the proposed method when the sparseness constraint is satisfied. A phantom that is piecewise-constant was used to meet the requirement that the finite difference of the image is sparse and thus the TV is small. A T1-weighted scan was performed on the phantom using a two-dimensional spin echo sequence on a 3T commercial scanner (GE Healthcare, Waukesha,

WI) with an 8-channel torso coil (echo time/pulse repetition time = 11/300 ms, FOV = 18 × 18 cm, matrix = 256 × 256, slice thickness = 1.7 mm). The k-space data were randomly undersampled along the phase encoding direction with a variable-density sampling pattern (6). The undersampled k-space data included a total of 40 random phase-encoding lines with the central 24 lines Nyquist sampled, and the net reduction factor was 6.4. This is relatively high reduction factor for an 8-coil dataset.

4.2.5 In vivo Brain Imaging Experiment: Coronal View

This experiment is to examine the performance of the proposed method when reconstructing in vivo coronal brain images which have few fine structures and thus are close to the prior model. A T_1-weighted scan was performed using a 2-D spin echo sequence on a 3T commercial scanner (Magnetom Trio, Siemens Healthcare Sector, Erlangen, Germany) with a 32-channel head coil (TR = 100ms, TE = 2.29s, FOV = 24 × 24 cm, matrix = 256 × 256, slice thickness = 3 mm, Flip Angle = 25). To reduce the computational complexity, 8 out of 32 channels were used for reconstruction. The undersampled k-space data were composed of a variable density sampling pattern that has a total of 88 random phase-encoding lines with 32 Nyquist-sampled central lines, corresponding to a net reduction factor of 2.91.

4.2.6 In vivo Brain Imaging Experiment: Sagittal View

This experiment is to evaluate the proposed Sparse BLIP when there are many fine structures with different contrast in the images to be reconstructed. A set of sagittal data was acquired on a GE 3T scanner (GE Healthcare, Waukesha, WI) with an 8-channel head coil and a 3-D T_1-weighted spoiled gradient echo sequence (TE = minimum full, TR = 500

ms, FOV = 24 × 24 cm, matrix = 256 × 256). A total of 92 phase-encoding lines were acquired with the variable density sampling pattern which has central 24 lines fully sampled and the rest randomly sampled. The net reduction factor was 2.78.

4.2.7 In vivo 3-D Brain Imaging Experiment: Axial View

A T_1-weighted, inversion recovery prepared 3-D spoiled gradient echo (SPGR) sequence was used to obtain a fully sampled high resolution dataset of a brain of a healthy volunteer. The scan was performed on a GE Signa-Excite 1.5-T scanner, using an 8-channel receive coil. The scan parameters were echo time = 8 ms, pulse repetition time= 17.6 ms, flip = 20°, BW = 6.94 khz. The data were downloaded from http://www.eecs.berkeley.edu/~mlustig/Software.html. The field of view was 20×20×20 cm, with a matrix size of 200×200×200, corresponding to isotropic 1 mm^3 resolution. A 2-D undersampling pattern was exploited along the phase and slice encoding directions according to a variable-density sampling pattern (6). The sampling pattern has a net reduction factor of 4 with an 8×8 Nyquist-sampled region at the center of k-space for calibration. This is a relatively high reduction factor for a 8-coil dataset in practice.

4.2.8 In vivo Cardiac Imaging Experiment

This experiment is to examine the performance of the proposed method when applied to one frame of in vivo cardiac data, where air-tissue boundaries induce sharp transitions in the estimated coil sensitivities. The dataset was acquired from a 3T scanner (Siemens Trio, Erlangen, Germany), with a 12-channel phased array coil (combined to 4 coils), using a 2-D true FISP sequence (TE = 1.87 ms, TR = 29.9 ms, BW = 930, flip = 50°, FOV = 34 × 28.6875 cm, matrix = 256 × 216, slice thickness = 6 mm). A total of 82 phase-encoding

lines were acquired with a variable density random sampling and 24 fully sampled central lines. The net reduction factor was 2.63. This dataset is different from the other datasets in that it has different size in the x and y dimension. So it is a little tricky for the wavelet term to run smoothly and has to extend it to 256 × 256 during the wavelet transform.

4.3 Results

4.3.1 Phantom Experiment

For the phantom data, Figure 4.1 presents the images reconstructed using five different methods, JSENSE, Sparse SENSE, IRGN-TV, L_1-SPIRiT, and the proposed Sparse BLIP. The parameters of all methods were selected based on the L-surface method. The values for these parameters are: $\lambda = 1\times10^{-6}$, $\alpha = 5\times10^{-6}$, $\beta = 2\times10^{-4}$ for the proposed Sparse BLIP, $\lambda=1\times10^{-6}$, $\alpha=5\times10^{-6}$ for Sparse SENSE, $\alpha_0=1$, $\beta_0=1$, $q_\alpha=0.1$, $q_\beta=0.2$, $\alpha_{min}=0$, $\beta_{min}= 0.005$ for IRGN-TV, and $\lambda_1=0.001$, $\lambda_2=0.02$ for L_1-SPIRiT. For this phantom data, we observe that at the high reduction factor of R=6.4, the proposed Sparse BLIP has less aliasing across the whole image when compared with JSENSE, Sparse SENSE, IRGN-TV, and L_1-SPIRiT. The nRMSE of each reconstructed image, as defined in Eq. [4.12], is shown in Table 4.1 (see the row corresponding to the phantom dataset). It is seen that the nRMSEs of JSENSE, IRGN-TV, and L_1-SPIRiT are about three to four times higher than that of the first iteration of Sparse BLIP. The nRMSE of Sparse BLIP continues to decrease over subsequent AM iterations and it converges in four iterations. This is consistent with visual inspection that Sparse BLIP has less aliasing than other methods for the phantom dataset. The phantom results demonstrate that when the model is fairly accurate, the proposed method is able to reconstruct high quality images at high reduction factors. We also compare the initial and final estimated coil sensitivities of a single channel using Sparse BLIP against that

estimated using the full data (named "SOS sensitivities") on the bottom of Figure 4.1. The comparison shows that the iterative updating procedure gradually smoothens the sensitivity function, and the final estimated sensitivity looks more smooth and continuous than the initial estimate.

4.3.2 In vivo Coronal Experiment

Reconstructions for the coronal data are shown in Figure 4.2 at a reduction factor of R=2.91. When using the L-surface method, the parameters were chosen as $\lambda = 2\times10^{-6}$, $\alpha = 2\times10^{-6}$, $\beta = 2\times10^{-5}$ for Sparse BLIP, $\lambda=2\times10^{-6}$, $\alpha=2\times10^{-6}$ for Sparse SENSE, $\lambda_1=0.01$, $\lambda_2=0.0015$ for L1-SPIRiT, and $\alpha_0=1$, $\beta_0=1$, $q_\alpha=0.1$, $q_\beta=0.2$, $\alpha_{min}=0$, $\beta_{min}=0$ for IRGN-TV. It shows in Figure 4.2 that Sparse BLIP largely suppressed the aliasing artifacts that are present in other methods. The arrows in the images highlight the regions where aliasing are most prominent. Quantitatively, the nRMSE of Sparse BLIP is lower than those of other methods, as shown in Table 4.1. We also show the initial, final, and SOS sensitivities on the bottom of Figure 4.2. The conclusion is consistent with that from Figure 4.1. To further validate the accuracy of the final sensitivities, we use both the initial and final sensitivities obtained by Sparse BLIP to perform the conventional SENSE (i.e., uniform sampling without regularization), and the reconstructions are contrasted with conventional GRAPPA, which is known to be less prone to aliasing artifacts due to inaccurate coil calibrations than SENSE (3). The comparison in Figure 4.3 demonstrates that the SENSE reconstruction obtained using the final sensitivities is able to suppress the aliasing that is present in the reconstruction using the initial sensitivities and achieve a quality similar to that of GRAPPA. This suggests that the final sensitivities may be closer to the true ones than the initial sensitivities do. Such an improvement from Sparse BLIP is important because it

would enable more accurate image-space-based parallel imaging.

We also use this dataset as an example to demonstrate how the parameters are selected using the L-surface method (69). Figure 4.4 shows the L-surface in the range of $\alpha \in [8\times10^{-9}, 2\times10^{-3}]$ and $\beta \in [8\times10^{-8}, 5\times10^{-6}]$, where the mesh becomes denser near the "optimal region" labeled with a circle. Different (α, β) pairs near the "optimal region" have similar performance which makes the choice of optimal parameters less stringent. For this particular dataset, we found that any parameters within $\alpha \in [2\times10^{-6}, 1\times10^{-5}]$, $\beta \in [2\times10^{-5}, 5\times10^{-4}]$ can generate similar reconstructions.

4.3.3 In vivo Sagittal Experiment

Figure 4.5 shows reconstructions of the sagittal image. The parameters of the Sparse BLIP are $\lambda = 5\times10^{-6}$, $\alpha = 5\times10^{-6}$, $\beta = 5\times10^{-4}$, Sparse SENSE $\lambda=5\times10^{-6}$, $\alpha=5\times10^{-6}$, L_1-SPIRiT $\lambda_1=0.01$, $\lambda_2=0.0015$, and IRGN-TV $\alpha_0=1$, $\beta_0=1$, $q_\alpha=0.1$, $q_\beta=0.2$, $\alpha_{min}=0$, $\beta_{min}=0$. As indicated by the arrows, aliasing artifacts are present in IRGN-TV, Sparse SENSE, JSENSE, and L_1-SPIRiT reconstructions, but are largely suppressed in the Sparse BLIP reconstruction. This is consistent with the results of Table 4.1, which indicates that other methods have higher nRMSEs than that of Sparse BLIP. In Table 4.2, we present the RMSE for the first 4 iterations where both **f**-step and **s**-step reduce the RMSE in the first 3 and then the RMSE starts to increase and the iteration terminates.

4.3.4 In vivo Axial Experiment

The axial reconstructions from the 3-D data are shown in Fig. 4.6. The parameters are $\lambda = 8\times10^{-6}$, $\alpha = 8\times10^{-6}$, $\beta = 2\times10^{-4}$ for Sparse BLIP, $\lambda=8\times10^{-6}$, $\alpha=8\times10^{-6}$ for Sparse SENSE, $\lambda_1=0.01$, $\lambda_2=0.0015$ for L_1-SPIRiT, and $\alpha_0=1$, $\beta_0=1$, $q_\alpha=0.1$, $q_\beta=0.2$, $\alpha_{min}=0$, $\beta_{min}=0$ for

IRGN-TV. At a reduction factor of 4 with 2-D undersampling, Sparse BLIP is still able to achieve a reconstruction that is visually close to the SOS reconstruction, while other methods cannot preserve the same image quality. From Table 4.1, Sparse BLIP reconstructions have about 20% lower nRMSE than other reconstructions.

4.3.5 In vivo Cardiac Experiment

Figure 4.7 shows reconstructions of the cardiac image. The parameters of Sparse BLIP are $\lambda = 2\times10^{-6}$, $\alpha = 2\times10^{-6}$, $\beta = 2\times10^{-5}$, Sparse SENSE $\lambda=2\times10^{-6}$, $\alpha=2\times10^{-6}$, L_1-SPIRiT $\lambda_1=0.05$, $\lambda_2=0.01$, and IRGN-TV $\alpha_0=0.001$, $\beta_0=0.001$, $q_\alpha=1$, $q_\beta=1$, $\alpha_{min}=0$, $\beta_{min}=0$. As indicated by the arrows, artifacts are present in Sparse SENSE, JSENSE, and L_1-SPIRiT reconstructions and certain structures are lost in IRGN-TV. The sparse BLIP reconstruction is still able to reduce artifacts and preserve details. The lower nRMSE of Sparse BLIP compared to those of other methods is shown in Table 4.1.

4.3.6 Influence of Regularization Parameters

Similar to other compressed sensing algorithms, the performance of the proposed Sparse BLIP method depends on the choice of regularization parameters λ, α, and β. Here, we compare the Sparse BLIP reconstructions of the cardiac data using different sets of parameters in Figure 4.8. The SOS reconstruction and the reconstruction with optimal parameters ($\lambda = 2\times10^{-6}$, $\alpha = 2\times10^{-6}$, $\beta = 2\times10^{-5}$) are shown on the top row as references. It is seen from the 2nd row that when the two TV terms are included in the energy function, reconstruction without the wavelet term ($\lambda = 0$) yields slightly inferior image quality and nRMSE to those obtained using the optimized value of $\lambda = 2\times10^{-6}$. We can see that the image in Figure 4.8b has a higher resolution and has less aliasing artifacts than that in

Figure 4.8d (see the region pointed by the arrow), which justifies the inclusion of wavelet penalty in the problem formulation. Large value of λ, however, could cause a loss of details. The 3rd row demonstrates that small regularization parameter α for the image leads to noisy reconstruction with aliasing artifacts, while large α makes the reconstruction blurry and lacks details. The 4th row shows that when β is too small, the Sparse BLIP reconstruction is very close to that of Sparse SENSE. While if β is too large, the reconstruction has aliasing artifacts due to inaccurate sensitivities.

4.3.7 Influence of Different Initialization

It is known that the performance of Sparse SENSE relies heavily on the estimated sensitivities. In contrast, we find that the final reconstruction of the proposed Sparse BLIP is not as sensitive to the initial estimated sensitivities. This is demonstrated in Figure 4.9 where different distributions between the number of Nyquist-sampled lines (ACS) and the number of randomly undersampled lines are used with the net reduction factor fixed. The reason that we maintain the same net reduction factor is because the reconstructions of both methods will improve if the net reduction factor decreases with increasing ACS lines and it is difficult to distinguish whether such an improvement is due to the increase in ACS lines or in the total acquisition lines. When the ACS lines become fewer, the Sparse SENSE reconstruction becomes obviously inferior, while Sparse BLIP is still able to maintain a similar visual quality with a slightly increased nRMSE and some loss of resolution. The figure shows how Sparse BLIP improves the reconstructions over iterations with Sparse SENSE as the initial estimate. The result suggests that, when the coil sensitivity is well represented by the piecewise-smooth model, Sparse BLIP takes advantages of the prior information on coil sensitivities by iteratively updating their values, while Sparse SENSE

only utilizes the central Nyquist sampled ACS data to obtain the sensitivities information.

4.3.8 Computation Complexity

Sparse BLIP typically requires 3 or 4 AM iterations to converge. The **f**-step and **s**-step in each AM iteration are implemented using the NLCG algorithm that takes 40~50 iterations for convergence. The complexity of Sparse BLIP per AM iteration is slightly higher than that of Sparse SENSE because the latter involves only the **f**-step. Since Sparse BLIP requires multiple AM iterations, its complexity can be several times higher than that of Sparse SENSE. For instance, in our reconstruction of the in vivo sagittal brain dataset, the computer running time of Sparse BLIP, JSENSE, Sparse SENSE, L_1-SPIRiT, and IRGN-TV is 113 seconds (for 3 AM iterations), 172 seconds, 25 seconds, 40 seconds, and 213 seconds, respectively.

4.4 Discussion

4.4.1 Relation to Previous Works

There are several previous methods that attempt to jointly estimate image and sensitivities simultaneously (14,18,67,68). The success of these methods and Sparse BLIP depends on the accuracy of the prior information incorporated in the image and coil sensitivity models. The method in (68) exploits the sparseness of coil sensitivities using polynomial or Fourier transforms. There are no regularizations on the image in the objective function, and thus the prior information of the image is not used. Both (18,67) employ TV regularization for the image and simultaneously impose a smoothness constraint on the coil sensitivities. The IRGN-TV method in (18) uses a weighted L_2 norm to penalize high frequencies of the coil sensitivities, and (67) uses a L_2 norm of the high-

order gradient as the constraint for sensitivities instead. The key difference between Sparse BLIP and methods of (18,67) is that Sparse BLIP uses the total variation constraint in both image and coil sensitivities. There are two key differences between Sparse BLIP and methods of (18,67). First, Sparse BLIP uses the total variation constraint, instead of the L_2 norm as in (18) and (67), for both image and coil sensitivities. Second, the optimization method used in Sparse BLIP is based on alternating optimization, whereas (18) and (67) use the Gauss-Newton method. Due to the nonconvexity of the minimization problems addressed here, different optimization algorithms yield different behavior in local optimality. These result in the difference in reconstruction qualities. It is evident from the Results section that the TV penalty of the coil sensitivities combined with alternating minimization is more appropriate for the datasets used here, resulting in superior reconstructions for the same number of measurements. We acknowledge, however, since such TV penalty is not universal, it might not be the best model in some scenarios other than those tested in this study. Higher order differentiation operators (71) or nonlocal total variations (72) may be useful as alternative penalty functions for Sparse BLIP when the traditional total variation representation is inadequate such as in applications with rapidly varying coil sensitivities from small coil elements.

4.4.2 Sampling Pattern Selection

Based on the compressed sensing theory (5,31) and analysis in Sparse MRI (6), a key requirement of successful recovery is that the sampling must be incoherent, meaning that the aliasing introduced by undersampling should be noise-like (5,6,31). Random sampling is known to satisfy the incoherent requirement and variable density random undersampling with denser sampling close to the center of the k-space has the additional benefit of

improved SNR (6). Figure 4.10 compares the Sparse BLIP reconstruction results of random and uniform undersampling patterns using the 2-D sagittal datasets. The top row presents the sampling patterns used where the white lines indicate the acquired readout lines. The random sampling has a variable density with a total of 92 lines and the uniform one has the same total number of lines with 38 fully sampled ones in the center. For uniform sampling, conventional GRAPPA (4) reconstruction is also shown for comparison. A kernel size of 4 blocks and 5 columns was used. The results confirm that random undersampling provides better reconstructions than uniform undersampling for the proposed method.

4.4.3 Gain over Sparse SENSE and JSENSE

While Sparse BLIP can improve the reconstruction quality of Sparse SENSE and JSENSE for the same reduction factor, the advantage of Sparse BLIP also lies in its ability to reconstruct images of the same quality using fewer acquired samples, especially fewer central k-space samples. It is therefore of interest to see how much acceleration that Sparse BLIP could bring compared to Sparse SENSE and JSENSE. While it largely depends on the particular dataset and sampling patterns, we use the in vivo sagittal dataset as an example to examine the additional acceleration. For Sparse BLIP shown in Figure 4.11b and Figure 4.12b, we use 24/92 to represent that a total of 92 phase-encoding lines were acquired with the variable density sampling pattern, which has 24 fully sampled ACS lines and the rest 68 lines randomly sampled. This corresponds to reduction factor R=256/92=2.78. In Figure 4.11 c-f, we increase the number of ACS lines and total phase encoding lines to examine the performance improvement in Sparse SENSE. This is in light of the observation from Figure 4.9 that the performance of Sparse SENSE is sensitive to the number of ACS lines. As shown in Figure 4.11 c-e, Sparse SENSE suffers from aliasing

(refer to the arrow in each figure) despite increased number of ACS lines and phase encoding lines. In Figure 4.11f, we observe that Sparse SENSE generates a reconstruction with a similar nRMSE and visual quality as Sparse BLIP, while requiring 16 additional readout lines. This shows that Sparse BLIP has a gain of 16/108=15% in acceleration over Sparse SENSE. Similarly, in Figure 4.12 c-f, we increase the number of total phase encoding lines for JSENSE with ACS/total lines being 38/92, 22/100, 34/108, and 40/112, respectively. As shown in Figure 4.12 c-f, JSENSE suffers from aliasing (refer to the arrow in each figure) even when 112 lines are acquired. This shows that the TV constraints are important and Sparse BLIP has a gain of at least 20/112=18% in acceleration over JSENSE.

4.5 Conclusion

We propose a new method, Sparse BLIP, to jointly reconstruct the image and coil sensitivities from undersampled multichannel phased-array data. Phantom and in vivo experimental results demonstrate that Sparse BLIP provides reconstructions superior to those using IRGN-TV, Sparse SENSE, JSENSE, and L_1-SPIRiT both qualitatively and quantitatively. In particular, Sparse BLIP is robust to the initial estimate of coil sensitivities and the algorithm converges to a high quality image reconstruction after a small number of joint image and sensitivities updates.

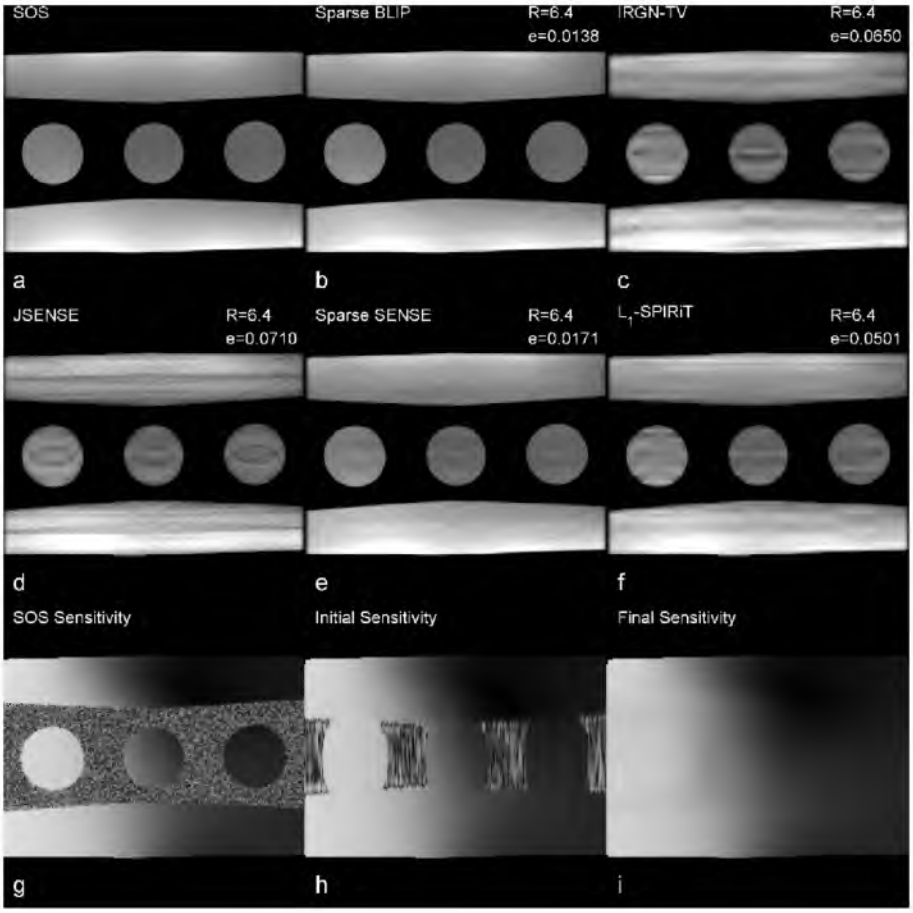

Figure 4.1 Comparison of reconstructions for the phantom dataset. The reconstruction images of SOS, Sparse BLIP, IRGN-TV, JSENSE, Sparse SENSE, and L_1-SPIRiT are shown in (a) – (f). The method used for image reconstruction is shown on the top left corner of each image and the net reduction factors "R" and the nRMSE "e" are shown on the top right corner. For the high reduction factor of R = 6.4, the proposed Sparse BLIP yields a reconstruction with much less aliasing than IRGN-TV, JSENSE, Sparse SENSE, and L_1-SPIRiT. The sensitivity estimated from the fully sampled data (SOS sensitivities), the initial, and final sensitivities of channel #1 estimated from Sparse BLIP are shown in (g) – (i). While the initial sensitivity of Sparse BLIP has errors in the regions where the image has low intensity, the final estimation is able to recover the smoothness of the sensitivity function.

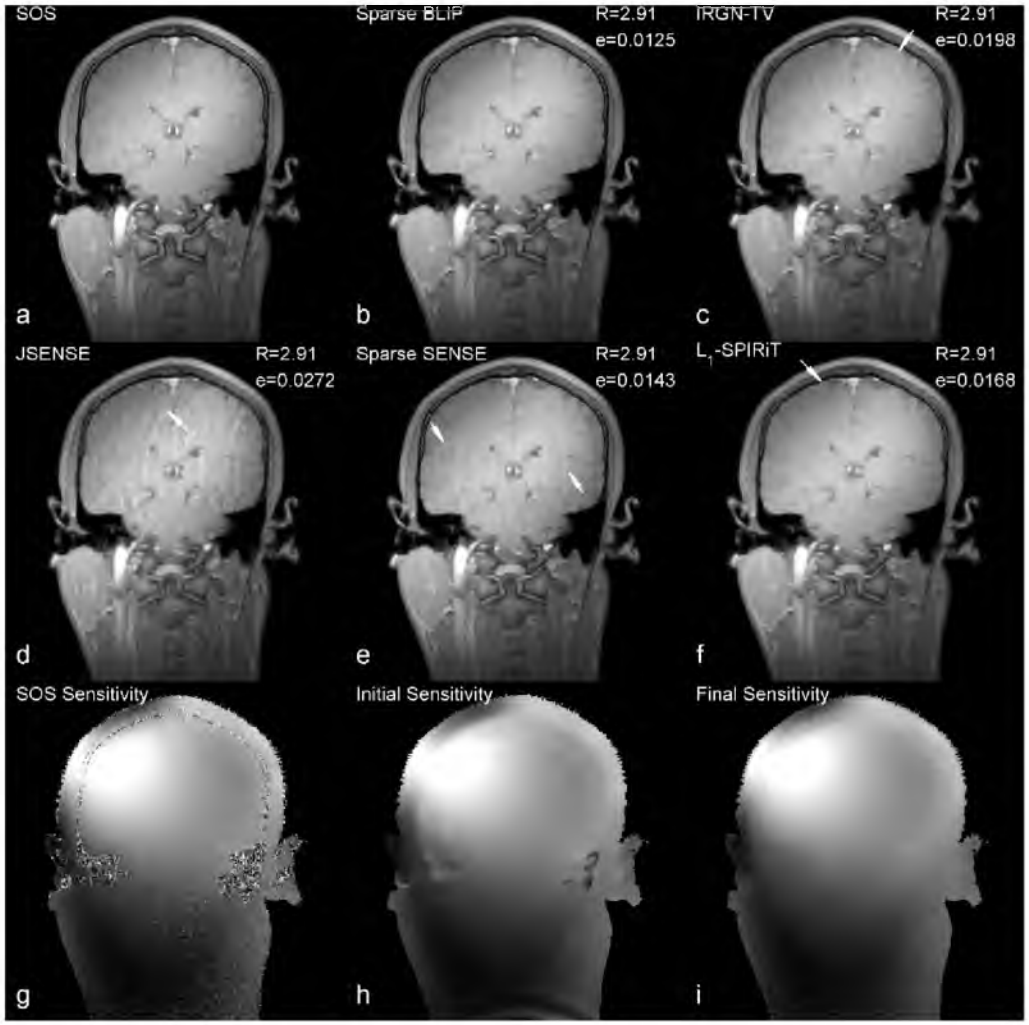

Figure 4.2 Comparison of reconstructions for the coronal dataset. The reconstruction images of SOS, Sparse BLIP, IRGN-TV, JSENSE, Sparse SENSE, and L_1-SPIRiT are shown in (a) – (f). For the reduction factor of R = 2.91, the proposed Sparse BLIP method has less aliasing and preserves more details than IRGN-TV, JSENSE, Sparse SENSE, and L1-SPIRiT. The arrows in the reconstructed image for Sparse SENSE point to the vertical white stripes that extend from the top of the image to the center due to aliasing. Similar aliasing artifacts, as indicated by the arrows, are also present in the reconstructed image for IRGN-TV, JSENSE, and L1-SPIRiT. The SOS, initial, and final sensitivities estimated by Sparse BLIP for channel #1 are shown in (g) – (i). The conclusion is consistent with that from Figure 4.1 that the final estimated sensitivity represents the smooth and continuous nature of the sensitivity function more accurately.

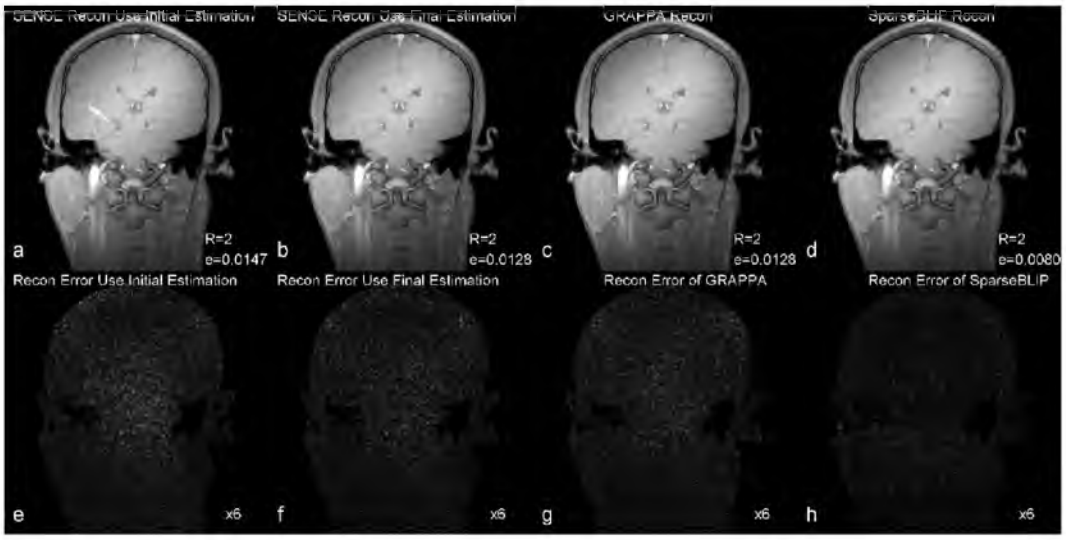

Figure 4.3 Using SENSE reconstruction to show the improvement of the sensitivities estimation from Sparse SENSE to Sparse BLIP. SENSE reconstructions using the initial sensitivities of Sparse SENSE (a) and final sensitivities of Sparse BLIP (b), GRAPPA reconstruction (c), and Sparse BLIP reconstruction (d) are shown for comparison. The reduction factor of R = 2 is used. The aliasing artifacts that appear in the SENSE reconstruction with the initial sensitivities are suppressed in that with the final sensitivities. The SENSE reconstruction using the final sensitivities achieves a reconstruction quality similar to GRAPPA. Sparse BLIP, which has the lowest nRMSE, is able to suppress the noise present in SENSE and GRAPPA reconstructions.

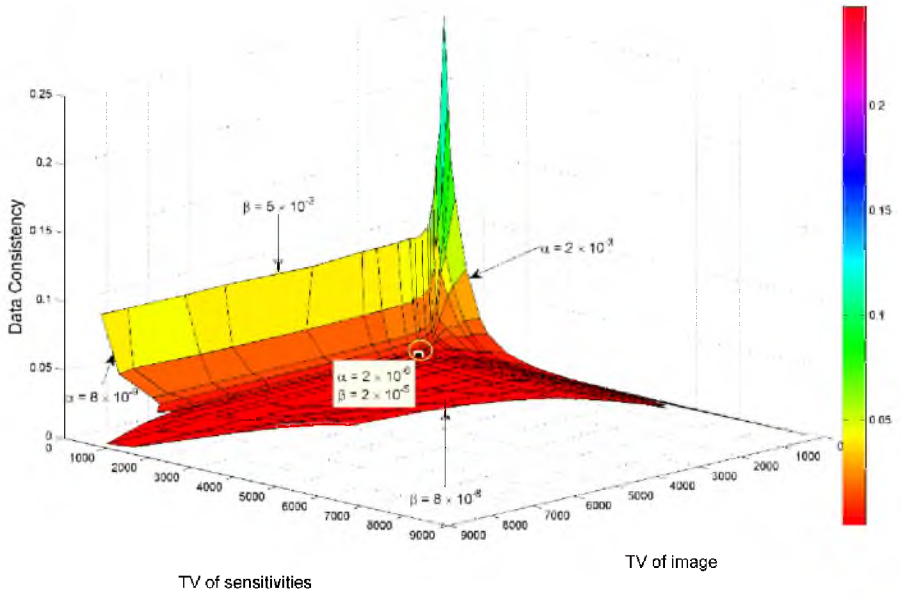

Figure 4.4 Illustration of the L-surface method for automated parameter selection using the coronal brain dataset. Each point in the 3-D space corresponds to a pair of parameters (α and β) used for Sparse BLIP. The three coordinates of a given point correspond to the values of the data consistency, TV of image, and TV of sensitivities, respectively. A surface is generated by varying (α and β) in a certain range. The optimal parameters are located at the circled corner of the L-surface.

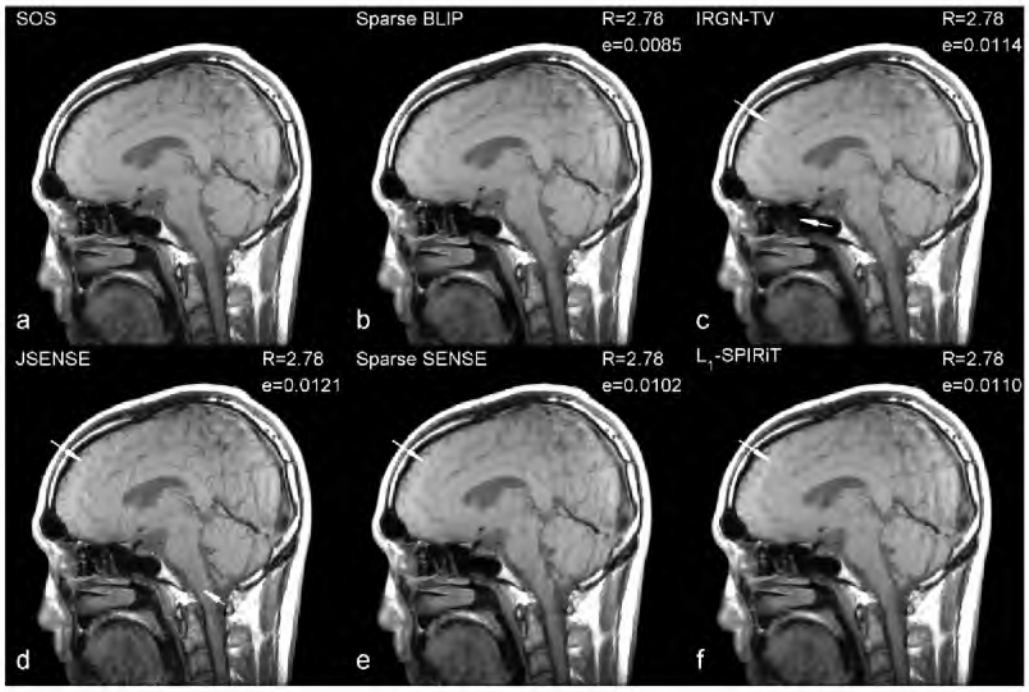

Figure 4.5 The reconstructed images for the sagittal dataset at R = 2.78 are shown for comparison. The reconstruction images of SOS, Sparse BLIP, IRGN-TV, JSENSE, Sparse SENSE, and L_1-SPIRiT are shown in (a) – (f). We can see that the Sparse BLIP method is able to suppress the aliasing artifacts that are present in IRGN-TV, JSENSE, Sparse SENSE, and L1-SPIRiT reconstruction. The aliasing artifacts are indicated by arrows in each image.

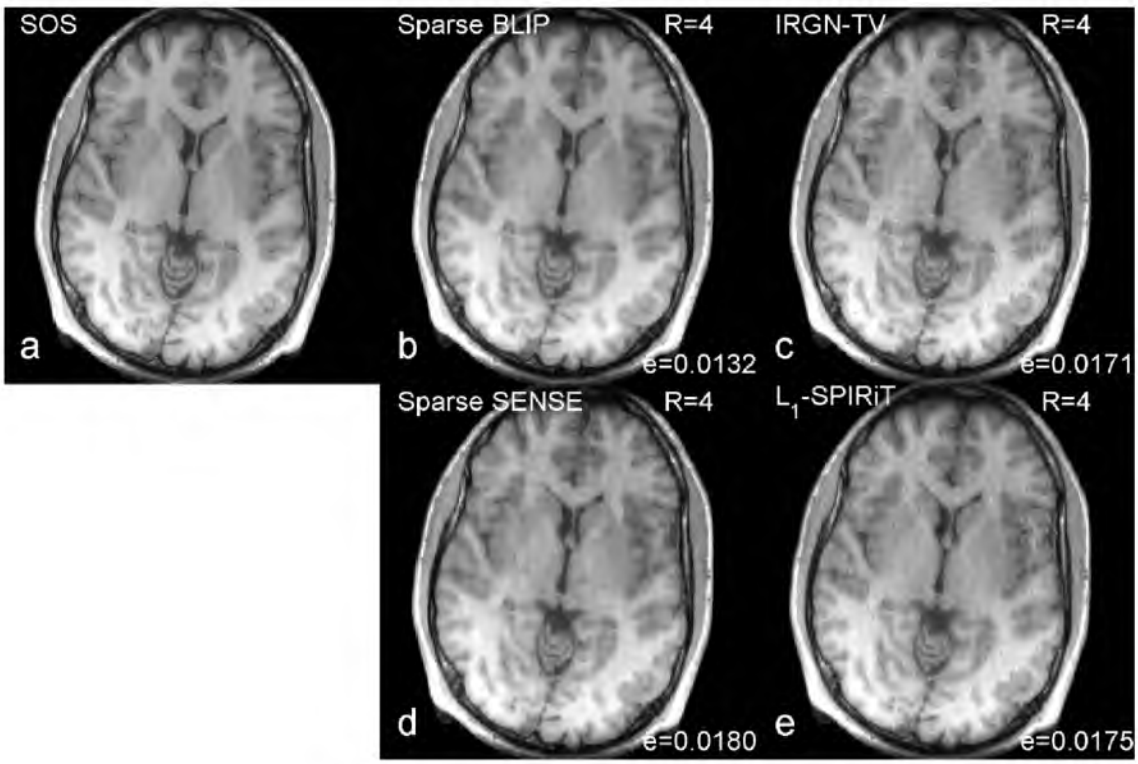

Figure 4.6 Comparison of the axial reconstructions of a 3-D brain dataset with a 2-D reduction factor of 4. The reconstruction images of SOS, Sparse BLIP, IRGN-TV, Sparse SENSE, and L_1-SPIRiT are shown in (a) – (e). Among all methods, the proposed Sparse BLIP method is able to reconstruct an image with the least reconstruction error.

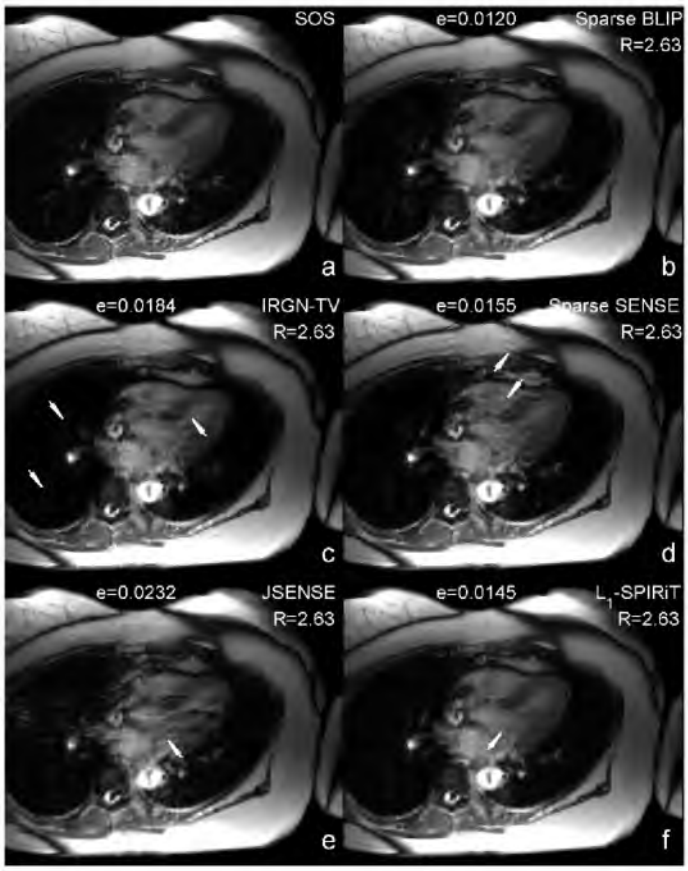

Figure 4.7 Comparison of reconstruction results for the cardiac dataset. The reconstruction images of SOS, Sparse BLIP, IRGN-TV, Sparse SENSE, JSENSE, and L_1-SPIRiT are shown in (a) – (f). The results show that, at R = 2.63, the proposed Sparse BLIP method has less aliasing and preserves more details than IRGNTV, Sparse SENSE, JSENSE, and L_1-SPIRiT. The two arrows on the left in the reconstructed image of IRGN-TV show the loss of structural details. The other arrows in the figures show the aliasing artifacts.

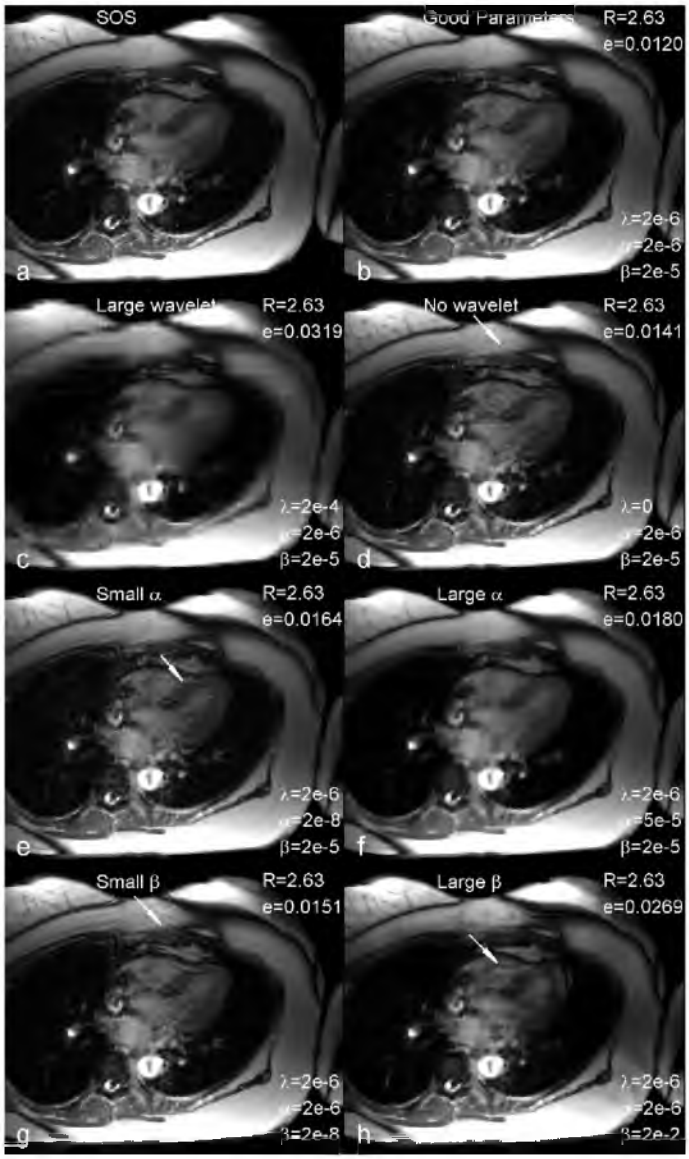

Figure 4.8 Illustration of the influence of regularization parameters λ, α, and β. The SOS is shown in (a), result of Sparse BLIP with the regularization parameters λ=2e-6, α=2e-6, β=2e-5 is shown in (b), λ=2e-4, α=2e-6, β=2e-5 is shown in (c), λ=0, α=2e-6, β=2e-5 is shown in (d), λ=2e-6, α=2e-8, β=2e-5 is shown in (e), λ=2e-6, α=5e-5, β=2e-5 is shown in (f), λ=2e-6, α=2e-6, β=2e-8 is shown in (g), λ=2e-6, α=2e-6, β=2e-2 is shown in (h), The values of these parameters are shown on the bottom right corner of each image. The reduction factor "R" and the corresponding nRMSE "e" are shown on the top right corner of each image. In the first row, the left image is obtained by SOS, and the right image is obtained by Sparse BLIP with optimally chosen parameters. In rows 2–4, we examine the effect of changing one of the parameters λ, α, and β, respectively, while keeping the other two parameters fixed at their optimal values. The images and nRMSEs indicate that the reconstruction can suffer from noise, aliasing artifacts, or loss of details when the parameters are not chosen properly either too small, or too large from the optimal values.

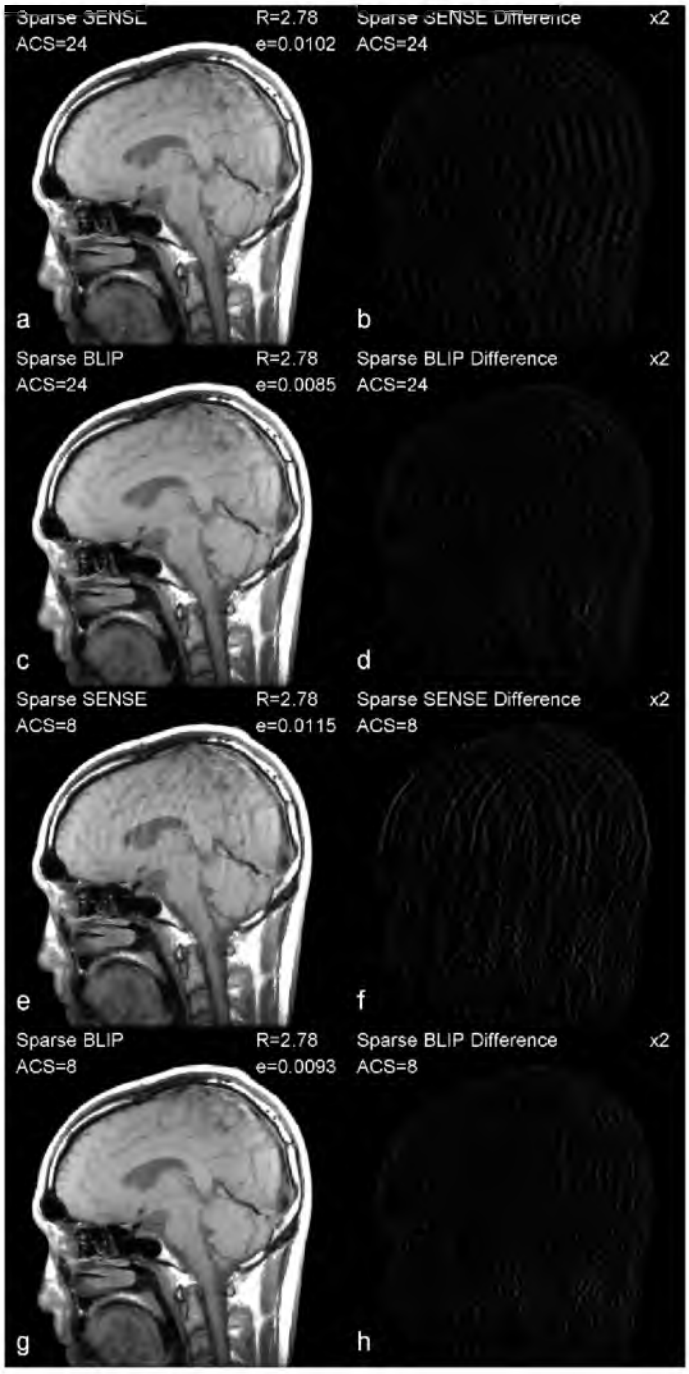

Figure 4.9 Comparison of sagittal reconstructions with different ACS lines for a fixed reduction factor R = 2.78. Sparse SENSE and Sparse BLIP reconstruction of 24 ACS lines are shown in (a) and (c), the difference images are shown in (b) and (d). Sparse SENSE and Sparse BLIP reconstruction of 8 ACS lines are shown in (e) and (g), the difference images are shown in (f) and (h). The proposed Sparse BLIP method is able to achieve similar reconstructions with decreasing numbers of ACS lines, while Sparse SENSE relies on a larger number of ACS lines to estimate the coil sensitivities accurately.

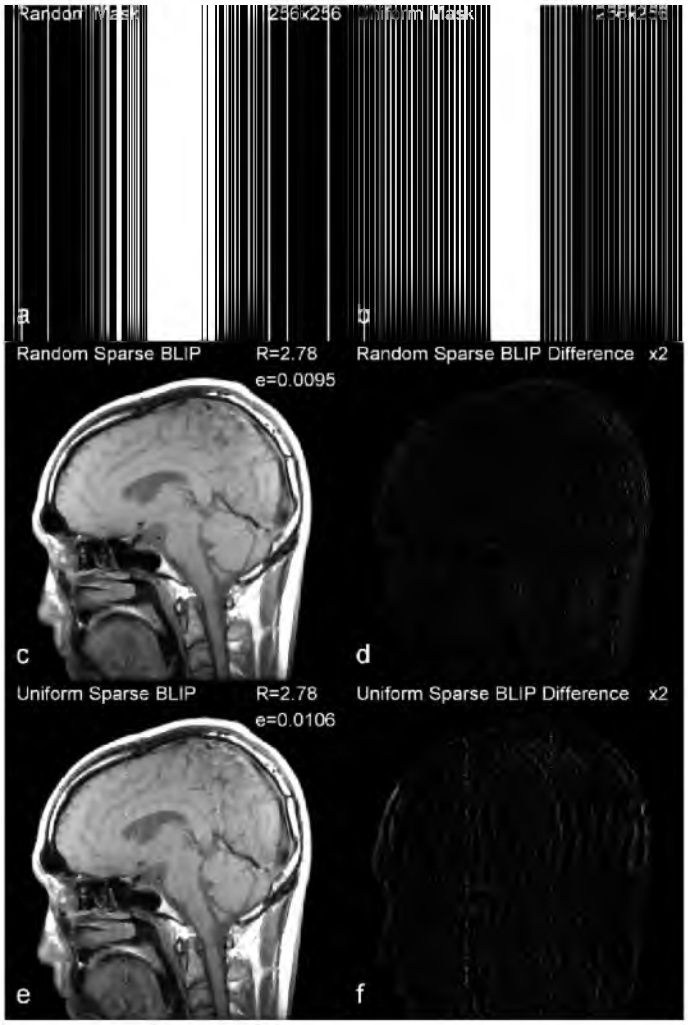

Figure 4.10 Comparison of Sparse BLIP reconstructions using variable density random undersampling and uniform undersampling pattern for the in vivo sagittal datasets. The random (a) and uniform (b) sampling patterns with white lines representing the acquired k-space locations are shown. The reconstructions from the random sampling pattern and the difference images with the reference are shown in (c) and (d). The reconstructions from the uniform sampling pattern and the difference images with the reference are shown in (e) and (f). We can see that Sparse BLIP using random sampling gives better reconstruction quality than uniform sampling.

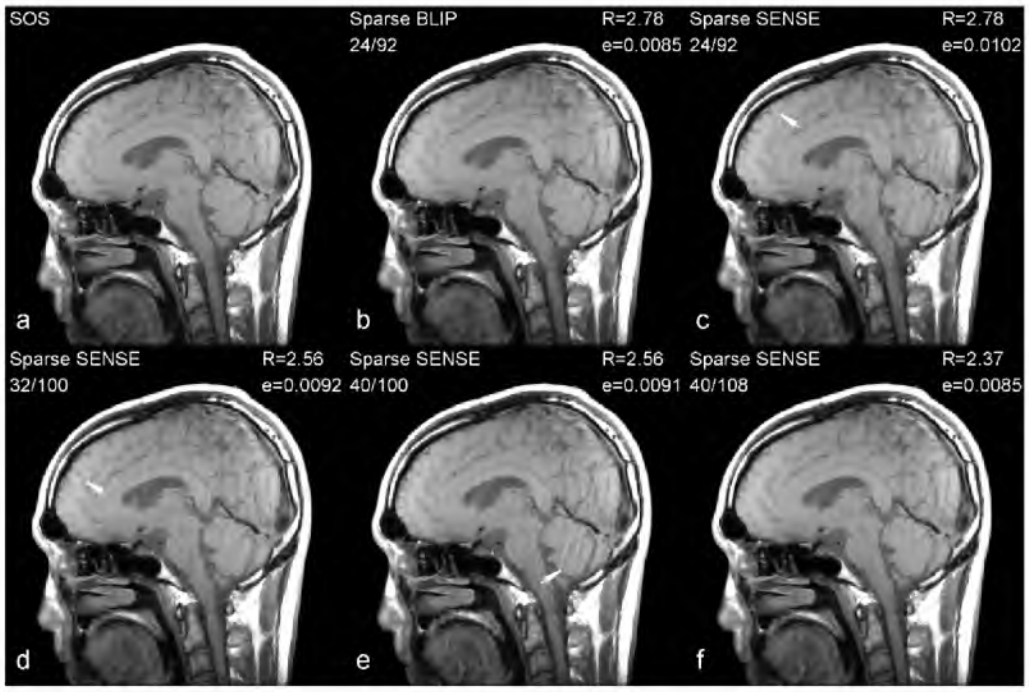

Figure 4.11 Reconstructions of Sparse SENSE for the sagittal dataset with decreasing reduction factors are compared. SOS reconstruction is shown in (a). In (b), 24/92 represents that 92 phase-encoding lines were acquired with the variable density-sampling pattern, which has 24 fully sampled ACS lines and the rest randomly sampled. The reduction factor is R = 256/92 = 2.78. In (c–e), it is seen that Sparse SENSE suffers from aliasing artifacts despite increased number of ACS lines and phase-encoding lines. Sparse SENSE in (f) achieves a reconstruction quality similar to that of Sparse BLIP when the number of ACS lines and phase-encoding lines increase to 40/108, corresponding to R = 2.37.

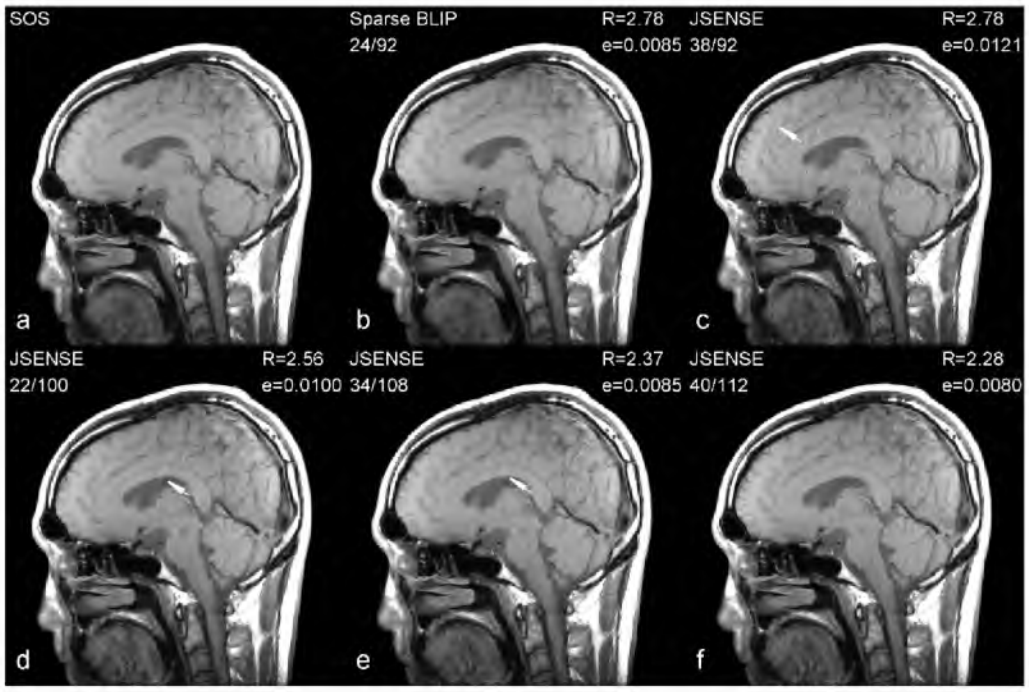

Figure 4.12 Comparison of Sparse BLIP with JSENSE to show the improvement of acceleration rate of Sparse BLIP over JSENSE. Reconstructions of JSENSE for the sagittal dataset with decreasing reduction factors. SOS is shown in (a), Sparse BLIP with reduction factor of 2.78 is shown in (b), and JSENSE with reduction factor of 2.78, 2.56, 2.37, and 2.28 are shown in (c) – (f). JSENSE in (f) achieves a reconstruction quality close to (but still with aliasing) that of Sparse BLIP when the number of phase-encoding lines increases to 112, corresponding to R = 2.28. So the improvement of Sparse BLIP over JSENSE is around 20%.

Table 4.1 nRMSE of different methods over iteration for the four different datasets: phantom, in vivo brain data with coronal, sagittal, and axial views. The nRMSE of Sparse BLIP is lower than those of L_1-SPIRiT and Sparse SENSE after convergence.

Method / Data	L_1-SPIRiT	Sparse BLIP			
		Iteration 1 (Sparse SENSE)	Iteration 2	Iteration 3	Iteration 4
Phantom	0.0501	0.0171	0.0149	0.0144	0.0143
In vivo coronal	0.0235	0.0195	0.0183	0.0175	0.0174
In vivo sagittal	0.0105	0.0096	0.0094	0.0092	0.0092
In vivo axial	0.0403	0.0444	0.0363	0.035	0.0346

Table 4.2 Take RMSE of each step during the iterations as a stop criterion.

Iterations	RMSE of **f**-step	RMSE of **s**-step
1	0.000461	0.000388
2	0.000352	0.000341
3	0.000327	0.000327
4	0.000321	0.000323

CHAPTER 5

A STUDY OF TEMPORAL CONSTRAINED RECONSTRUCTION AND MODEL-BASED RECONSTRUCTION FOR DCE-MRI

5.1 Introduction

Dynamic Contrast Enhanced magnetic resonance imaging (DCE-MRI) has emerged in the past decade as an important imaging tool for both routine clinical practice and cancer detection and treatment. Although MRI speeds have increased dramatically over the last two decades, many DCE-MRI applications require still faster imaging methods to provide the desired spatial and temporal resolutions. A common approach to balance the trade-off between spatial resolution and temporal resolution is to reduce the sampling of k-space data at each time frame. Examples of such methods include UNFOLD (41), keyhole (34) , RIGR (42), HYPR (43), and k-t BLAST/k-t SENSE (44). Most of these methods use constraints or prior information in the image reconstruction to compensate for the information loss from reduced sampling. In particular, temporal constrained reconstruction (TCR) (15,73) is an effective method to produce good reconstruction by imposing the temporal constraint that the images of adjacent time frames are similar, and in which case temporal total variation (TV) is a reasonable regularization term. The TCR approach, however, requires the reconstruction of every pixel in each time frame, and hence involves a huge number of unknown variables in the reconstruction. An alternative approach to incorporate prior information into the reconstruction is in the form of the pharmacokinetic

model (16,19,20). Such model-based reconstruction method reduces the reconstruction task from estimating each pixel intensity over time to estimating only the parameters of the model. Both the TCR approach and the model-based approach have been shown to achieve high quality reconstructions for reduction factors up to 10.

In this work, we conduct an in-depth study of the TCR approach and the model-based approach and develop improved versions of these algorithms to achieve good image reconstructions for highly sparse DCE-MRI data. We find that, at high reduction factors, the choice of the initial image plays a critical role in the convergence of the TCR algorithm and the convergence can be accelerated dramatically with the aid of a well-designed sampling pattern, termed the jigsaw sampling. The reconstruction quality of the model-based approach, on the other hand, greatly depends on the accuracy of the initial phase estimate. Our study reveals that, for the high reduction factors considered, the model-based approach performs inferior to the improved TCR approach, even with the best phase estimates available. For the in vivo breast DCE-MRI data, we show that the improved TCR approach can achieve a highly accelerated reduction factor of 30, while achieving a good balance of temporal and spatial resolution without a significant loss in image quality. The improved spatiotemporal resolution leads to better estimation of the kinetic parameters, which is instrumental in improving the accuracy of lesion characterizations.

5.2 Materials and Methods

5.2.1 Improved TCR Method for High Reduction Factor

In this section, we first review the TCR method and then present the improved TCR algorithm for high reduction factors. The TCR method follows the SENSE (3) framework, in which the imaging equation is written as

$$\mathbf{Ef} = \mathbf{d}, \qquad [5.1]$$

where **d** is the vector formed from all k-space data acquired from all channels, and **f** is the unknown image vector formed from the desired full field of view (FOV) image. The encoding matrix **E** consists of the Fourier encoding, i.e.,

$$\mathbf{E}_{m,n} = e^{-i2\pi \mathbf{k}_m \cdot \mathbf{r}_n}, \qquad [5.2]$$

where $\mathbf{k}_m$ denotes the coordinates of the k-space data. To reconstruct the desired image from acquired data, the least-squares method is usually used to solve Eq. [5.1].

Based on the data consistency in the imaging equation, TCR uses the temporal TV as a sparse constraint and the reconstruction is formulated as a nonlinear optimization problem:

$$\arg\min_{\mathbf{f}_{t,c}} \left\{ \sum_t \left\| \mathbf{d}_{t,c} - \mathbf{W}_t \mathbf{E} \mathbf{f}_{t,c} \right\|_2^2 + \alpha \mathrm{TV}_t(\mathbf{f}_c) \right\}, \qquad [5.3]$$

where $\mathbf{d}_{t,c}$ is the vector consisting of the undersampled k-space data acquired from the t-th time frame and the c-th channel, $\mathbf{f}_{t,c}$ is the corresponding unknown image vector, **E** is the Fourier Encoding matrix, $\mathbf{W}_t$ is the sparse sampling pattern of k-space data from the t-th frame, TV_t is the total variation operator along the temporal domain, and α is the regularization parameter which controls the tradeoff between the data consistency term and the prior information term. The temporal TV operator on a complex image series $\mathbf{f}_c$ of the c-th coil is defined as:

$$\mathrm{TV}_t(\mathbf{f}_c) = \sum_{t=1}^{T} \left| \mathbf{f}_{t+1,c} - \mathbf{f}_{t,c} \right|, \qquad [5.4]$$

where t is the frame index for the image series, and T is the total number of frames. Gradient descent algorithm is used to find the optimum solution of Eq. [5.3].

The TCR algorithm (15) is initialized with a low-resolution image, obtained from taking

the inverse-Fourier Transform of the central, fully sampled k-space data in the center of the acquired k-space data. We refer to this TCR algorithm as the low-resolution initialized TCR (LTCR). While LTCR performs well at low reduction factors of up to 10 (add reference), we find that it suffers from performance degradation at high reduction factors. The reconstructed image of LTCR remains blurry after thousands of iterations and the convergence to the optimal solution of [5.3] is very slow.

To improve the convergence of the TCR method, we design an undersampling pattern at the precontrast stage, and these undersampled frames are combined along the temporal direction to form a better baseline estimation. We refer to this sampling pattern as the jigsaw sampling pattern, and an example of such is shown in Figure 5.1. Since the k-space data at the auto-calibration (ACS) region are fully sampled, we take the average of these precontrast frames to obtain the values for the baseline image in the ACS region. The outer k-space data and the averaged ACS data are combined to generate a full k-space data, which are used to obtain an initial estimation of a baseline image. We make replica of this jigsaw image to all time frames and get a whole series of initial estimation images for TCR reconstruction. We refer to this jigsaw sampling enhanced TCR method as JTCR.

5.2.2 Phase Enhanced Model-based Reconstruction Method

In this section, we first review the existing model-based method, then present our approach of phase enhanced model-base reconstruction. The model-based reconstruction method assumes that contrast agent (CA) exchanges at constant rates between vascular space and extravascular-extracellular space (EES). It constrains the magnitude of the reconstructed time series to be consistent with a pharmacokinetic model (16):

$$\mathrm{f}_c(x,t) = \left(\left| S_0(x,c) \right| + K^{trans}(x,c) C_p\left(t - t_0(x,c)\right) * e^{-k_{ep}(x,c)t} \right) \cdot e^{i\varphi(x,c)}, \qquad [5.5]$$

where $f_c(x,t)$ is the complex signal intensity of a pixel, x is the spatial location, t is the frame index, c is the coil index, $|S_0(x,c)|$ is the magnitude of the complex baseline signal of the c-th coil, $K^{trans}(x,c)$ and $k_{ep}(x,c)$ are transfer rates of the CA from plasma to EES and back, $C_p(t)$ is the concentration of CA in the plasma, which remains zero until time $t_0(x,c)$, $\varphi(x,c)$ is the phase, and * is the convolution operator over time.

In (19), model-based reconstruction estimates the phase information $\varphi(x,c)$ from the low-resolution images reconstructed from the fully sampled low-frequency samples or the aliasing measurements images. Since the accuracy of the phase estimation is not guaranteed, the model-based reconstruction suffers from significant reconstruction error at high reduction factors. In this study, we aim to enhance the performance of model-based method using better phase initializations. It is found that an effective way to improve the phase initialization is to adopt the phase estimates provided by JTCR reconstruction. We refer to the JTCR phase enhanced model-based reconstruction as JTCR-M. Note that the baseline estimation used in JTCR-M is the same as that used for JTCR.

5.2.3 Jigsaw Initialization for Other Image Reconstruction Methods

Our study shows that at high reduction factor, the initialization is very important for convergence and it has great effects on the reconstruction quality. We find that the proposed jigsaw initialization method not only works for the TCR method, but also helps to improve the convergence rate of other image reconstruction methods. For instance, when we apply the proposed approach to the PCA method, we find that the jigsaw sampling initialized PCA method, termed JPCA, also demonstrates improved performance than the

standard low-resolution initialized PCA (LPCA) method, since a good initialization will adopt more prior information of the dataset. More detail of the analysis and comparison of those methods are shown in the Results and Discussion sections.

5.2.4 Data Acquisition and Simulation

Breast DCE-MRI datasets were acquired on a Siemens 3 Tesla scanner equipped with a 7-channel dedicated breast coil. Three datasets from three study participants with clinically confirmed breast cancer were obtained under an Institutional Review Board-approved protocol. The root sum-of-squares (SOS) reconstruction from fully sampled data was used as the gold standard for visual comparison. All three k-space datasets were acquired in full and then manually undersampled retrospectively to simulate accelerated scans.

The imaging used a 3-D spoiled gradient echo pulse sequence with the following imaging parameters: TR = 2.35-3.16 ms, TE = 0.99-1.24 ms, flip angle = 10–15°. Omniscan of dose 0.1 ml/kg was injected at 4 ml/s followed by 20 ml saline flush injected at 2 ml/s. Temporal resolution per frame was 12–15 s with data acquired with 6/8 reduced Fourier space in the phase and slice directions and elliptical acquisition in the kx-ky plane. The acquisition matrices for the data kx × ky × kz × T were 256 × 83 × 64 × 45, 256 × 83 × 64 × 42 and 512 × 83 × 51 × 59, respectively. The acquisitions were bilateral, with the read direction left to right. The fast inverse Fourier transform (IFT) was performed in the read (kx) direction, and the ky-kz datasets were extracted from each slice in the x dimension.

Jigsaw sampling patterns are divided into the precontrast stage and the postcontrast stage. In the precontrast stage, the k-space center ACS region has a size of 8 by 8, and the outer reduction factor is 8 and 10, respectively, depending on the total number of frames.

The sampling masks are designed so that the summation of the precontrast sampling masks cover the outer k-space. In the postcontrast stage, k-space data are undersampled with a variable-density random undersampling with the central k-space sampled with Nyquist rate as in Sparse MRI (6). Specifically, the samples are taken randomly with a sampling density that is scaled according to a power of distance from the k-space center. Undersampled k-space data were simulated by randomly picking a portion of the acquired phase encodes in the ky and kz directions. We have tested high reduction factor R=30 for the postcontrast frames.

5.2.5 Implementation Issues

All the reconstructed images of the same dataset were normalized and shown individually on the same scale for visual evaluations of image quality. Quantitative comparison was provided in terms of the normalized root mean squared error (nRMSE) with the SOS as the reference, which is defined as:

$$\text{nRMSE} = \frac{1}{\max\left(f_{\text{SOS}}\right) - \min\left(f_{\text{SOS}}\right)} \sqrt{\frac{\sum_{m=1}^{M}\sum_{n=1}^{N}\sum_{t=1}^{T}\left|\hat{f}\left(m,n,t\right) - f_{\text{SOS}}\left(m,n,t\right)\right|^2}{MNT}}, \qquad [5.5]$$

where $\hat{f}$ is the reconstructed image and f_{SOS} is the SOS image.

The mean intensity (MI) curves obtained from the region of interest (ROI) can be taken as another criterion for the reconstruction quality. To obtain the MI curves, the image series are normalized by dividing the mean value of all frames.

5.3 Results

Figure 5.2 and Figure 5.3 show the reconstructed images and the MI curves from a subject with two lesion regions. The first 8 frames are undersampled with R=8, and the

other frames are undersampled with R = 30. Reconstruction results from JTCR, JPCA, and JTCR-M are compared with the fully sampled SOS image for the last frame. Both JTCR and JPCA achieve smaller estimation error than that of the JTCR-M method. JTCR has a smaller estimation error that that of JPCA even though the reconstruction images are similar. In comparison, JTCR-M gives a noisy reconstruction. In the 1st region of interest (ROI 1), indicated by the left red square, the MI curves of all three methods are close to that of the fully sampled SOS. In the 2nd region of interest (ROI 2), indicated by the right red square, the MI curves of JTCR are still close to the fully sampled SOS, whereas the curves of JPCA and JTCR-M deviate away from that of the SOS towards later frames.

In Figure 5.4 and Figure 5.5, we present results for a second dataset. The jigsaw sampling pattern is the same as that of the first dataset. For this dataset, we also observe that JTCR still gives the smallest reconstruction error among all three methods. For both ROI1 and ROI2, the MI curve of JTCR is the closest to that of the SOS.

Figure 5.6 and Figure 5.7 present the reconstructed images and the MI curves from a third subject with one lesion region. The first 10 frames are undersampled with R= 10 and the other frames are undersampled with R = 30. Both JTCR and JPCA methods produce good reconstructions while JTCR-M gives noisy reconstruction. In the ROI, the MI curves of both JTCR and JPCA are closer to that of the SOS curve than the JTCR-M.

5.4 Discussion and Conclusion

5.4.1 Different Initialization

In this study, we observe that the images of the precontrast stage are similar and a large part of the tissues shown in the postcontrast frames are close to that in the precontrast frames except for the tumor regions. LTCR and LPCA methods adopt the low-resolution

initialization without using such prior information, and thus fail to give quality reconstruction at high reduction factors. Based on this prior information, we design the jigsaw undersampling pattern for initialization, which improves the reconstruction quality for highly undersampled data. Figure 5.8 shows the comparison of low-resolution initialized reconstructions (LTCR and LPCA) with the jigsaw initialized reconstructions (JTCR and JPCA) using one dataset. We can see both LTCR and LPCA give inferior reconstruction at R=30 while JTCR and JPCA improve the reconstruction quality significantly.

5.4.2 Different Jigsaw Sampling Frames

As shown in the Methods section, the jigsaw sampling pattern is designed such that the samples are taken from the first 8 (JTCRF8) precontrast frames. This allows the JTCR to have a better baseline initialization. We have also examined other sampling patterns, such as combining the last 8 (JTCRL8) frames to cover the whole k-space. In this way, the initialization captures more information from the postcontrast frames. The MI curves of two different jigsaw sampling patterns are shown in Figure 5.9. We see that the baseline signal estimation for ROI 2 of JTCRL8 has a larger bias than that of JTCRF8. Thus, for the datasets that we have, we take more samples from the precontrast frames to give a better baseline signal estimation.

5.4.3 Relationship with Model-based Method

As mentioned earlier, the model-based method constrains the magnitude of the reconstructed curves to be consistent with a pharmacokinetic model and good reconstructions can be achieved at relatively low acceleration factors. However, since the

phase information is unknown a priori and needs to be estimated, inaccurate estimation of the phase may lead to large estimation error in the reconstructed image for the model-based method. Figure 5.10 shows the comparison of reconstruction results of model-based methods using the low-resolution phase estimate and the phase estimate from the JTCR reconstruction. We can see the performance of JTCR-M is much better than that of the model-based method using the low-resolution phase estimate. Since JTCR utilizes temporal total variation constraint and does not need the phase information to perform reconstruction, we conclude that the JTCR is more robust than the model-based method for the datasets considered.

Baseline estimation is another important element for model-based reconstruction. In this work, we use the magnitude of the jigsaw image of the precontrast frames as the baseline signal. To show the accuracy of jigsaw baseline estimation, we compare the curves of the model-based method using jigsaw baseline estimation and those using the fully sampled baseline estimation for one dataset with R = 30. For fair comparison, both methods use phase information from the fully sampled images, i.e., true phase information. In Figure 5.11, we can see that the reconstruction curve using jigsaw baseline estimation is close to that using fully sampled baseline estimation. This demonstrates that jigsaw estimation is a good approximation to the true baseline estimation.

5.4.4 Kinetic Parameter Estimation

In clinical applications, the pharmacokinetic parameters are important for diagnosis. Thus, it is meaningful to examine the accuracy of the parameters estimated from the reconstructed MI curves and compare with that obtained from the fully sampled MI curves. The parameters estimation is based on the pharmacokinetic model (16), and the values are

estimated via a nonlinear least-squares function *lsqcurvefit* defined in Matlab® optimization toolbox. The nRMSE of curve fitting parameters K^{trans} and k_{ep} of JTCR, JPCA, and JTCR-M for different ROIs of three datasets are shown in Figure 5.12. The normalized estimation error is calculated based on comparisons with the SOS parameters. We can see that JTCR parameters are closer to the SOS parameters compared to those of the JPCA and JTCR-M methods. To examine the statistical performance of JTCR, JPCA, and JTCR-M across the tumor region, we show the correlation plot of kinetic parameters (K^{trans}, k_{ep}) generated from JTCR, JPCA, and JTCR-M curves with that of the fully sampled SOS curves. The kinetic parameters are computed from the MI curves of many small regions (7x7) across the ROIs. The correlation plots of K^{trans} and k_{ep} are shown in Figure 5.13 and Figure 5.14, respectively. As shown, parameters obtained from JTCR demonstrate the best correlation with the SOS parameters compared to those of JPCA and JTCR-M.

5.5 Conclusion

In the work we provide a comparative study of the TCR method and the model-based method for highly accelerated DCE-MRI data and show that an improved version of the TCR method can achieve a very good image quality at a high reduction factor of 30 without much loss in temporal and spatial resolution. The model-based method shows inferior performance to that of the improved TCR reconstruction, due to the crudeness of the model and inaccurate phase estimation. Further research is needed to improve the model-based method at high reduction factors. This includes the development of a more accurate kinetic model and better phase estimates.

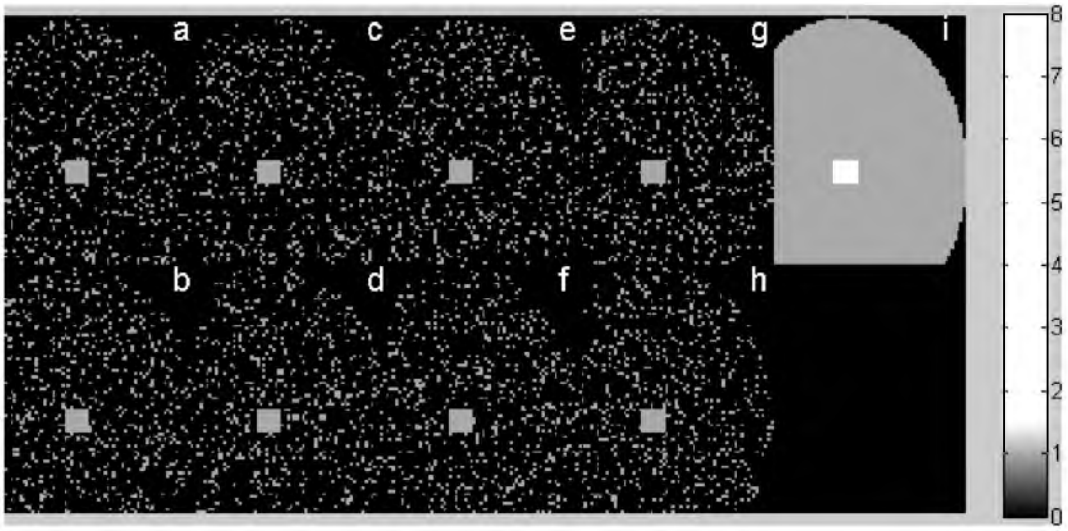

Figure 5.1 The sampling masks for the first 8 precontrast frames are shown in (a)-(h). The central ACS region has a size of 8x8, and the outer reduction factor is 8. The summation of the 8 downsampling masks, shown in (i), covers the entire k-space. Since the central ACS region is covered 8 times, the average of these, together with the outer combined samples, form the k-space samples as shown in (i), which is used to obtain the initial baseline image.

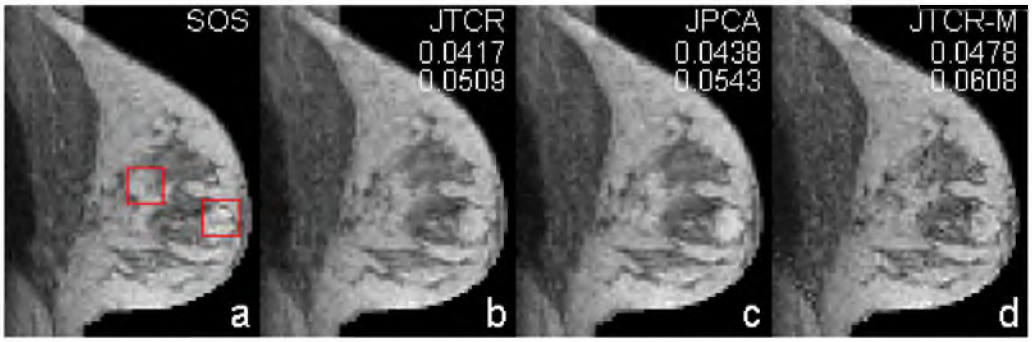

Figure 5.2 The last frame of the reconstructed image of the 1st dataset for R=30 is shown in (a)-(d) for SOS, JTCR, JPCA, and JTCR-M, respectively. The nRMSE averaged over all reconstructed frames (number at the top) and the nRMSE of the last reconstructed frame only (number at the bottom) are shown in each subfigure. Both JTCR and JPCA achieve superior performance than JTCR-M. The reconstruction of JTCR-M is noisy and has the largest nRMSE.

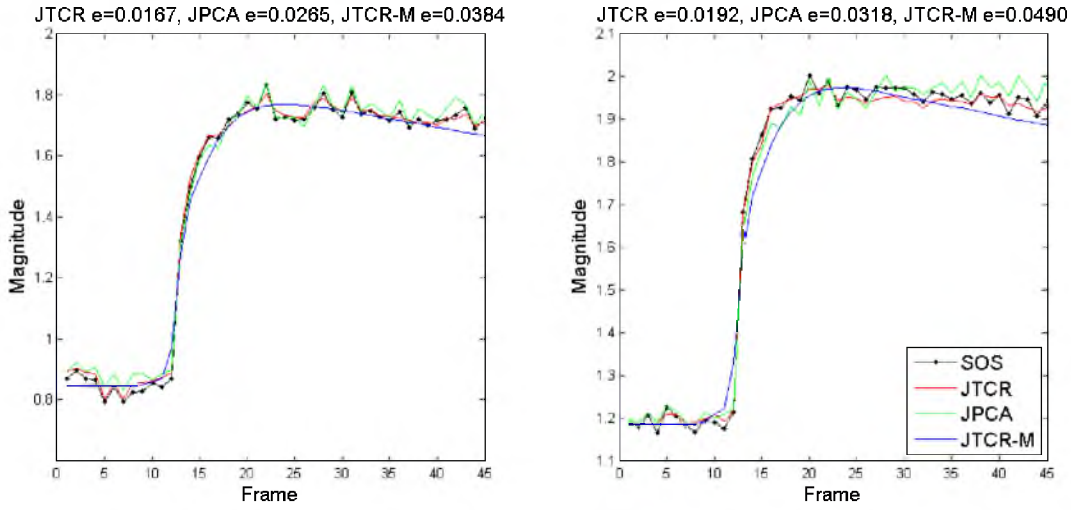

Figure 5.3 MI curves of two ROIs (corresponding to the two subfigures) for JTCR, JPCA, and JTCR-M reconstructions. The error between the MI curve of each reconstruction method and the SOS curve is shown in the figure. In ROI 1 (see the left subfigure), the JTCR curves best match the SOS curve and has the smallest error. In ROI 2 (the right subfigure), the MI curve of JTCR is also the closest to the fully sampled SOS curve, while the curves of JPCA and JTCR-M's show much deviation for the postcontrast frames.

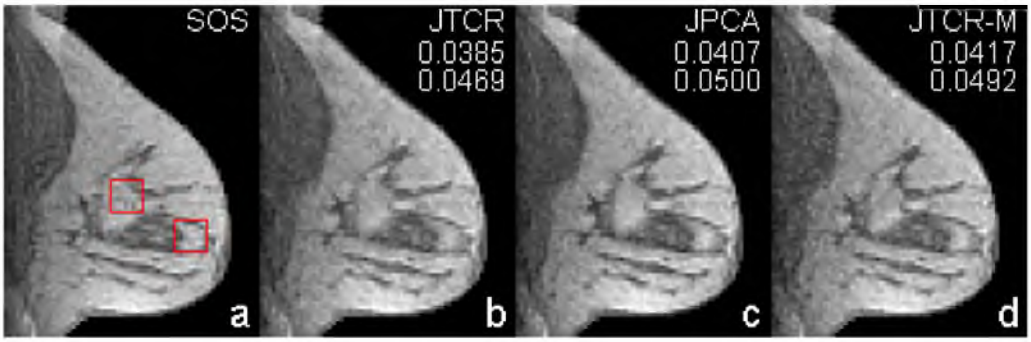

Figure 5.4 The last frame of the reconstructed image of the 2nd dataset for R=30 is shown in (a)-(d) for SOS, JTCR, JPCA, and JTCR-M, respectively. The nRMSE averaged over all reconstructed frames (number at the top) and the nRMSE of the last reconstructed frame only (number at the bottom) are shown in each subfigure. Both JTCR and JPCA achieve superior performance than JTCR-M. The reconstruction of JTCR-M is noisy and has the largest nRMSE.

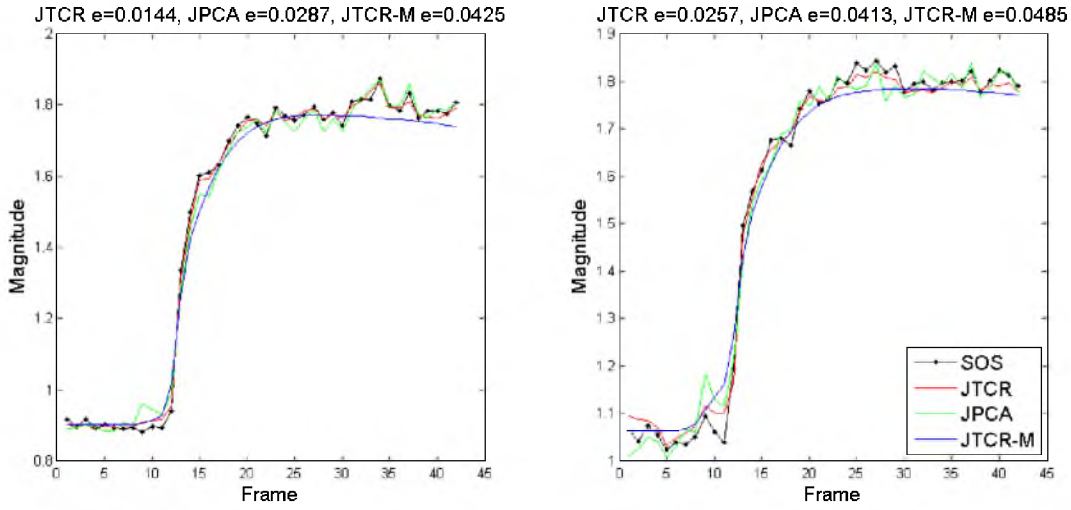

Figure 5.5 MI curves of two ROIs, corresponding to the two subfigures, for JTCR, JPCA, and JTCR-M reconstructions with reduction factor R = 30. The curves of all three methods are close to the fully sampled SOS curve in both ROIs. The MI curves of JTCR have the smallest error compared to JPCA and JTCR-M.

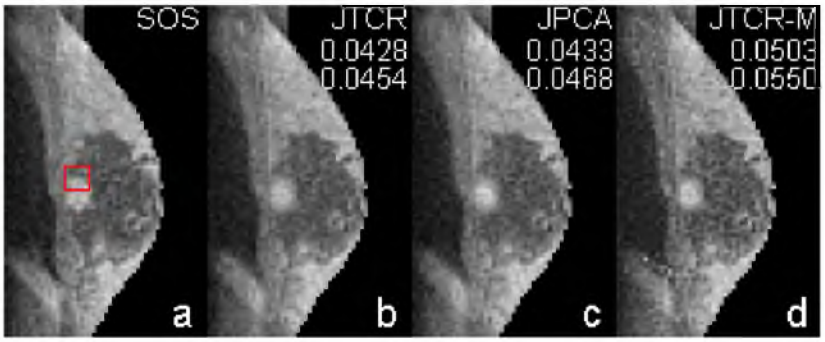

Figure 5.6 The last frame of the reconstructed image of the 3rd dataset for R=30 is shown in (a)-(d) for SOS, JTCR, JPCA, and JTCR-M, respectively. The nRMSE averaged over all reconstructed frames (number at the top) and the nRMSE of the last reconstructed frame only (number at the bottom) are shown in each subfigure. Both JTCR and JPCA achieve superior performance than JTCR-M. The reconstruction of JTCR-M is noisy and has the largest nRMSE.

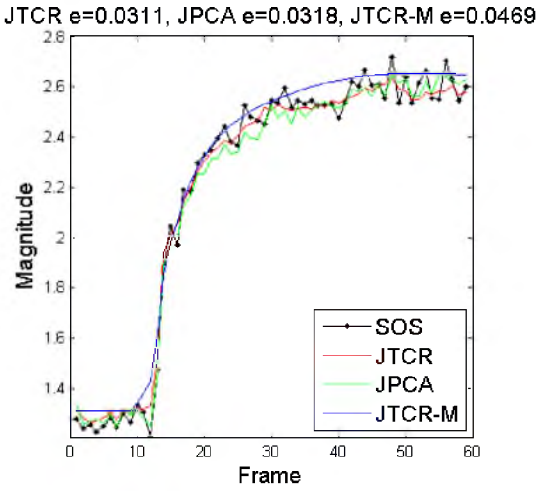

Figure 5.7 MI curves in ROI for JTCR, JPCA, and JTCR-M reconstructions with reduction factor R = 30. The curves of all three methods are close to the fully sampled SOS curve in both ROIs. The MI curve of JTCR has the smallest error compared with JPCA and JTCR-M.

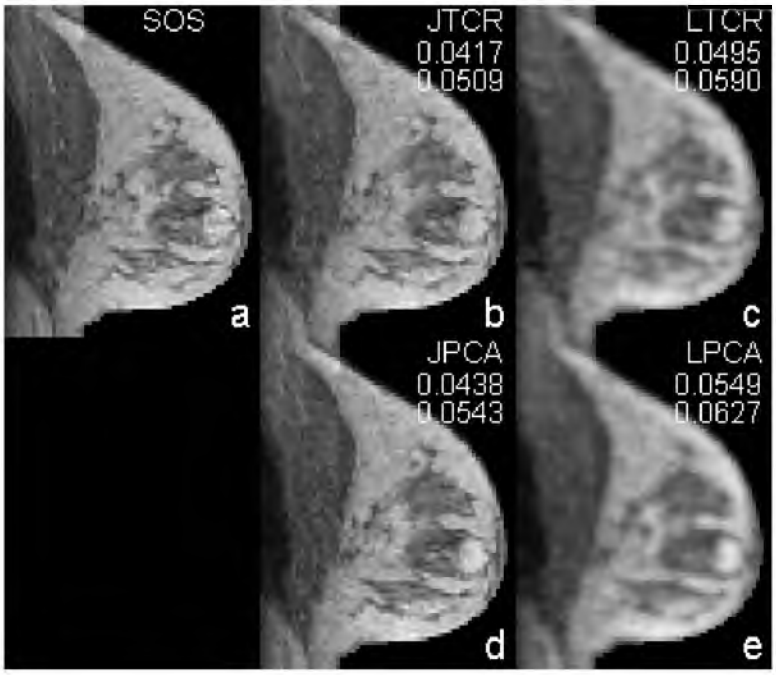

Figure 5.8 Comparisons of low-resolution initialization and jigsaw initialization for TCR and PCA methods. Reconstructed images for SOS, jigsaw initialized TCR, low-resolution initialized TCR, jigsaw initialized PCA, and low-resolution initialized PCA are shown in (a), (b), (c), (d), and (e), respectively. Jigsaw initialized TCR and PCA provide good reconstruction qualities, while low-resolution initialized TCR and PCA give poor reconstruction qualities.

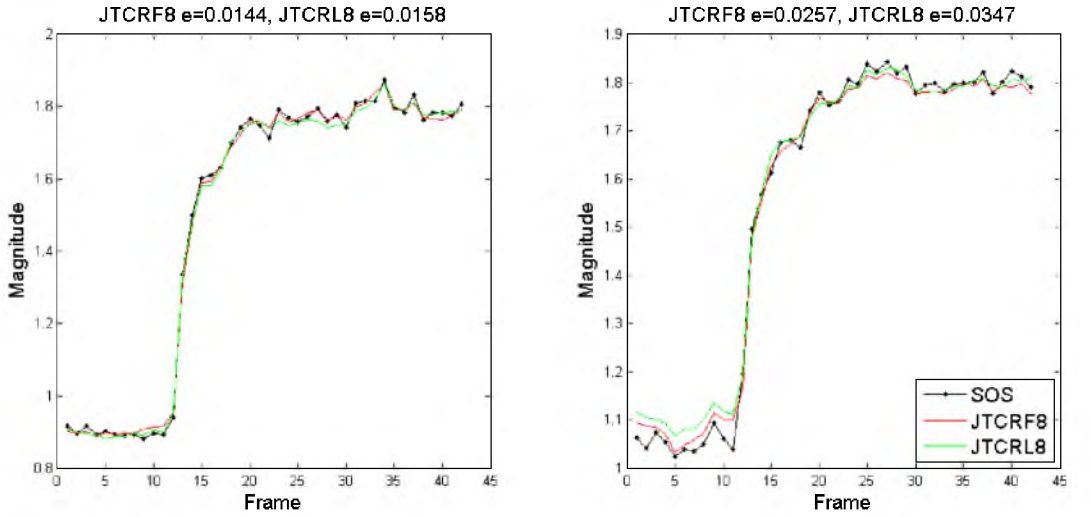

Figure 5.9 Comparisons of JTCR using the first 8 frames and the last 8 frames, respectively, for jigsaw initialization. JTCR using the first 8 frames performs slightly better than that using the last 8 frames.

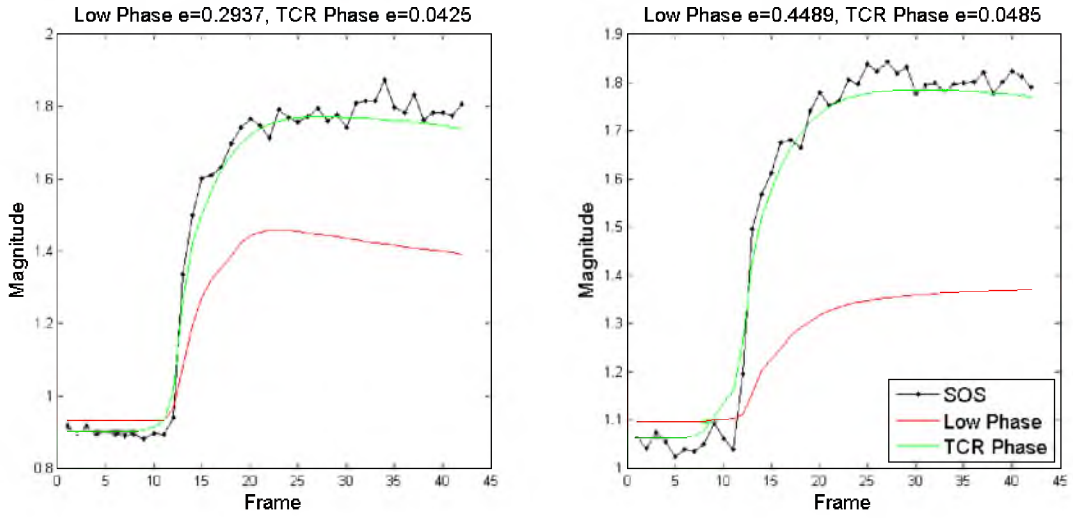

Figure 5.10 The time curves of model-based method using phase estimates from the low-resolution image and from the JTCR reconstruction for reduction factor R = 30.

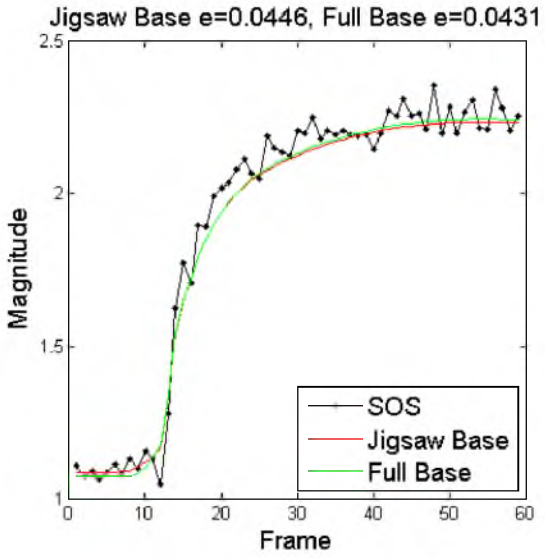

Figure 5.11 The MI curves of model-based method using jigsaw baseline estimation and fully sampled baseline estimation for the 3rd dataset with reduction factor R = 30. The reconstruction curve using jigsaw baseline estimation is close to that using fully sampled baseline estimation.

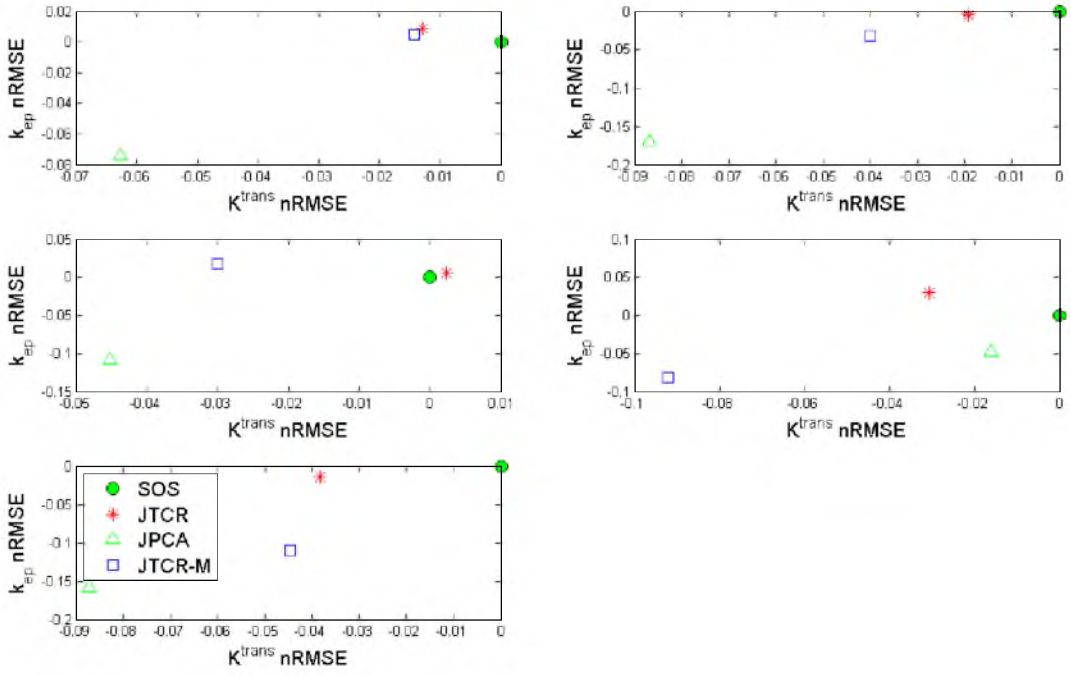

Figure 5.12 The nRMSE of model-based curve fitting parameters K^{trans} and k_{ep} compared with fully sampled SOS curve fitting parameters for the mean signal intensity curves of JTCR, JPCA, and JTCR-M methods. For both parameters, the JTCR estimates are closer to the SOS estimates compared to JPCA and JTCR-M.

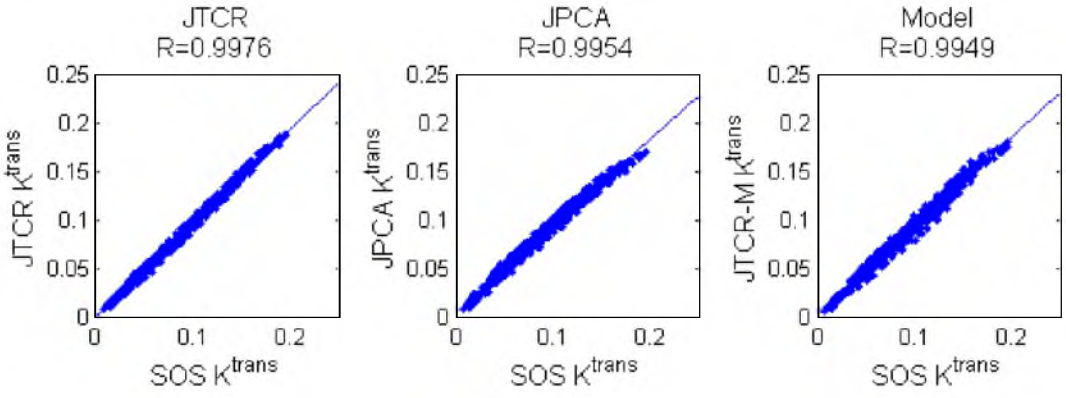

Figure 5.13 The correlation plots of kinetic parameter K^{trans} generated from reconstructed images of SOS, JTCR, JPCA, and JTCR-M. The kinetic parameters are obtained from the mean intensity (MI) curve of a small region (7x7) moving across the ROIs of the three datasets. The value R is the correlation coefficient between the kinetic parameter estimates from the SOS method and other methods.

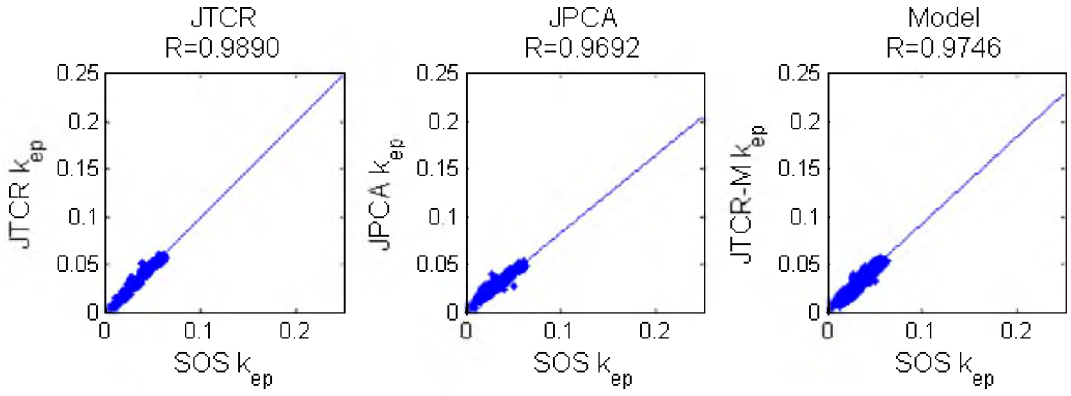

Figure 5.14 The correlation plots of kinetic parameter k_{ep} generated from reconstructed images of SOS, JTCR, JPCA, and JTCR-M. The kinetic parameters are obtained from the mean intensity (MI) curve of a small region (7x7) moving across the ROIs of the three datasets. The value R is the correlation coefficient between the kinetic parameter estimates from the SOS method and other methods.

CHAPTER 6

CONCLUSIONS AND FUTURE WORK

In this thesis, we developed novel signal processing techniques within the blind estimation and compressed sensing framework to improve MRI image reconstruction for parallel MRI and DCE-MRI. This work is innovative in several aspects: a) it addresses the problem of ill-conditioning and inaccurate sensitivities in parallel imaging simultaneously with a novel joint optimization approach. The reconstruction algorithms result in a more uniform image and achieve better spatial resolution with a smaller number of acquired k-space samples. b) It provides a comparative study of the TCR method and the model-based method for DEC-MRI and shows that high quality reconstruction images and accurate kinetic parameters can be obtained at the high reduction factor of 30 without much loss of spatial or temporal resolution.

An interesting direction for future work is to study the integration of parallel imaging with dynamic imaging. It is promising to investigate the application of Sparse BLIP to DCE-MRI applications to explore the benefit of data correlation across space (parallel imaging) and the data dependence over time. Extension of Sparse BLIP to non-Cartesian sampling will make it applicable to a wider range of applications and signal types. The extension of the proposed work to 3-D imaging is also worth pursuing because it has the potential to greatly accelerate the current slow imaging speed of 3-D imaging and enhance the image quality. Another direction of handling 3-D and dynamic imaging is the dictionary

learning method. Through the dictionary learning, more information of the datasets could be utilized to improve the quality of reconstruction. Finally, the development of more accurate kinetic models for DEC-MRI will be important for further improvement of spatial and temporal resolution for very sparse DEC-MRI data.

REFERENCES

1. Liang Z-P, Lauterbur PC. Principles of magnetic resonance imaging: a signal processing perspective. Institute of Electrical and Electronics Engineers Press; 2000.

2. Sodickson DK, Manning WJ. Simultaneous acquisition of spatial harmonics (SMASH): fast imaging with radiofrequency coil arrays. Magnetic Resonance in Medicine 1997;38(4):591-603.

3. Pruessmann KP, Weiger M, Scheidegger MB, Boesiger P. SENSE: sensitivity encoding for fast MRI. Magnetic Resonance in Medicine 1999;42(5):952-962.

4. Griswold MA, Jakob PM, Heidemann RM, Nittka M, Jellus V, Wang J, Kiefer B, Haase A. Generalized autocalibrating partially parallel acquisitions (GRAPPA). Magnetic Resonance in Medicine 2002;47(6):1202-1210.

5. Donoho DL. Compressed sensing. Information Theory, IEEE Transactions on 2006;52(4):1289-1306.

6. Lustig M, Donoho D, Pauly JM. Sparse MRI: The application of compressed sensing for rapid MR imaging. Magnetic Resonance in Medicine 2007;58(6):1182-1195.

7. Liu B, Sebert F, Zou Y, Ying L. SparseSENSE: randomly-sampled parallel imaging using compressed sensing. 2008. Citeseer.

8. Lustig M, Pauly JM. SPIRiT: Iterative self-consistent parallel imaging reconstruction from arbitrary k-space. Magnetic Resonance in Medicine 2010;64(2):457-471.

9. Roemer PB, Edelstein WA, Hayes CE, Souza SP, Mueller OM. The NMR phased array. Magnetic Resonance in Medicine 1990;16(2):192-225.

10. Gurelli MI, Nikias CL. EVAM: An eigenvector-based algorithm for multichannel blind deconvolution of input colored signals. Signal Processing, IEEE Transactions on 1995;43(1):134-149.

11. Hua Y. Fast maximum likelihood for blind identification of multiple FIR channels. Signal Processing, IEEE Transactions on 1996;44(3):661-672.

12. Harikumar G, Bresler Y. Perfect blind restoration of images blurred by multiple filters: Theory and efficient algorithms. Image Processing, IEEE Transactions on 1999;8(2):202-219.

13. Ying L, Liang Z-P. Parallel MRI using phased array coils: multichannel sampling theory meets spin physics. Signal Processing Magazine, IEEE 2010;27(4):90-98.

14. Ying L, Sheng J. Joint image reconstruction and sensitivity estimation in SENSE (JSENSE). Magnetic Resonance in Medicine 2007;57(6):1196-1202.

15. Adluru G, Awate SP, Tasdizen T, Whitaker RT, DiBella EV. Temporally constrained reconstruction of dynamic cardiac perfusion MRI. Magnetic Resonance in Medicine 2007;57(6):1027-1036.

16. Tofts PS, Brix G, Buckley DL, Evelhoch JL, Henderson E, Knopp MV, Larsson HB, Lee T-Y, Mayr NA, Parker GJ. Estimating kinetic parameters from dynamic contrast-enhanced T_1-weighted MRI of a diffusable tracer: standardized quantities and symbols. Journal of Magnetic Resonance Imaging 1999;10(3):223-232.

17. Morrison RL, Jacob M, Do MN. Multichannel estimation of coil sensitivities in parallel MRI. 2007. IEEE International Symposium on Biomedical Imaging. p 117-120.

18. Knoll F, Clason C, Bredies K, Uecker M, Stollberger R. Parallel imaging with nonlinear reconstruction using variational penalties. Magnetic Resonance in Medicine 2012;67(1):34-41.

19. Felsted BK, Whitaker RT, Schabel MC, DiBella EVR. A Dynamic-Phase Extension for Model-Based Reconstruction of Breast Tumor Dynamic Contrast Enhanced MRI. 2010. p 2934.

20. Felsted BK, Whitaker RT, Schabel M, DiBella EV. Model-based reconstruction for undersampled dynamic contrast-enhanced MRI. 2009. International Society for Optics and Photonics. p 72622S-72622S-72610.

21. Haacke EM, Brown R, Thompson M, Venkatesan R. Magnetic resonance imaging: physical principles and sequence design. New York: John Wiley & Sons; 1999.

22. McRobbie DW, Moore EA, Graves MJ, Prince MR. MRI from picture to proton: Cambridge University Press; 2006.

23. Hashemi RH, Bradley WG, Lisanti CJ. MRI: the basics: Lippincott Williams & Wilkins; 2012.

24. Griswold MA, Jakob PM, Nittka M, Goldfarb JW, Haase A. Partially parallel imaging with localized sensitivities (PILS). Magnetic Resonance in Medicine

2000;44(4):602-609.

25. Jakob PM, Grisowld MA, Edelman RR, Sodickson DK. AUTO-SMASH: a self-calibrating technique for SMASH imaging. Magnetic Resonance Materials in Physics, Biology and Medicine 1998;7(1):42-54.

26. Heidemann RM, Griswold MA, Haase A, Jakob PM. VD-AUTO-SMASH imaging. Magnetic Resonance in Medicine 2001;45(6):1066-1074.

27. Brau A, Beatty PJ, Skare S, Bammer R. Comparison of reconstruction accuracy and efficiency among autocalibrating data-driven parallel imaging methods. Magnetic Resonance in Medicine 2008;59(2):382-395.

28. Wang Z, Wang J, Detre JA. Improved data reconstruction method for GRAPPA. Magnetic resonance in medicine 2005;54(3):738-742.

29. Huo D, Wilson DL. Robust GRAPPA reconstruction and its evaluation with the perceptual difference model. Journal of Magnetic Resonance Imaging 2008;27(6):1412-1420.

30. Liang Z-P, Ying L, Xu D, Yuan L. Parallel imaging: some signal processing issues and solutions. 2004. IEEE International Symposium on Biomedical Imaging. p 1204-1207.

31. Candès EJ, Romberg J, Tao T. Robust uncertainty principles: exact signal reconstruction from highly incomplete frequency information. Information Theory, IEEE Transactions on 2006;52(2):489-509.

32. Candes EJ, Tao T. Decoding by linear programming. Information Theory, IEEE Transactions on 2005;51(12):4203-4215.

33. Candes EJ, Romberg JK, Tao T. Stable signal recovery from incomplete and inaccurate measurements. Communications on Pure and Applied Mathematics 2006;59(8):1207-1223.

34. Van Vaals JJ, Brummer ME, Thomas Dixon W, Tuithof HH, Engels H, Nelson RC, Gerety BM, Chezmar JL, Den Boer JA. "Keyhole" method for accelerating imaging of contrast agent uptake. Journal of Magnetic Resonance Imaging 1993;3(4):671-675.

35. d'Arcy J, Collins D, Rowland I, Padhani A, Leach M. Applications of sliding window reconstruction with cartesian sampling for dynamic contrast enhanced MRI. NMR in Biomedicine 2002;15(2):174-183.

36. Feng L, Otazo R, Jung H, Jensen JH, Ye JC, Sodickson DK, Kim D. Accelerated cardiac T2 mapping using breath-hold multiecho fast spin-echo pulse sequence

with k-t FOCUSS. Magnetic Resonance in Medicine 2011;65(6):1661-1669.

37. Gamper U, Boesiger P, Kozerke S. Compressed sensing in dynamic MRI. Magnetic Resonance in Medicine 2008;59(2):365-373.

38. Jung H, Sung K, Nayak KS, Kim EY, Ye JC. k-t FOCUSS: A general compressed sensing framework for high resolution dynamic MRI. Magnetic Resonance in Medicine 2009;61(1):103-116.

39. Pedersen H, Kozerke S, Ringgaard S, Nehrke K, Kim WY. k-t PCA: Temporally constrained k-t BLAST reconstruction using principal component analysis. Magnetic Resonance in Medicine 2009;62(3):706-716.

40. Barrett T, Brechbiel M, Bernardo M, Choyke PL. MRI of tumor angiogenesis. Journal of Magnetic Resonance Imaging 2007;26(2):235-249.

41. Madore B, Glover GH, Pelc NJ. Unaliasing by Fourier-encoding the overlaps using the temporal dimension (UNFOLD), applied to cardiac imaging and fMRI. Magnetic Resonance in Medicine 1999;42(5):813-828.

42. Webb AG, Liang ZP, Magin RL, Lauterbur PC. Applications of reduced - encoding MR imaging with generalized-series reconstruction (RIGR). Journal of Magnetic Resonance Imaging 1993;3(6):925-928.

43. Mistretta C, Wieben O, Velikina J, Block W, Perry J, Wu Y, Johnson K. Highly constrained backprojection for time-resolved MRI. Magnetic Resonance in Medicine 2006;55(1):30-40.

44. Tsao J, Boesiger P, Pruessmann KP. k-t BLAST and k-t SENSE: Dynamic MRI with high frame rate exploiting spatiotemporal correlations. Magnetic Resonance in Medicine 2003;50(5):1031-1042.

45. Kellman P, McVeigh ER. Ghost artifact cancellation using phased array processing. Magnetic Resonance in Medicine 2001;46(2):335-343.

46. Axel L, Costantini J, Listerud J. Intensity correction in surface-coil MR imaging. American Journal of Roentgenology 1987;148(2):418-420.

47. Murakami JW, Hayes CE, Weinberger E. Intensity correction of phased - array surface coil images. Magnetic Resonance in Medicine 1996;35(4):585-590.

48. Walsh DO, Gmitro AF, Marcellin MW. Adaptive reconstruction of phased array MR imagery. Magnetic Resonance in Medicine 2000;43(5):682-690.

49. Bydder M, Larkman DJ, Hajnal JV. Combination of signals from array coils using image-based estimation of coil sensitivity profiles. Magnetic Resonance in

Medicine 2002;47(3):539-548.

50. Debbins JP, Felmlee JP, Riederer SJ. Phase alignment of multiple surface coil data for reduced bandwidth and reconstruction requirements. Magnetic resonance in medicine 1997;38(6):1003-1011.

51. Hadjidemetriou S, Studholme C, Mueller S, Weiner M, Schuff N. Restoration of MRI data for intensity non-uniformities using local high order intensity statistics. Medical Image Analysis 2009;13(1):36-48.

52. Çukur T, Lustig M, Nishimura DG. Multiple-profile homogeneous image combination: application to phase-cycled SSFP and multicoil imaging. Magnetic Resonance in Medicine 2008;60(3):732-738.

53. Sroubek F, Cristóbal G, Flusser J. A unified approach to superresolution and multichannel blind deconvolution. Image Processing, IEEE Transactions on 2007;16(9):2322-2332.

54. Ying L, Liu B, Steckner MC, Wu G, Wu M, Li SJ. A statistical approach to SENSE regularization with arbitrary k-space trajectories. Magnetic Resonance in Medicine 2008;60(2):414-421.

55. She H, Chen R-R, Liang D, Chang Y, Ying L. Image reconstruction from phased-array MRI data based on multichannel blind deconvolution. 2010. IEEE International Symposium on Biomedical Imaging. p 760-763.

56. Chan TF, Wong C-K. Convergence of the alternating minimization algorithm for blind deconvolution. Linear Algebra and its Applications 2000;316(1):259-285.

57. Papoulis A. Generalized sampling expansion. IEEE Transactions on Circuits and Systems 1977;24(11):652-654.

58. Kyriakos WE, Panych LP, Kacher DF, Westin CF, Bao SM, Mulkern RV, Jolesz FA. Sensitivity profiles from an array of coils for encoding and reconstruction in parallel (SPACE RIP). Magnetic Resonance in Medicine 2000;44(2):301-308.

59. Uecker M, Hohage T, Block KT, Frahm J. Image reconstruction by regularized nonlinear inversion—joint estimation of coil sensitivities and image content. Magnetic Resonance in Medicine 2008;60(3):674-682.

60. Huang F, Chen Y, Yin W, Lin W, Ye X, Guo W, Reykowski A. A rapid and robust numerical algorithm for sensitivity encoding with sparsity constraints: Self-feeding sparse SENSE. Magnetic Resonance in Medicine 2010;64(4): 1078-1088.

61. Liang D, Liu B, Wang J, Ying L. Accelerating SENSE using compressed sensing. Magnetic Resonance in Medicine 2009;62(6):1574-1584.

62. Wu B, Millane R, Watts R, Bones P. Applying compressed sensing in parallel MRI. 2008. Proceedings of the 16th Annual Meeting of ISMRM. p 1480.

63. Otazo R, Kim D, Axel L, Sodickson DK. Combination of compressed sensing and parallel imaging for highly accelerated first-pass cardiac perfusion MRI. Magnetic Resonance in Medicine 2010;64(3):767-776.

64. King K. Combining compressed sensing and parallel imaging. 2008. Proceedings of the 16th annual meeting of ISMRM. p 1488.

65. Ji JX, Zhao C, Lang T. Compressed sensing parallel magnetic resonance imaging. 2008. 30th Annual International Conference of the IEEE Engineering in Medicine and Biology Society. p 1671-1674.

66. Wu B, Millane RP, Watts R, Bones PJ. Prior estimate - based compressed sensing in parallel MRI. Magnetic Resonance in Medicine 2011;65(1):83-95.

67. Keeling SL, Clason C, Hintermüller M, Knoll F, Laurain A, Von Winckel G. An image space approach to Cartesian based parallel MR imaging with total variation regularization. Medical Image Analysis 2012;16(1):189-200.

68. Fernandez-Granda C, Senegas J. L1-norm regularization of coil sensitivities in non-linear parallel imaging reconstruction. 2009. Proceedings of the 17th Annual Meeting of ISMRM. p 380.

69. Brooks DH, Ahmad GF, MacLeod RS, Maratos GM. Inverse electrocardiography by simultaneous imposition of multiple constraints. Biomedical Engineering, IEEE Transactions on 1999;46(1):3-18.

70. Hansen PC. Rank-deficient and discrete ill-posed problems: numerical aspects of linear inversion: Siam; 1998.

71. Velikina JV, Alexander AL, Samsonov A. Accelerating MR parameter mapping using sparsity-promoting regularization in parametric dimension. Magnetic Resonance in Medicine 2013;70(5):1263-1273.

72. Liang D, Wang H, Chang Y, Ying L. Sensitivity encoding reconstruction with nonlocal total variation regularization. Magnetic Resonance in Medicine 2011;65(5):1384-1392.

73. Adluru G, McGann C, Speier P, Kholmovski EG, Shaaban A, DiBella EV. Acquisition and reconstruction of undersampled radial data for myocardial perfusion magnetic resonance imaging. Journal of Magnetic Resonance Imaging 2009;29(2):466-473.